Synergy in Additive Manufacturing and Machining of Complex Design Topologies

by

Yanli Zhu

A thesis

presented to the University of Waterloo

in fulfillment for the degree of

Master of Applied Science

in

Mechanical and Mechatronics Engineering

Waterloo, Ontario, Canada, 2019

AUTHOR'S DECLARATION

I hereby declare that I am the sole author of this thesis. This is a true copy of the thesis, including any required final revisions, as accepted by my examiners.

I understand that my thesis may be made electronically available to the public.

Abstract

Additive manufacturing (AM) enables freedom of design, part complexity and customization with minimal added cost, light weighting, design for function, and part consolidation. It is gaining increasing interests in the fields of biomedical, aerospace, automotive, tooling, and heat exchange systems where small batch productions of customized parts with high value are usually in demand. AM, in general, is considered to have great potential in complementing conventional manufacturing methods. Functional parts with high strength to weight ratio generated using structural topology optimization can be eventually realized by AM. Limitations of AM parts related to surface finish and dimensional accuracy are likely to be overcome by post-machining of critical features and surfaces in order to achieve specific tolerance and surface quality. To minimize trial and error efforts, AM and post-machining simulations are essential for effective planning of the synergized processes. The goal of this study is to propose a process workflow which can be used as a guideline for successful production of complex parts manufactured via AM, particularly laser powder bed fusion (LPBF), and post-processed via CNC (computer numerical control) machining. The workflow is deployed and iterated through a case study of manufacturing a surgical navigation tracker, where the holistic manufacturing process involves digital design utilizing structural topology optimization, AM simulation, machining planning, fabrication, and validation.

Acknowledgements

I would like to express my gratitude to my supervisor, Professor Mihaela Vlasea, for giving me the opportunity to work on this project and for her inspiration and guidance throughout my research.

I would like to thank Professor Kaan Erkorkmaz and Dr. Ahmet Okyay for their insights in the machining aspect and providing me with necessary trainings and advice.

I would like to thank Intellijoint Surgical and Renishaw Canada for providing their inputs, technical knowhow as well as resources such as machine time, material, and instruments into this project.

I would also like to thank the technical stuff Jerry Ratthapakdee for the help with preparing build files for additive manufacturing and Robert Wagner for his assistance with experimental setups for machining cutting tests.

Finally, I would like to thank all my colleagues from the Multi-Scale Additive Manufacturing Lab, my friends and family for their supports during my degree.

Dedication

To my parents

Table of Contents

List of Figures

List of Tables

Nomenclature

Symbol	Definition	Units
ϕ_c	Shear angle	°
r_c	Chip compression ratio	
h	Undeformed chip thickness	mm
h_c	Deformed chip thickness	mm
α_r	Rake angle	°
β_a	Friction angle	°
τ_s	Shear stress	MPa
A_s	Shear plane area	mm^2
b	Width of cut	mm
K_c	Cutting coefficients	N/mm^2
K_e	Edge coefficients	N/mm
ϕ_n	Normal shear angle	°
β_n	Normal friction angle	°
α_n	Normal rake angle	°
i	Chip flow angle	°
η	Inclination angle	°
n	Spindle speed	rpm
c	Feed per tooth	mm
a	Axial depth of cut	mm
ϕ_{st}	Start immersion angle	°

ϕ_{et}	Exit immersion angle	°
ϕ	Instantaneous immersion angle	°
ω_c	Chatter frequency	Hz
ε	Phase shift between succeeding waves in regenerative chatter vibration	rad
ω_r	Natural frequency	Hz
ζ_r	Damping ratio	
k_r	Stiffness	N/m
m_r	Mass	kg

Chapter 1

Introduction

Additive manufacturing (AM) has received growing attention from industry. This is in part attributed to the fact that geometric complexity can be achieved with ease, whereas conventional manufacturing methods have restrictions in terms of fabrication of geometries. Also, owing to the tool-less nature of the process, AM has advantages in small batch production of high value added customized components. Laser powder bed fusion (LPBF), a type of AM, utilizes a laser beam to successively melt layers of metal powders to form a near-net shape part. The quality of AM parts is sensitive to print parameters and materials of choice. Inherently, poor surface finish, geometric distortion due to thermal induced residual stress, and anisotropic properties are commonly observed in AM parts. As result, in order to produce complex parts with high precision features such as mating surfaces and threaded holes, it is desired to post-machine critical features on an AM part to achieve the required dimensional tolerance. Simulation of the AM process to predict geometric distortion is essential in order to make geometric compensation and to plan for machining allowance.

AM offers design potentials such as consolidation of assemblies, integration of lattice structures for light weight parts, realization of structural topology optimization for high strength to weight ratio components, and customization of part design. AM has growing applications in automotive, aerospace and biomedical sectors due to the unique design possibilities. There is also an increased need to streamline strategies for design optimization with considerations for AM and post-processing constraints.

In order to holistically utilize the capabilities of AM and SM (subtractive manufacturing), hybrid manufacturing solutions have been proposed in literature and industry, which can be mainly categorized into an integrated process alternating between AM and SM or a separated AM process followed by SM. Manufacturing constraints related to the AM process include overhang and support structures, part size, geometric distortion, powder evacuation from internal holes, etc. Challenges of post-machining of AM products include machine tool accessibility, machining allowance and trajectories planning, datum selection, fixturing methods for complex near-net-shape parts, vibration minimization under cutting forces, variable properties, etc. As a result, thorough process planning for the synergized AM and SM process is essential in order to minimize trial and error attempts and scrap parts.

1.1 Problem statement

For the successful design and fabrication of complex components, it is important to foresee as many of the manufacturing challenges as possible at the design stage. As such, there is a need for a harmonized digital workflow of the additive manufacturing and post-machining processes as a guideline for product design optimization and process planning.

1.2 Motivation and objectives

The motivation behind this thesis is to generate a workflow for synergistically combining AM and post-machining for highly complex geometries achievable via LPBF. The following objectives are of interest in this study: CAD design utilizing topology optimization, AM process simulation, machining planning, fabrication, and part validation. The goal is to be able to deploy and iterate on the workflow through a case study of manufacturing a surgical tool using AM

followed by post-machining in order to produce a part which fulfils all functional and dimensional specifications.

1.3 Thesis outline

In Chapter 2, a literature review is presented on the LPBF technology as well as design potentials, especially structural topology optimization and challenges related to the process. A brief overview is provided on the applications of AM in biomedical implants and surgical tools. In the same chapter, a component of a surgical navigation system (tracker) is introduced with the potential to redesign the part for AM and post-machining. Existing AM and SM synergy strategies in the literature are explored. Major challenges for post-machining AM parts are identified through the review of case studies. Several distortion simulation models are reviewed. On the machining side, the focus of this study is to minimize chatter during machining through chatter stability analysis. As a result, the experimental method which is usually used in the identification of cutting force coefficients and a simple zero order analytical solution for predicting chatter stability are explained. Based on the literature review of different aspects of AM and SM processes, a synergized AM and SM process workflow is proposed.

In Chapter 3, general properties of AM parts including powder size distribution, surface roughness, hardness, and porosity are obtained via experiments on AM artifacts. These properties have influence on the performance and machinability of the AM part.

In Chapter 4, design considerations for AM are addressed with the focus on structural topology optimization, AM build setup, geometric distortion simulation, and validation of geometric distortion of printed part via 3D optical scanning. It is important to design a part that is not only optimized functionally but also for manufacturing. A reliable distortion prediction model is

useful in finding optimum AM build parameters for distortion minimization, making geometric compensation and efficient planning for machining allowance.

In Chapter 5, design and manufacturing considerations for machining are presented. Firstly, cutting force coefficients are identified for the specific AM material and cutter, as they are key for cutting force prediction, vibration analysis and surface quality prediction. Next, modal analysis is performed on the cutter in order to determine the vibratory behavior of the cutter. With the cutting force coefficients and vibratory performance of the cutter, chatter stability lobes are generated for the cutting in order to plan for the chatter free depth of cut and spindle speed while ensuring productivity. Chatter stability of the workpiece mounted on the CNC machine by two fixturing methods are also compared.

Chapter 6 describes the actual AM and post-machining fabrication process of the demonstrator (Cobra tracker). Lastly, Chapter 7 provides conclusions of the project and recommendations for future work.

Chapter 2

Background and Literature Review

2.1 Laser powder bed fusion (LPBF) technology overview

2.1.1 Description of LPBF technology

The ASTM F42 Technology Committee defines the additive manufacturing (AM) technology as "a process of joining materials to make objects from 3D models data, usually layer upon layer, as opposed to subtractive manufacturing methodologies" [1]. The AM process is started directly with a 3D CAD file, which is usually in STL format. The STL file is imported into a specific software such as Magics RP® by Materialise, Viscam® by Marcam, and Netfabb® by FIT, where it is pre-processed [2]. During pre-processing, depending on the type of AM process, the part is oriented for building and support structures are generated under overhangs or local minima for the purpose of part anchoring, weight supporting, or heat sinking. Afterwards, the 3D CAD model and the support structures are sliced into layers with specified layer thickness.

Based on factors such as the form of feedstock materials, material deposition method, and source of fusion, etc., metal-based AM technologies are mainly classified into powder bed fusion (PBF), direct energy deposition (DED), binder jetting (BJ) and sheet lamination [1], with the most industrial relevant metal-based AM technologies being PBF and DED [3]. Other emerging technologies such as metal infused filament deposition and metal-loaded photopolymerization are gaining momentum. The process of DED utilizes a nozzle and an energy source to deposit metal wire (wire fed) or powder (powder fed) onto an existing part directly. On the other hand, PBF uses a powder delivery system, which typically consists of a powder feed chamber and a build chamber, as well as a re-coater to spread powder from the feed to build chamber, layer

upon layer. Each layer is selectively melted by an energy source. The energy source used is typically a laser beam or an electron beam for both DED and PBF. The focus of this thesis is laser powder bed fusion (LPBF) process and the operation of a LPBF machine is described in details.

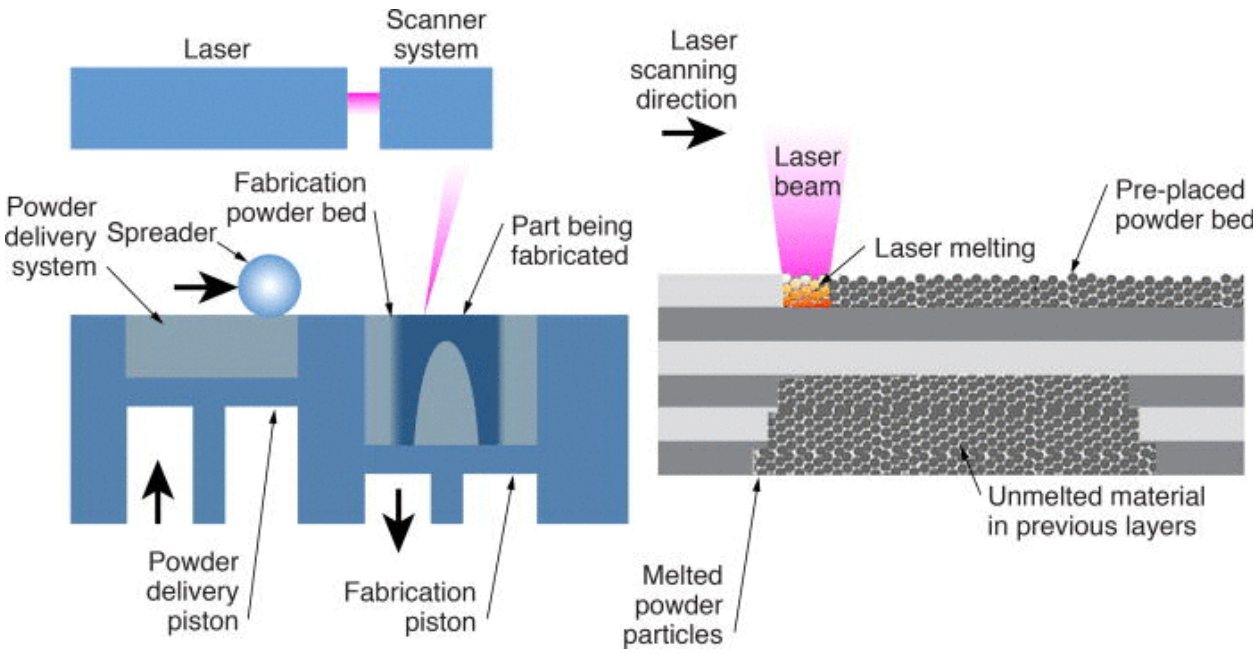

Figure 1: Process Overview of Laser Powder Bed Fusion [4].

Figure 1 is a schematic overview of the LPBF process. As is typical with current AM technologies, the LPBF process starts with an STL file, which is sliced into layers, with the beam path trajectory and parameters controlled selectively. To deposit a layer of powder, the powder delivery piston moves up and pushes the powder chamber filled with powder material upwards. Simultaneously, the fabrication piston lowers down by the amount as the specified layer thickness which is typically 20-100 μm [3] [5]. A re-coater rolls from the back of the powder chamber to the build chamber to smoothly deposit a thin layer of powder over the build platform. Another powder delivery mechanism is sometimes deployed, to deliver the powder through a hopper system and douse or dispense powder in front of the re-coater, as it travels across a build

bed. The high power laser beam, which is usually of 200 W to 1 KW [5], selectively scans across the build area as per digital 2D cross-section profile from the slice CAD model in order to melt and fuse the new layer of powder with previously solidified layers. Part resolution is therefore defined by layer thickness, laser beam parameters, and powder size characteristics. The powder deposition and melting process continues until the part is fully fabricated in an inert gas (e.g., argon, nitrogen) protective environment. At the end of the LPBF process, the un-melted powder is removed, leaving the printed parts welded onto the build plate directly, or through support structures. If necessary, the printed parts and the build plate are heat-treated for residual stress relief. After heat treatment, the parts are then removed from the build plate by wire EDM or other machining methods. The completed components can be tailored to achieve at best a typical dimensional accuracy of ±0.05 mm and a surface roughness of 9-16 μm with powder bed/fed technology, depending on geometry and process parameters [3]. In general, when comparing metal laser AM processes, LPBF AM technologies can produce more complex parts with higher geometric resolution and accuracy than wire- or powder-fed metal AM technologies; however, wire fed AM is more suitable for the fabrication of large scale components due to high deposition rate. In this study, LPBF was selected as the manufacturing method of choice due to refined design requirements.

2.1.2 Design and manufacturing potentials via LPBF

AM is considered to have great potentials in complementing conventional manufacturing methods such as subtractive, formative, and joining processes in the near future. Promising features inherent from the nature of AM technologies can be generally categorized into aspects such as sustainability [6][7][8] , design freedom, cost efficiency, and simplicity. From a sustainability perspective, AM has the potential to enable production on demand, to shorten

supply chains and to localise production, to extend product life by part repair and maintenance, as well as to reduce waste of materials by adding materials layer by layer only at desired locations in contrast to subtractive manufacturing where materials are removed to achieve the part design [7]. In terms of part design, AM allows for consolidation of assemblies [9][10][11], integration of lattice structures for light weighting [12][13][14], realization of topology optimization (TO) for the high strength to weight ratio components [15][16][17][18][19], and customization of part design [20][21][22]. These benefits are carefully considered against cost factors when deciding on the most appropriate product manufacturing method. Depending on the product, there is often a breakeven point where the benefit in design complexity and/or time-to-market justifies the LPBF manufacturing choice.

For conventional manufacturing methods (machining, forming, etc.), cost models and technological capabilities are well understood and most product designs are typically optimized to significantly reduce manufacturing costs. In machining, for production of complex designs, expenses related to the customization of manufacturing tools such as cutters, moulds, fixtures, etc. for production could be cost-prohibitive. However, due to layer by layer digital fabrication, AM processes are usually tool-less which makes it cost effective for customized, small batch productions. Unlike subtractive manufacturing, which turns large amounts of material into chips in order to create the final shape, AM may be more suitable for the fabrication of complex parts made of expensive materials such as titanium and nickel alloys, as most materials used in the process go into the direct part fabrication.

With the development of AM technologies, of design tools, and of simulation software, it is possible to foresee that in the near future, it will be possible to automate the AM process from design to fabrication with minimal human interaction [23]. As AM is gaining increasing attention

from automotive [24][25], aerospace [26][27] and biomedical [28][29][14]sectors for the unique design possibilities that AM may be able offer, there is an increased need to streamline strategies for design optimization for not only AM considerations, but post-processing considerations as well. Figure 2 to Figure 5 provide an insight into design possibilities in AM for applications such as design consolidation of an aircraft nozzle (Figure 2), lattice structure integration into a spider bracket (Figure 3), topology optimization of a seat bracket (Figure 4) and customization of a complex cooling channel (Figure 5). These figures also illustrate the challenges in post-processing such complex structures.

Figure 2: 3D printed nozzle combining 20 parts into one by GE [30].

Figure 3: Spider bracket with integrated lattice structures by Renishaw [31].

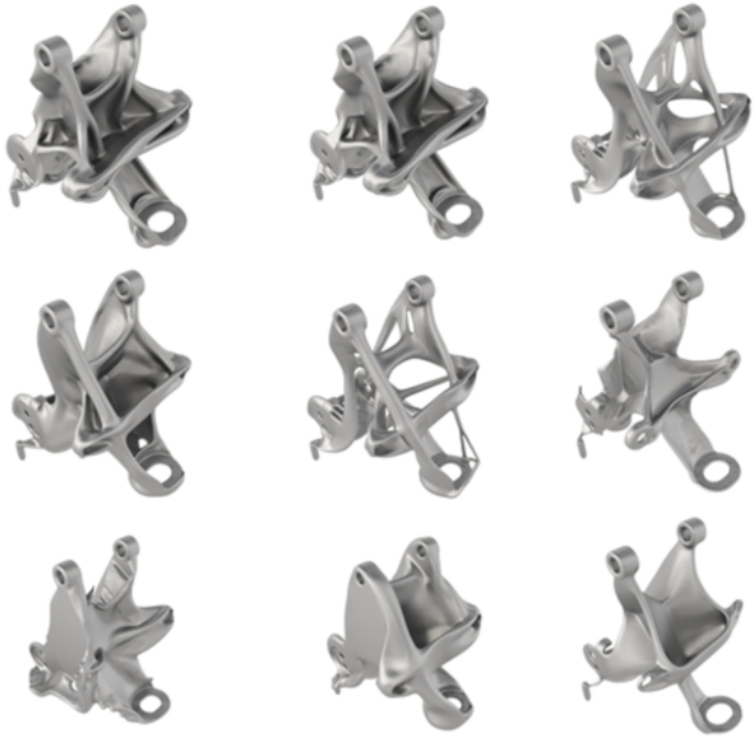

Figure 4: Seat bracket topology optimization by GE and Autodesk [32].

Figure 5: 3D printed cooling channel by AMM [33].

2.1.3 Topology optimization

Structural topology optimization has been developed for over a century, with the goal to generate designs with optimal material distribution under specific loading and boundary conditions and constraints. AM, owing to its minimal limitations on shape and complexity of the design, is seen as a manufacturing method that fills the manufacturing gap between topology optimization and end application [15]. The following is a brief review of two finite element based structural topology optimization methods for the purpose of providing a background into the design tools and decisions adopted in this thesis work.

One popular density-based method is the Solid Isotropic Material with Penalization (SIMP) algorithm (Figure 6) [34]. This method represents a design space by finite elements and defines the density of each element as a design variable taking a value from 0 to 1 with '0' indicating a

void and ‘1’ a fully dense element. Other elemental material properties are assumed to be proportional to the elemental density. A penalty value is usually used to solve the issue of having intermediate densities which is hard to realize in traditional manufacturing methods (Figure 7); the penalty value is used to binarize the final optimized domain. The objective (compliance) for the optimization may be to minimize weight or to minimize strain energy which is equivalent to maximizing stiffness under specific loadings, while satisfying the density and volume fraction constraints. Finite element analysis is performed at the beginning of each iteration. A sensitivity analysis is performed, which calculates the amount of total compliance change with respect to elemental density change. A sensitivity filter is often applied in order to avoid checkerboard patterns (Figure 8) and to obtain a smooth and connected structure. Design space mass layout is updated based on the results of sensitivity analysis and filtering. Iteration continues until compliance converges.

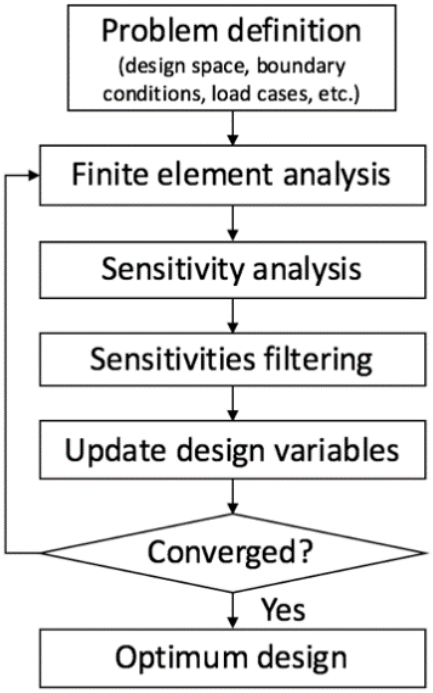

Figure 6: Flow chart of SIMP algorithm.

Figure 7: Void (white), intermediate densities (grey), and full dense elements (black) [35].

Figure 8: Checkerboard pattern [36].

Another popular type of finite element-based method is the bi-directional evolutionary optimization (BESO) method (Figure 9) [37]. The BESO method is similar to the SIMP method in terms of performing iterations of element distribution updates based on finite element analysis results. However, in this method, an element can only either be a void with a density value of '0' or a full dense element with a density value of '1'. Although the issue of intermediated densities is not a concern for this method, sensitivity filtering may still be necessary for eliminating checkerboard patterns. A final volume is usually predefined and based on the volume from the previous iteration, a target volume of the current iteration is updated. For example, if the previously obtained volume is smaller than the final volume, the target volume of the current iteration should increase, otherwise it should decrease. As a result, the structure evolves towards

the final volume. Based on the target volume, upper and lower threshold sensitivity values are computed. Elements with a sensitivity larger than the upper sensitivity threshold will be added to the structure while elements with a sensitivity smaller than the lower sensitivity threshold will be excluded. Iterations continues until the compliance converges and the final volume is reached.

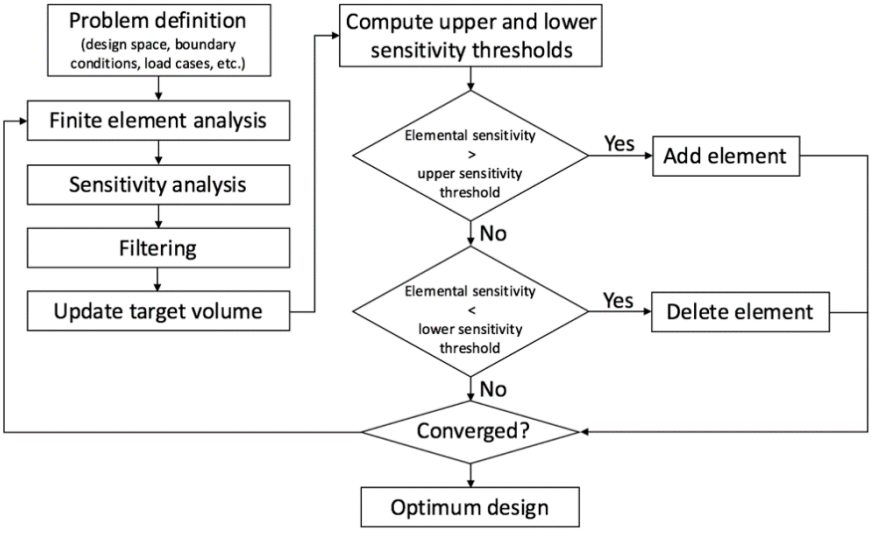

Figure 9: Flow chart of BESO algorithm.

Other topology optimization approaches include the homogenization method [38], the truss-based ground structure method [39], the boundary variation level set method [40], and more. Detailed descriptions are beyond the scope of this thesis. In this thesis, the SIMP method will be explored as it is the most developed and implemented method in commercial software.

Although AM allows for design freedom that traditional manufacturing may not be able to offer, there are manufacturing constraints inherent from the AM process which need to be considered before topologically optimized structures can be realised by AM. AM-related manufacturing constraints include: minimization of support structures required for overhangs, considerations on minimum feature size achievable, avoiding of enclosed voids to enable powder or support material removal, access to support structure removal, achievable cross section area

perpendicular to build direction to avoid distortion and part over-heating, connectivity of the optimized part, etc. Typically, these constraints are either incorporated in the topology optimization algorithm to generate manufacturable designs, or by subsequent modification of the unconstrained design [16].

Researchers have been exploring different solutions to create topology optimized designs that are also feasible for AM. Brackett et al. [16] assessed the angles and the overhang distance of downward facing edges at each iteration. A penalty function of overhang angle and distance is used to quantify violation of self-supporting requirements. The penalty function is then combined with the structural response to form a single objective function. This way support structure elimination is incorporated with the BESO algorithm. Aremu et al. [41] investigated the effect of BESO optimization parameters on the design. It was found that by reducing checkerboard filter radius, design complexity is increased which may eliminate large overhangs; however, there is limited control of the final structure. Langelaar et al. [19][42] implemented an additive manufacturing filter as part of the SIMP algorithm in both 2D and 3D to generate self-supporting structures. Zegard et al. [15] obtained optimized designs by SIMP and ground structure methods and post-processed the designs to make them feasible for AM.

In fact, post-processing of the obtained optimized design is typically inevitable to create a smooth, connected, or self-supported part ready for AM. It should be aware that the performance of the modified design may need to be reinvestigated since the objectives reached by the optimization process may have been violated. In this thesis work, the topologically optimized structure was processed into a manufacturable design using various software tools, with the iterative performance analysis approach described.

2.1.4 Challenges in LPBF

Despite the advantages and potentials of AM mentioned above, there are inherent drawbacks that hinder the widespread adoption of AM technologies. Compared to subtractive manufacturing (SM) methods, current metal-AM methods still suffer from poor surface finish and part dimensional inaccuracies [43]. For LPBF, partially melted powders tend to adhere to surfaces of the solidified part, which results in a rough surface. Researchers have found that surface roughness is dependent on surface and overhang angles, as well as process parameters [44][45][46]. Internal and sub-surface pores are prone to occur in AM parts, which may affect the parts' mechanical properties [47][48]. Internal and sub-surface porous defects can act as crack initiation points and therefore reduce fatigue life and tensile performance of AM functional components [49][50][51]. Associated with build orientation and process parameters, AM parts usually exhibit anisotropic mechanical properties such as tensile and fatigue behaviors with the Z-direction generally being the weakest [52][53]. In addition, due to the repeated, rapid, and concentrated thermal cycle, residual stresses are developed in AM parts, which then lead to geometric distortions and dimensional inaccuracies after part removal from the build plate [54][55]. Post-processes are necessary to attain the desired functional parts.

Heat treatment and hot isostatic pressing (HIP) are required to improve mechanical properties of AM parts [56][57][58]. As-built surfaces are also usually polished by sandblasting, electro-polishing, machining, laser etching, etc. There may also be a need to post-machine high precision features such as mating surface, holes and threads. Although AM has competitive advantages in producing complex components, design freedom is restricted by manufacturing constraints such as overhangs which require support structures, and thus also require a support structure removal process. For LPBF process, overhangs of angles smaller than 45° with respect to the build plate

generally require support structures [59][60]. Another challenge is that AM part size is still limited by the machine build volume, especially for LPBF. For example, Renishaw's RenAM 500Q multi-laser powder bed AM system has a build volume of 250 x 250 x 350 mm [61] and the build volume of EOS M 400-4 quad-laser system is 400 x 400 x 400 mm [62]. Also, it is not easy to maintain process repeatability and consistency from machine to machine or even from location to location on the build plate in the same machine, as part quality is sensitive to the systematic biases in the print environment [63].

Accurate process simulation and planning is essential for avoiding cost ineffective and time consuming trial and error experiments; however, accurate simulation may be computationally expensive as AM processes involve complicated multi-scale physics. There is still an overall lack of a comprehensive set of design principles, manufacturing guidelines, standardization and validation of AM parts [64]. In this thesis work, the focus is on understanding the design workflow for manufacturability for both AM and SM, with a direct application in high-value surgical tooling with complex topologies.

2.2 Additive manufacturing of surgical tooling and implants

2.2.1 Brief overview of metal implant fabrication via AM

In recent years, the development of AM technologies has enabled the short series production of customized biomedical implants with added value. Traditionally, mass-produced implants usually have poor individual fitment. As a result, biocompatible metallic implants with sufficient density are being manufactured utilizing recently advanced techniques such as Direct Metal Sintering (DMLS), Selective Laser Sintering (SLS), Selective Laser Melting (SLM) and Electron Beam Melting (EBM) [65]. Biomaterials suitable for metal implants include titanium, titanium

alloys, cobalt chrome, stainless steel and gold [66]. Tuomi et al. classified the AM application in medical into five major areas: (1) medical models, (2) surgical implant, (3) surgical guides, (4) external aids, and (5) bio-manufacturing [67].

With AM and computed tomography (CT) scanning technologies, more precise, customized implants can be designed and fabricated cost-effectively. The recent advancement in AM technologies is leading to an exponential growth of AM applications in the medical sector. Statistics from Scopus shows in 2014, there were only three articles published in the area of metal AM biomedical applications. The total research papers in this area increased to 426 with 133 articles published in 2016 [65].

There are numerous examples of surgical instruments and implants produced via LPBF. An additively manufactured EOS Titanium Ti64 EII reconstruction plate, which features a volumetric network structure with adjustable thickness to provide enough stiffness has been successfully implanted onto a patient's injured orbital wall (Figure 10) [68].

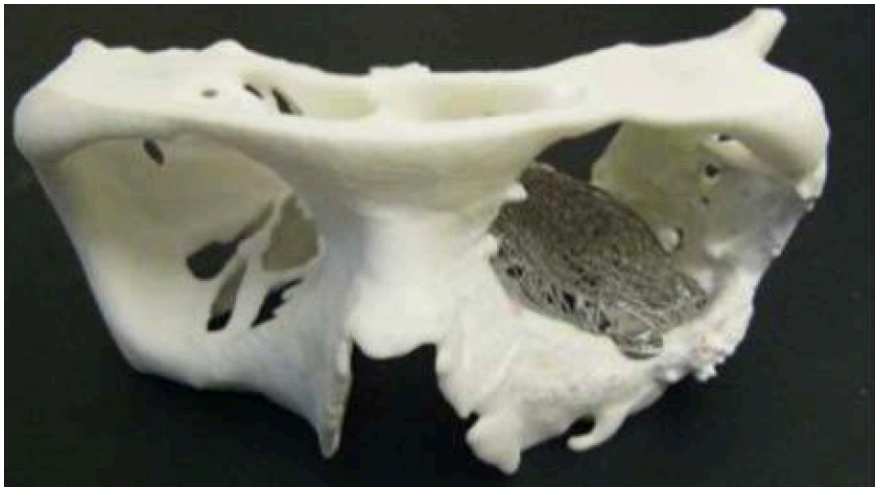

Figure 10: Ti64 reconstruction plate printed by EOS [68].

Another example is the personalized knee femoral component fabricated by SLM with CoCrMo-alloyed powder (Figure 11). The printed part is then post-processed in order to fulfill

requirements for mechanical properties, surface roughness and biological corrosion resistance of the implant [69].

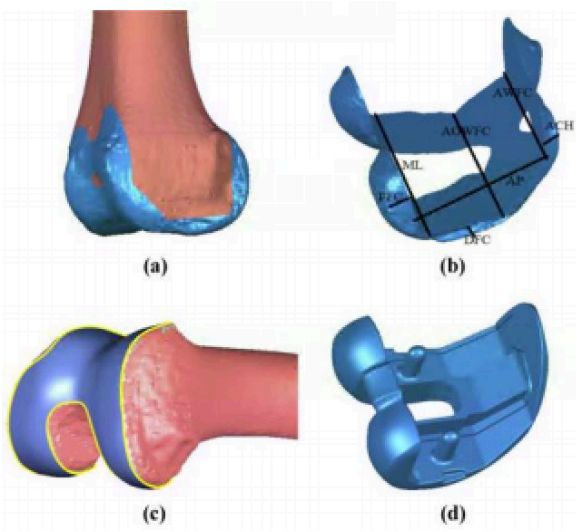

Figure 11: Personalized femoral component design process [69].

Topological design and additive manufacturing of porous metals for bone scaffolds and orthopaedic implants have found themselves to be suitable candidates for replacing damage bones since their stiffness and porosity can be theoretically adjusted as required (Figure 12). In addition, porous structures allow for the in-growth of bone tissue, hence accelerating the osseointegration process [70].

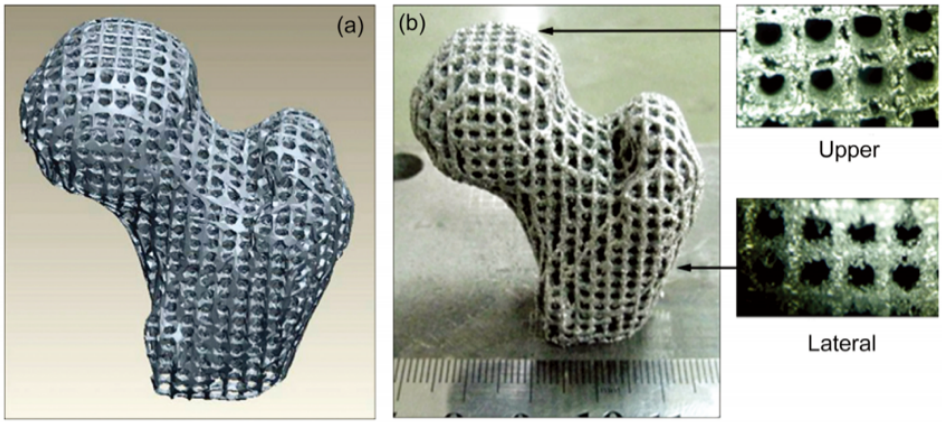

Figure 12: Porous titanium femoral bone implant [71].

2.2.2 Brief overview of metal surgical tooling fabrication via AM

AM technologies have also been applied in the field of surgical tooling due to the capability to manufacture customized tools on demand. The device for holding the needle during suturing as shown in Figure 13 [72] was redesigned to be manufactured using AM to get rid of the joints between components such that a smaller, simpler, and more precise grasping device was able to be realized. Large-scale plastic prototypes were first printed and examined before manufacturing the actual product in stainless steel via LPBF [72].

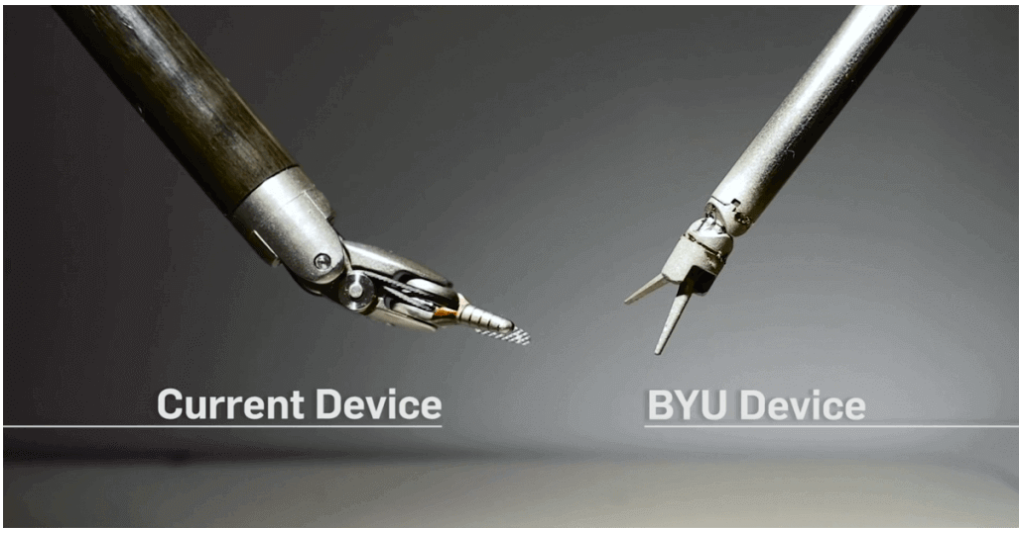

Figure 13: Conventional and printed origami-inspired surgical tools [72].

Stratasys manufactured a more flexible and accurate tool used in ACL reconstruction surgery by utilizing LPBF of Inconel 718 alloy [73], as seen in Figure 14. Many more examples of surgical tools fabricated via LPBF are emerging, showcasing the design and fabrication possibilities and capabilities of this technology.

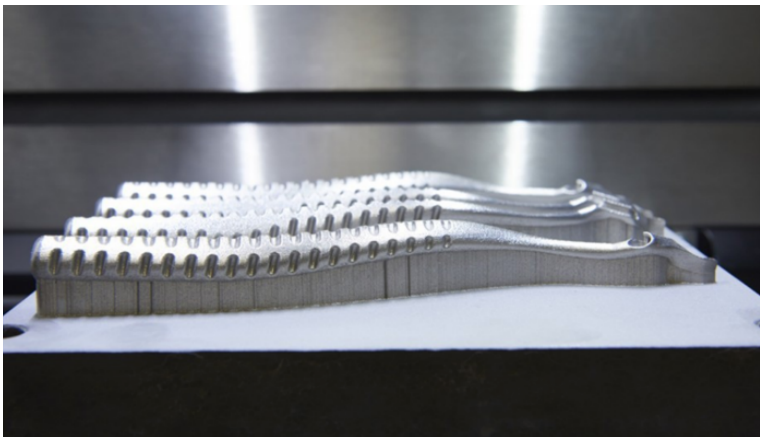

Figure 14: "Pathfinder" ACL reconstruction surgical tool manufactured by Stratasys [73].

2.2.3 Tracker demonstrator

In this thesis work, a surgical navigation tracker (Figure 15) is provided as a case study for AM redesign and fabrication by Intellijoint Surgical Inc. The surgical tracker is used to provide intraoperative measurements of femur position and orientation via optical navigation during hip replacement surgeries. The original tracker is an assembly consisting of a Ti6Al4V (Ti64) base, an Al 6061-T6 bracket, a pin, a screw, and four SS 17-4 posts of which the tips are press-fitted with reflective spheres. A camera mounted on the patient's pelvis takes images of the reflective spheres mounted on the tracker, while the tracker is probing on several locations on the patient's leg in order to calculate cup position, leg length and offset.

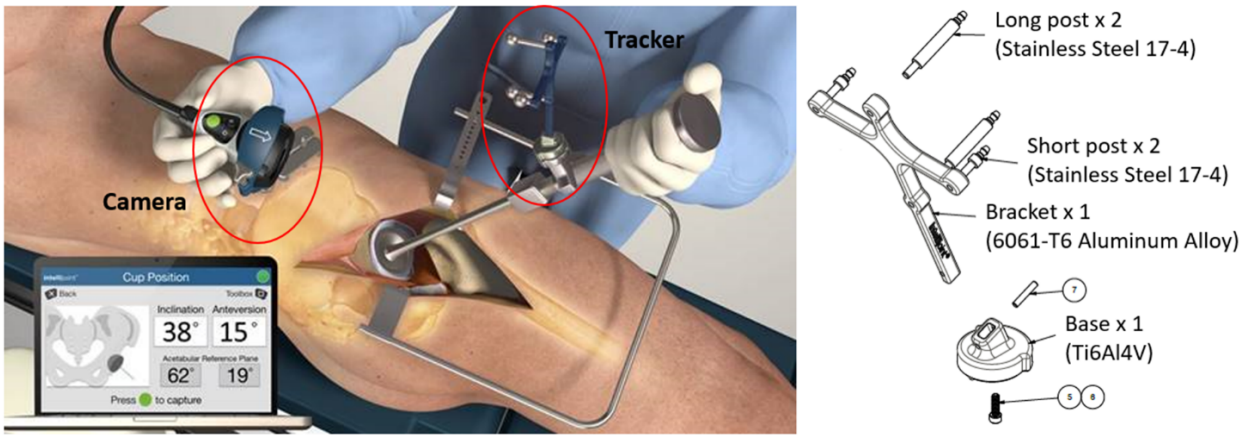

Figure 15: Original design of the surgical tracker (courtesy of Intellijoint Surgical).

The most important constraint of the design is that the dimensional tolerance of the location of the spheres referenced to the bottom surface of the base should be within ±25 μm overall displacement. In the present assembly, the specified tolerance is hard to achieve due to dimensional uncertainty accumulated during machining and assembly, where currently, the parts are press-fitted. With AM, it is possible to consolidate the original design and to print the entire part using Ti64. A high strength-to-weight ratio design can be obtained using structural topology optimization and the optimized, complex structure can be realized by LPBF. In parallel, manufacturing constraints imposed by the AM process, such as part orientation and overhangs, need to be considered in the design stage. For this case study, the print orientation constraint has been chosen with the bottom surface of the tracker being parallel to the build plate as shown for a family of designs in Figure 16. The selected orientation not only reduces unit cost of parts by accommodating more trackers on one build plate, but also minimizes thermally induced geometric distortion by avoiding large section variability between print layers. Structurally optimized parts may contain overhangs, which require support structures. As a result, the structural topology design constraint is to create self-supporting parts (Figure 16) which do not require support structures nor any following support removal post-processing. The design strategy to enable assembly consolidation, overhang reduction or avoidance, and minimization of product distortion due to thermal stresses will be described in detail in this thesis.

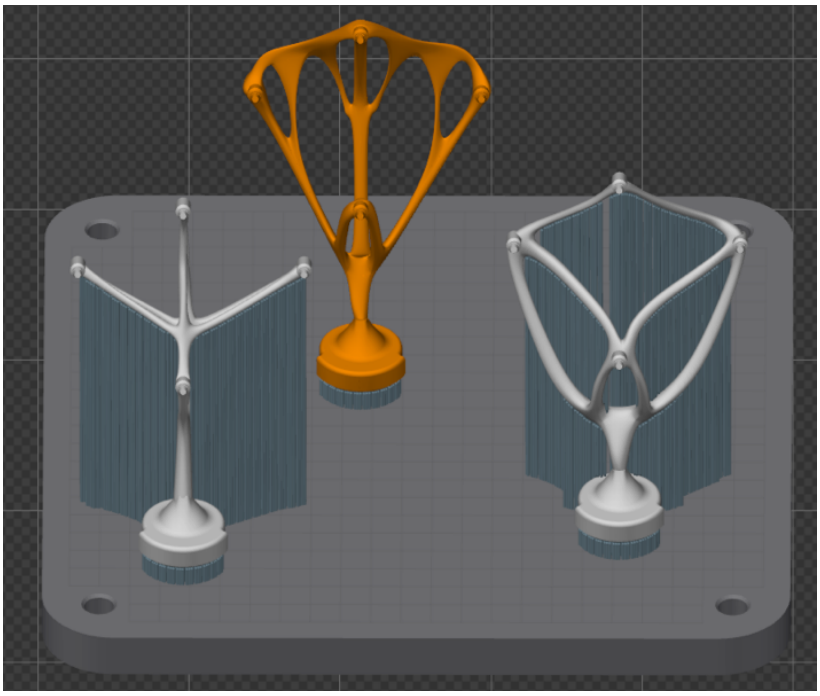

Figure 16: Self-supporting (golden) vs. non-self-supporting (silver) parts on the build plate.

In addition, critical mating surfaces can be machined after the part is printed to fulfil positional and dimensional precision. Two fixturing methods were used for mounting the complex, light-weight structure on the CNC machine, with design features propagating in the topology optimization stage to enable machining fixturing as will be described in this thesis.

The performance of the fixturing methods were compared in terms of vibration minimization. AM thermal distortion simulations, and subtractive machining (SM) experimental datasets and simulations were essential for effective planning of the synergized manufacturing processes in order to avoid costly iteration in experiments and part scrap during the post-processing step. In this work, it was identified that the design optimization has to consider both AM manufacturability and SM machinability potentials and capabilities.

2.3 Synergy of AM and SM strategies

2.3.1 Hybrid manufacturing systems or workflow solutions

In 2011, the International Academy for Production Engineering (CIRP) proposed an open definition for hybrid manufacturing as "a process that combines two or more established manufacturing processes into a new combined set-up whereby the advantages of each discrete process can be exploited synergistically" [74]. Major hybrid processes includes additive and subtractive processes, subtractive and joining processes, additive and transformative processes, and subtractive and transformative processes [75]. By the synergy of AM and SM, complex, lightweight parts can be fabricated using AM and tolerance requirements can be fulfilled by SM. For hybrid AM and SM processes, there are mainly two approaches which are integrated, alternating AM and SM processes and separated, successive processes. DMG MORI's LASERTEC 65 3D hybrid machine (Figure 17) [76] and similarly, Mazak's VC-500 AM machine [77] combine laser metal deposition with CNC milling by integrating a laser powder nozzle within a 5 axis milling machine.

Figure 17: LASERTEC 65 3D hybrid [76].

Sodick's OPM250L machine (Figure 18) combines laser metal sintering and high speed milling in a single machine. High speed milling is performed after printing several layers and the processes are alternated until the final part is fabricated [78].

Figure 18: OPM250L [78].

An AIMS (Additive systems Integrated with subtractive MethodS) process (Figure 19) has been proposed which theoretically combines any type of AM processes with post CNC RP (rapid prototyping) [43]. AIMS uses separate AM and SM machines which can be running simultaneously. AM is deployed for near-net shape fabrication while CNC RP in a 4-axis CNC machine is used for surface finishing. Fixturing features for CNC machining was integrated into part design.

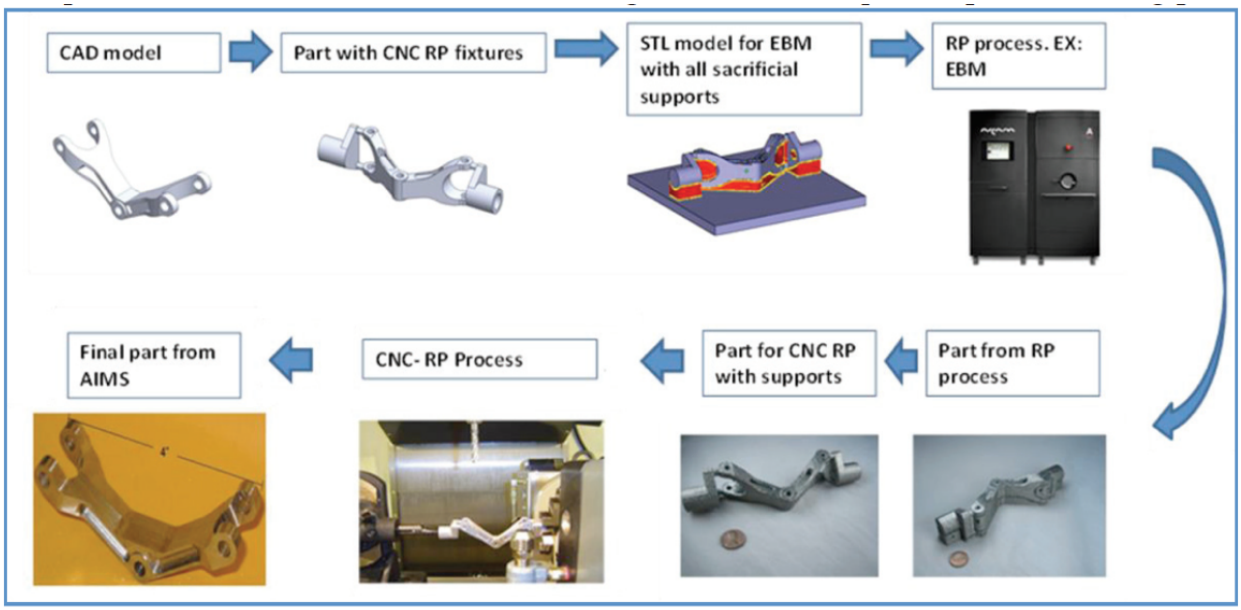

Figure 19: AIMS process [43].

A hybrid workflow intended for the production of injection moulding tooling inserts with conformal cooling has been proposed (Figure 20). In the described process, the tooling is split into a large inserts which is suitable for CNC milling and a conformal cooling system which is built on top of the CNC machined part by LPBF [79]. For integrated AM and SM systems, coolant for the machining process is usually prohibited as it may interfere with the AM process. However, the use of coolant is not a concern for separated AM and SM processes. As a result, tool life can be extended. Also, different batches of production can be running in AM and SM machines simultaneously, which reduces overall manufacturing time. For integrated single

machine AM and SM systems, fixturing and datum alignment is usually unnecessary, as the part is welded on the build plate and the AM and SM processes share a common datum. However, after the part is removed from the build plate, it may deform due to residual stress and become out of tolerances.

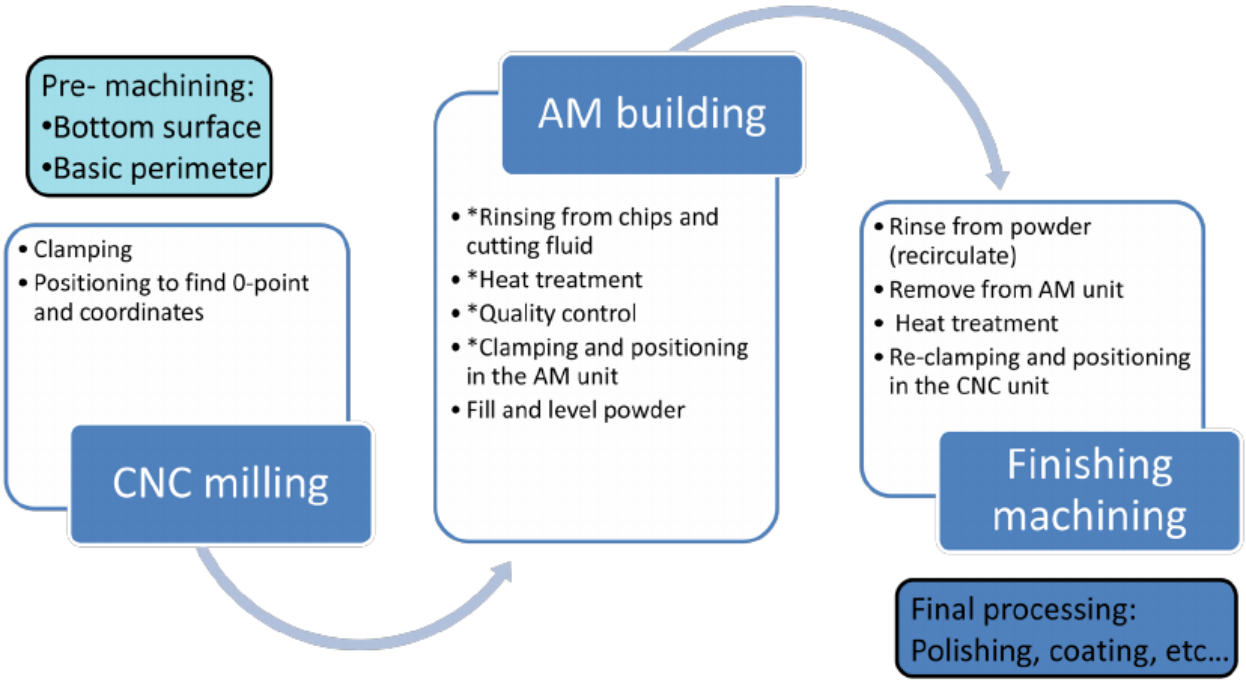

Figure 20: Workflow for the hybrid production of injection moulding tool inserts [79].

2.3.2 Case studies and challenges for post machining of AM parts

Challenges for the fabrication of AM parts followed by post-machining are inherent from the AM and CNC machining processes individually, as well as from the overlapping performance criteria for the two processes. Renishaw reported part vibration and fracture issues when machining lightweight AM structures due to the reduction in stiffness [80]. They also identified clamping a complex AM part in place in the CNC machine as a challenge. They 3D printed a plastic encapsulating fixture to mount a AM microwave guide on the CNC machining for surface finishing (Figure 21) [80].

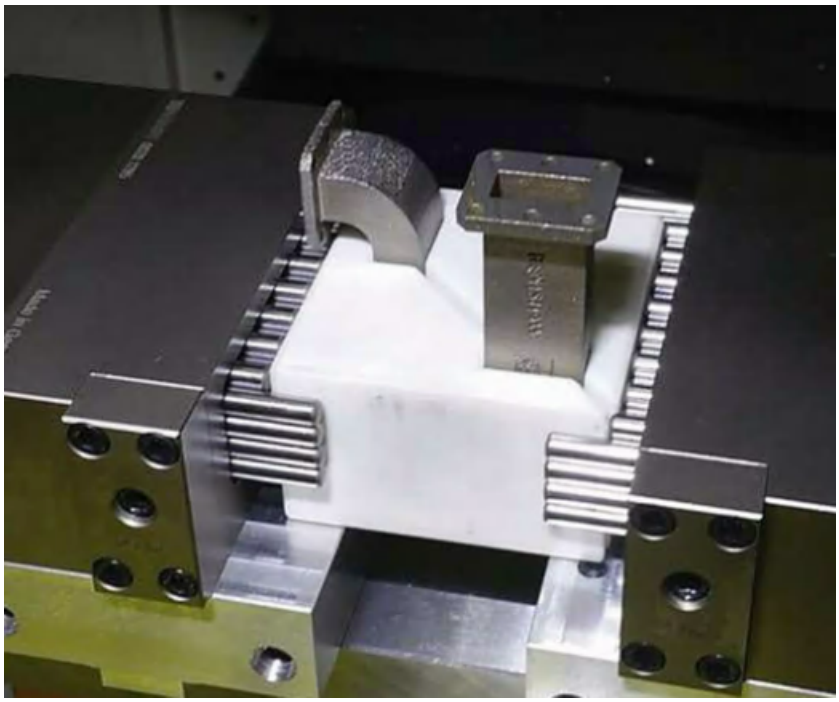

Figure 21: Encapsulating plastic fixture [80] .

Renishaw developed a "multi-point" probing alignment method to find the datum by performing "best fit" between the printed part axis and the machine axis in order to determine the excessive materials which need to be removed (Figure 22) [80].

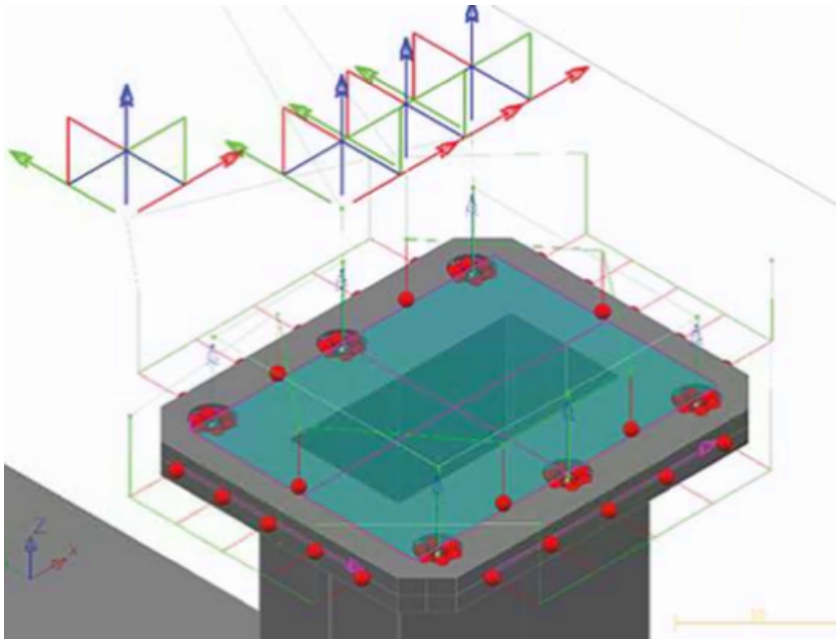

Figure 22: Alignment by probing [80].

Oyelola et al. [81] investigated the machining behaviour and surface integrity of Ti64 components produced by direct metal deposition. Results showed that the inhomogeneity in microstructure due to non-uniform heating and cooling from the AM process had effects on the cutting forces and chip formation [81]. Frank et al. [82], in the description of a direct additive-subtractive hybrid manufacturing (DASH) method, emphasized that it is important to identify features to be machined and their corresponding tolerances. Based on the identified features and cutter accessibility, plans for part orientation, fixation, and machining allowance should be considered as early as possible in the design stage. They laser-scanned the printed part and overlap the scanned data with the CAD model to determine excessive materials (Figure 23) [82].

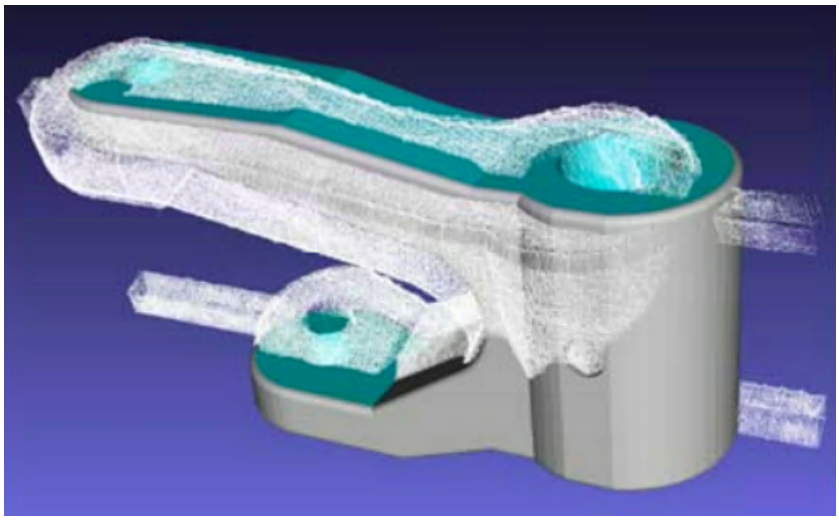

Figure 23: Laser scan of printed part and alignment with CAD model [82].

As these studies illustrate, there are challenges in harmonizing the AM and SM workflow to enable efficient utilization of both manufacturing strategies and avoid product scrap. This thesis work focuses on design optimization considering AM and SM constraints, AM process simulation to predict geometric distortion of AM part, validation of part geometry through 3D optical scan, post-machining strategies including clamping methods, alignment methods, and chatter free machining conditions.

2.4 LPBF process simulation for product distortion

In a typical LPBF process, important parameters include and are not limited to laser power, laser speed, layer thickness, scan pattern, and build orientation. These process parameters have significant effects on the melting mode and the cooling rate of the melted material and hence on the microstructure and residual stress of the printed part.

In order to plan for machining allowance and possibly to make geometric compensation to the CAD model, it is critical to be able to predict part distortion after printing accurately and computationally efficiently so that costly experiments can be avoided (Figure 24).

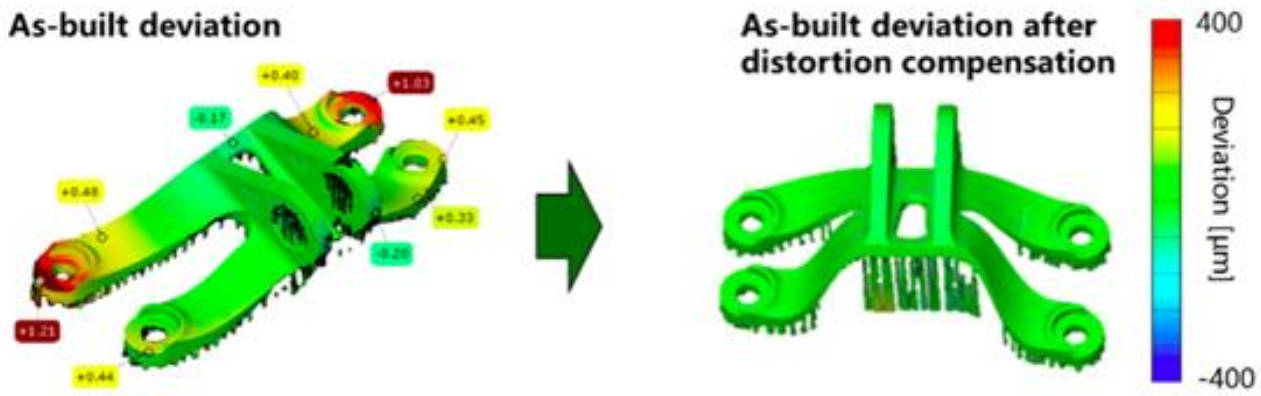

Figure 24: Deformation prediction and geometric compensation by Amphyon [83].

Different modelling methodologies of LPBF process for the fabrication of macroscale parts have been proposed in literature, which mainly include mechanical models and thermomechanical models. One example of mechanical models is the multi-scale stress thread method (Figure 25). In mesoscale, a stress thread model outputs local residual stress and uses it as an input in the mechanical macro part model to predict residual stress and distortion of the final part [84][85][86].

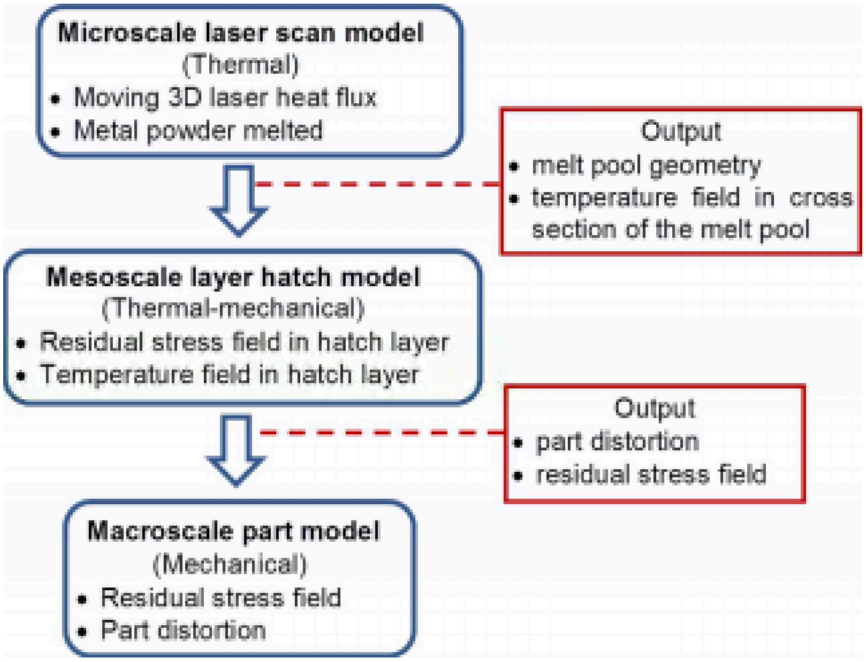

Figure 25: Multi-scale stress thread method [84].

Another example of mechanical models is the inherent shrinkage method (Figure 26). The main assumption of this method is that the most significant driving factor for distortion is the linear thermal contraction of the melted metal on cooling. A pure mechanical elastoplastic analysis is performed by introducing equivalent thermal loads in the finite element (FE) model in selected stacks of meshing layers at the same time. Isotropic and non-isotropic thermal expansion coefficients can be used to take into account the effect of scan patterns and build orientation [87].

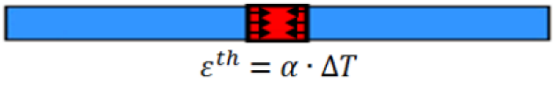

Figure 26: Inherent shrinkage method [87].

One simple thermomechanical FE model activates a stack of layers with uniform heat input [88]. In this method, temperature and residual stress field can be predicted but temperature gradient in x-y direction is neglected and the effect of scan pattern is not simulated. A non-uniform heat

input on multiple layers method (Figure 27) was proposed to take into account scan pattern associated part distortion [89].

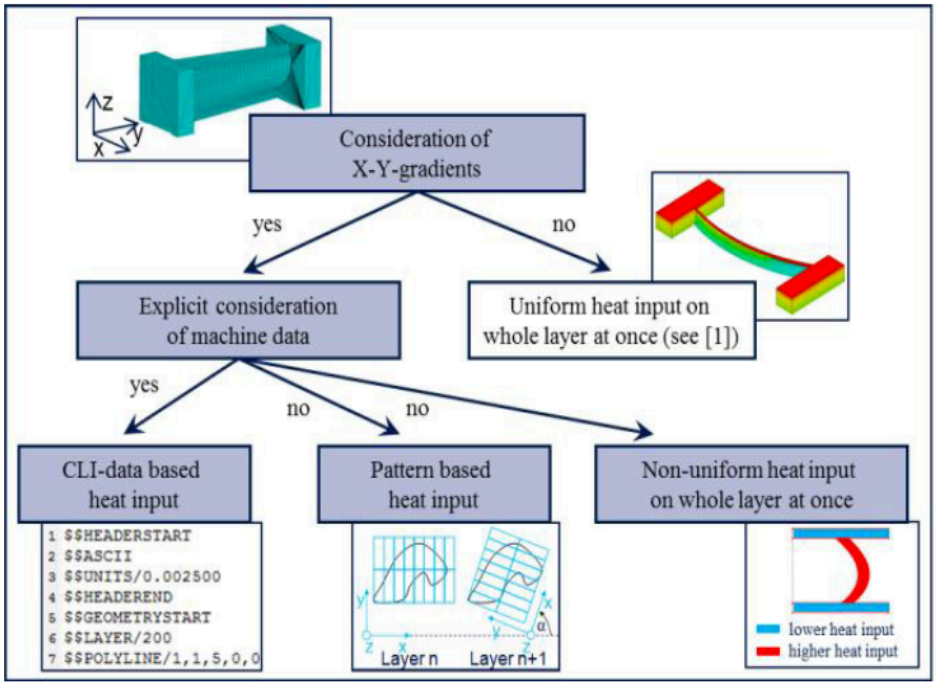

Figure 27: Uniform and non-uniform heat input models [89].

The thermomechanical multi-scale temperature thread FE model calculates an equivalent body heat flux from a micro-scale model in which thermal history of the melt pool center is used for developing an equivalent heat source (Figure 28 (a)). The obtained equivalent heat flux is imported as the "temperature thread" to a mesoscale layer hatch model to calculate the temperature field of the hatched layer (Figure 28 (b)). Lastly, the hatched layer with temperature field is used as a basic unit to build up the macro geometry (Figure 28 (c)) [90]. A few simulation softwares such as Amphyon® by Additive Works and Simufact Additive® by MSC implemented such model. In this thesis, the Simufact Additive® software engine was deployed.

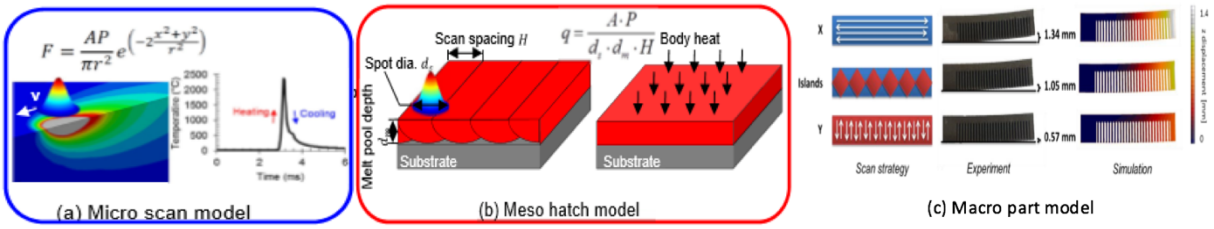

Figure 28: Multi-scale temperature thread model [90].

In order to capture most of the physics of the AM process and to save computational time at the same time, a dynamic adaptive mesh method has been proposed. The laser beam is the regime with highest thermal gradients and therefore a fine mesh with sub-beam diameter element size used for this zone and its neighboring heat affected zone is able to produce near-accurate results. A relatively coarse mesh has been employed in the surrounding areas (Figure 29) [91][92][93]. A commercially available simulation software – 3DSIM is implemented based on this model and shows promise in reducing computation time while maintaining accurate predictions. This algorithm was not tested in the context of this thesis.

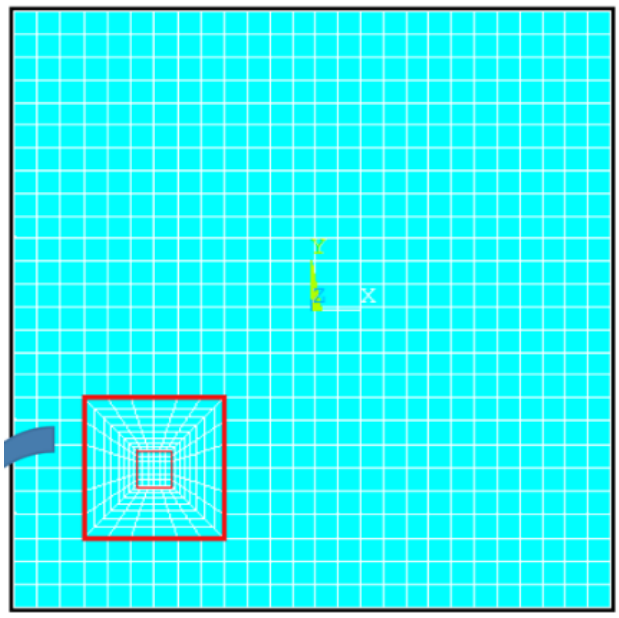

Figure 29: Dynamic adaptive mesh [91].

The inherent strain method with calibration is an approach based on using a calibrated analytical thermal model to derive functions that are implemented in a structural FEA (Figure 30). An intermediate step is introduced to calibrate the mechanical response using a specimen. The model needs to be recalibrated for different materials and process parameter sets. One of the simulation models of Simufact Additive® is based on this method.

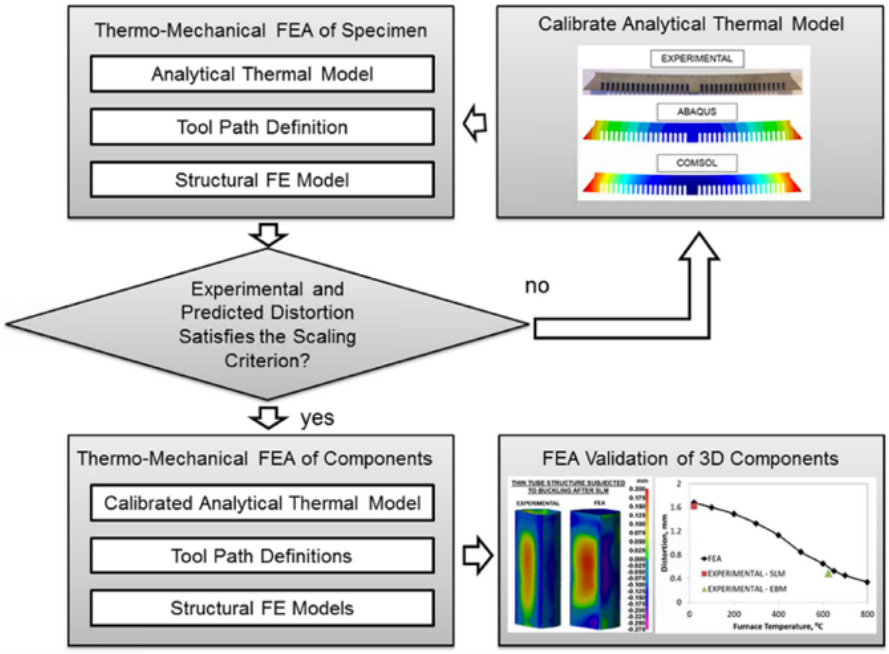

Figure 30: Inherent strain method with calibration [94].

In general, mechanical models are more computationally efficient than thermomechanical models. The limitation is that they are less accurate compared to thermomechanical models and usually no thermal history of the process is recorded.

Simufact Additive® was selected in this study to enable predictions of product distortion based on design features, product orientation, support structures, and process parameters. Due to the high number of design families simulated, computation time was a driving decision in the selection of the simulation software used. The simulated part distortion outcomes inform material allowance for machining processes.

2.5 CNC milling process simulation

2.5.1 Cutting force coefficients identification

It is important to identify cutting force coefficients for a specific tool-workpiece combination for the purpose of predicting cutting forces, chatter vibration, surface finish, and planning for the optimal machining parameters such as depth of cut, spindle speed and feed rate. In milling, there are mainly two basic approaches for identifying cutting force coefficients. One approach is to develop a database of cutting parameters such as shear angle, shear stress, and friction angle from orthogonal cutting tests for a specific tool-workpiece material combination. Given cutter geometry and the identified cutting parameters, cutting force coefficients can be calculated [95]. This idea can be briefly explained by the mechanistic model of orthogonal cutting and its transformation to oblique cutting.

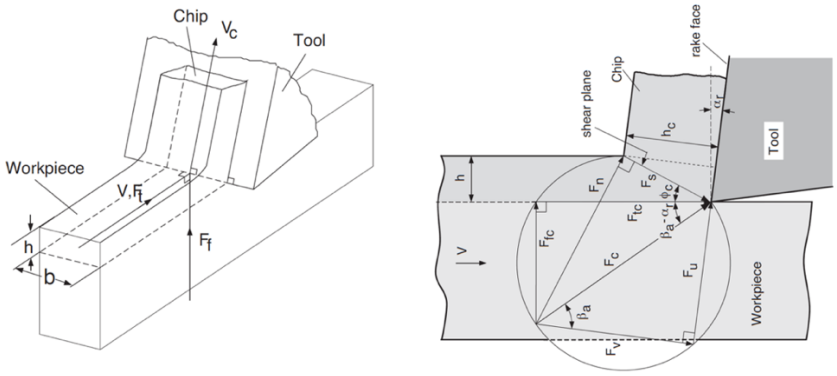

Figure 31: Mechanics of orthogonal cutting [96].

Figure 31 shows the mechanistic model of orthogonal cutting in which the edge of the cutter is perpendicular to the direction of relative tool motion. The shear angle ϕ_c, which is the angle between the shear plane and the cut surface, can be estimated from the geometry as:

$$\phi_c = \tan^{-1}\frac{r_c \cos\alpha_r}{1 - r_c \sin\alpha_r},\ r_c = \frac{h}{h_c}, \tag{2.5.1.1}$$

where r_c is the chip compression ratio defined as the uncut chip thickness (h) over the deformed one (h_c) and α_r is the rake angle. Alternatively, the shear angle may be theoretically predicted based on the maximum shear stress principle or minimum energy principle.

The friction angle β_α, of which the tangent ($\tan\beta_\alpha$) indicates the friction coefficient on the rake face, can be found as:

$$\beta_\alpha = \alpha_r + \tan^{-1}\frac{F_f}{F_t}, \tag{2.5.1.2}$$

where F_f is the force acting in the feed direction and F_t is that in the tangential direction.

Finally, the shear stress τ_s on the shear plane can be calculated as:

$$\tau_s = \frac{F_s}{A_s} = \frac{(F_t \cos\phi_c - F_f \sin\phi_c)\sin\phi_c}{bh}, \tag{2.5.1.3}$$

where F_s is the shearing force, A_s is the shear plane area, and b is the width of cut.

Tangential and feed forces (F_t and F_f) can be measured using a dynamometer during orthogonal tests. Deformed chip thickness can be observed and measured under microscope. Cutter rake angle α_r can be measured or obtained from the supplier. Consequently, the cutting parameters are determined.

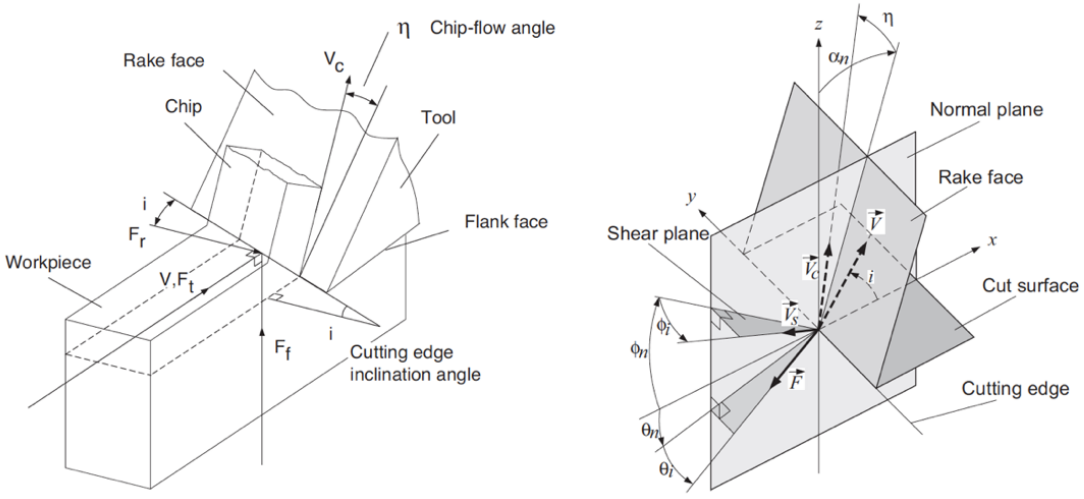

Figure 32: Mechanics of oblique cutting [96].

Figure 32 shows the mechanics of oblique cutting. In oblique cutting, the cutting velocity has an inclination angle i and cutting force exist in tangential, feed, and radial directions which are noted as F_t, F_f, and F_r respectively. Cutting forces are usually expressed in the following form:

$$F_t = K_{tc}bh + K_{te}b, \tag{2.5.1.4}$$

$$F_f = K_{fc}bh + K_{fe}b, \tag{2.5.1.5}$$

$$F_r = K_{rc}bh + K_{re}b, \tag{2.5.1.6}$$

where K_{tc}, K_{fc}, K_{rc}, K_{te}, K_{fe}, K_{re} are cutting force coefficients. K_{tc}, K_{fc}, and K_{rc} take into account the shearing effect due to the shearing of material. The shearing components of the cutting forces are proportional to the uncut chip area ($a = bh$). K_{te}, K_{fe}, and K_{re} correspond to the ploughing effect which is due to rubbing between the cutting edge and the cut surface. The ploughing components of the cutting forces are proportional to the width of cut (b). Using geometric relations, the shearing cutting coefficients can be represented as:

$$K_{tc} = \frac{\tau_s}{\sin\phi_n} \frac{\cos(\beta_n - \alpha_n) + \tan i \tan\eta \sin\beta_n}{\sqrt{\cos^2(\phi_n + \beta_n - \alpha_n) + \tan^2\eta \sin^2\beta_n}}, \quad (2.5.1.7)$$

$$K_{fc} = \frac{\tau_s}{\sin\phi_n \cos i} \frac{\sin(\beta_n - \alpha_n)}{\sqrt{\cos^2(\phi_n + \beta_n - \alpha_n) + \tan^2\eta \sin^2\beta_n}}, \quad (2.5.1.8)$$

$$K_{rc} = \frac{\tau_s}{\sin\phi_n} \frac{\cos(\beta_n - \alpha_n)\tan i - \tan\eta \sin\beta_n}{\sqrt{\cos^2(\phi_n + \beta_n - \alpha_n) + \tan^2\eta \sin^2\beta_n}}. \quad (2.5.1.9)$$

The oblique cutting coefficients may be predicted from the cutting parameters ϕ_c, τ_s, and β_α obtained from orthogonal cutting tests with the following assumptions: the normal shear angle and the normal friction angle in oblique cutting are the same as the shear angle and friction angle in orthogonal cutting ($\phi_c \equiv \phi_n, \beta_a \equiv \beta_n$); shear stress is the same in both orthogonal and oblique cutting; the normal rake angle in oblique cutting is the equal to the rake angle in orthogonal cutting ($\alpha_r \equiv \alpha_n$); and the chip flow angle is equal to the cutting edge inclination angle $\eta \equiv i$.

The tangential and feed edge coefficients (K_{te}, K_{fe}) are usually assumed to be the same as those identified in orthogonal cutting tests. The radial edge coefficient is usually small and negligible ($K_{re} \cong 0$). The orthogonal to oblique cutting transformation technique for cutting force coefficients prediction is usually used in cutter design when the cutter geometry is to be determined [95]. However, if the orthogonal cutting parameter database is not available or the cutter geometry is too complex, another cutting force coefficient identification method, which the shearing and edge cutting coefficients are calibrated against oblique cutting tests, may be applied.

In order to identify cutting coefficients of helical end milling using the second method, a set of milling tests need to be conducted at usually 5-6 different feed rates while keeping other machining conditions such as radial immersion, depth of cut, and spindle speed constant. The

cutting coefficients may be obtained by equating the measured average cutting forces to the analytically predicted average cutting forces and then performing linear regression analysis which assumes linear dependency of cutting forces on feed per tooth [96]. Some researchers calibrate cutting coefficients by performing a least squares fit of simulated cutting forces to measured cutting forces. In this method, only one milling test is required and the cutting force coefficients are specific to the machining conditions and tool-workpiece combination chosen [97].

End milling cutting forces can be predicted using discrete simulation, given machining conditions, tool geometry and cutting coefficients [96]. In the milling process, the chip thickness varies periodically according to the tool workpiece engagement. The instantaneous chip thickness may be estimated by assuming uniform circular motion of the tool tip as [96]:

$$h(\phi) = c \sin \phi, \tag{2.5.1.10}$$

where c is the feed per tooth and ϕ is the instantaneous immersion angle. The instantaneous chip thickness is dependent on the immersion angle which varies along the axial location of the cutting edge at each tooth. Chip thickness is non-zero only when a tooth is engaged in cutting which is equivalent to $\phi_{st} \leq \phi_j \leq \phi_{ex}$, where ϕ_{st} and ϕ_{ex} are the start and exit immersion angles respectively and j is the tooth index. Some researchers consider the true trochoidal trajectory of the tool tip due to radial run-out when computing instantaneous chip thickness, and some researchers take into account the effect of vibration when determining the instantaneous chip thickness.

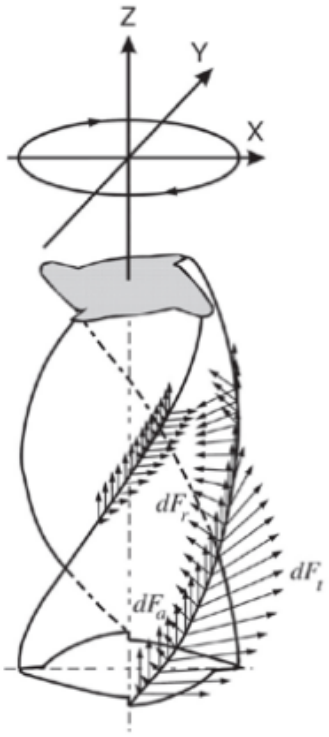

Figure 33: Discrete cutting force simulation of a helical end mill [98].

In order to predict cutting force analytically, a helical end mill can be discretized along the length (z-direction) of the cutter (Figure 33). Forces acting on discretized disks in tangential, radial, and axial directions were calculated based on the identified cutting force coefficients and the instantaneous chip thickness as follows:

$$dF_{t,j}(\phi, z) = (K_{tc} C_j(\phi_j(z)) + K_{te}) dz, \tag{2.5.1.11}$$

$$dF_{r,j}(\phi, z) = (K_{rc} C_j(\varphi_j(z)) + K_{re}) dz, \tag{2.5.1.12}$$

$$dF_{a,j}(\phi, z) = (K_{ac} C_j(\phi_j(z)) + K_{ae}) dz. \tag{2.5.1.13}$$

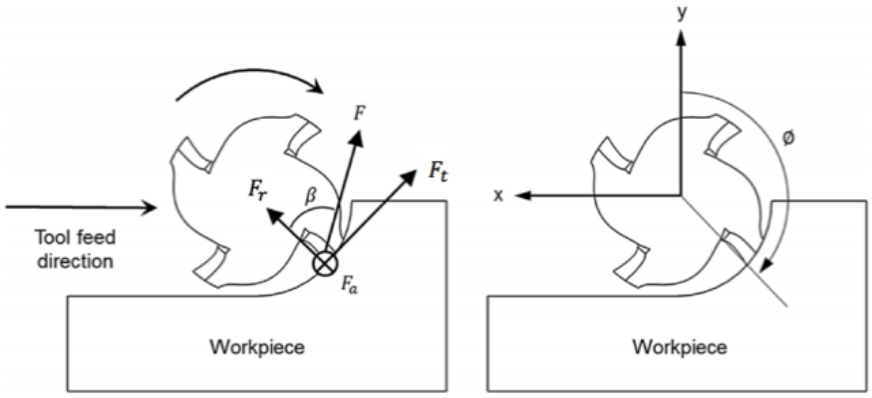

Figure 34: Down milling and the fixed X-Y-Z coordinate [99].

Projecting the tangential, normal, and axial forces into the fixed X-Y-Z coordinate (Figure 34) and averaging over one cutter revolution yields the following average milling forces:

$$\bar{F}_x = \left\{\frac{Nac}{8\pi}[-K_{tc}\,cos\,2\phi + K_{rc}(2\phi - sin\,2\phi)] + \frac{Na}{2\pi}[K_{te}\,sin\,\phi - K_{re}\,cos\,\phi]\right\}_{\phi_s}^{\phi_e}, \tag{2.5.1.14}$$

$$\bar{F}_y = \left\{\frac{Nac}{8\pi}[K_{tc}(2\phi - \sin 2\phi) + K_{rc}\cos 2\phi] - \frac{Na}{2\pi}[K_{te}\cos\phi + K_{re}\sin\phi]\right\}_{\phi_s}^{\phi_e}, \tag{2.5.1.15}$$

$$\bar{F}_z = \left\{\frac{Na}{2\pi}[K_{ac}c\cos\phi - K_{ae}\phi]\right\}_{\phi_s}^{\phi_e}, \tag{2.5.1.16}$$

where N is the number of teeth on the cutter and a is the axial depth of cut. For arbitrary radial immersion milling, Equation (2.5.1.14)-(2.5.1.16) can be expanded and rearranged in slope-intercept form as [99]:

$$\bar{F}_x = a_{1x}c + a_{0x}, \tag{2.5.1.17}$$

$$\bar{F}_y = a_{1y}c + a_{0y}, \tag{2.5.1.18}$$

$$\bar{F}_z = a_{1z}c + a_{0z}, \tag{2.5.1.19}$$

where:

$$a_{1x} = \frac{Na}{8\pi}\{K_{tc}(\cos 2\phi_s - \cos 2\phi_e) + K_{rc}[(2\phi_e - \sin 2\phi_e) - (2\phi_s - \sin 2\phi_s)]\}, \quad (2.5.1.20)$$

$$a_{1y} = \frac{Na}{8\pi}\{K_{tc}[(2\phi_e - \sin 2\phi_e) - (2\phi_s - \sin 2\phi_s)] + K_{rc}(\cos 2\phi_e - \cos 2\phi_s)\}, \quad (2.5.1.21)$$

$$a_{1z} = \frac{Na}{2\pi}[K_{ac}(\cos \phi_e - \cos \phi_s)], \quad (2.5.1.22)$$

$$a_{0x} = \frac{Na}{2\pi}[K_{te}(\sin \phi_e - \sin \phi_s) + K_{re}(\cos \phi_s - \cos \phi_e)], \quad (2.5.1.23)$$

$$a_{0y} = \frac{Na}{2\pi}[K_{te}(\cos \phi_s - \cos \phi_e) + K_{re}(\sin \phi_s - \sin \phi_e)], \quad (2.5.1.24)$$

$$a_{0z} = \frac{Na}{2\pi}[K_{ae}(\phi_s - \phi_e)]. \quad (2.5.1.25)$$

The above equations show that average milling forces and feed per tooth have linear relationship with a_{1x}, a_{1y}, and a_{1z} being the slopes and a_{0x}, a_{0y}, and a_{0z} being the intercepts. Rewriting Equation (2.5.1.20)-(2.5.1.25) in matrix form yields [99]:

$$\begin{bmatrix} b_{11} & \cdots & b_{16} \\ \vdots & \ddots & \vdots \\ b_{61} & \cdots & b_{66} \end{bmatrix} \begin{Bmatrix} K_{tc} \\ K_{te} \\ K_{rc} \\ K_{re} \\ K_{ac} \\ K_{ae} \end{Bmatrix} = \begin{Bmatrix} a_{1x} \\ a_{0x} \\ a_{1y} \\ a_{0y} \\ a_{1z} \\ a_{0z} \end{Bmatrix}, \quad (2.5.1.26)$$

where:

$$b_{11} = \frac{Na}{8\pi}(\cos 2\phi_s - \cos 2\phi_e), \quad (2.5.1.27)$$

$$b_{13} = \frac{Na}{8\pi}[(2\phi_e - 2\phi_s) + (\sin 2\phi_s - \sin 2\phi_e)], \quad (2.5.1.28)$$

$$b_{22} = \frac{Na}{2\pi}(\sin\phi_e - \sin\phi_s), \quad (2.5.1.29)$$

$$b_{24} = \frac{Na}{2\pi}(\cos\phi_s - \cos\phi_e), \quad (2.5.1.30)$$

$$b_{31} = \frac{Na}{8\pi}[(2\phi_e - 2\phi_s) + (\sin 2\phi_s - \sin 2\phi_e)], \quad (2.5.1.31)$$

$$b_{33} = \frac{Na}{8\pi}(\cos 2\phi_e - \cos 2\phi_s), \quad (2.5.1.32)$$

$$b_{42} = \frac{Na}{2\pi}(\cos\phi_s - \cos\phi_e), \quad (2.5.1.33)$$

$$b_{44} = \frac{Na}{2\pi}(\sin\phi_s - \sin\phi_e), \quad (2.5.1.34)$$

$$b_{55} = \frac{Na}{2\pi}(\cos\phi_e - \cos\phi_s), \quad (2.5.1.35)$$

$$b_{66} = \frac{Na}{2\pi}(\phi_s - \phi_e). \quad (2.5.1.36)$$

All other b elements are equal to zero. The slopes (a_{1x}, a_{1y}, a_{1z}) and intercepts (a_{0x}, a_{0y}, a_{0z}) can be estimated experimentally by performing linear regression analysis of the measured average cutting forces over a range of feed per tooth values. As a result, cutting force coefficients are solved according to Equation (2.5.1.26).

2.5.2 Chatter stability analysis

Machine tool and workpiece vibration play an important role in dimension accuracy, tool durability and process productivity. The scope of this thesis work is on avoiding milling regenerative chatter vibration of cutter tool and thin and flexible AM workpiece by determining optimum depth of cut and spindle speed during post-machining. Chatter vibrations are caused by a self-excitation mechanism. One of the structural modes of the tool-workpiece system is initially excited by cutting forces and as a result, each tooth of the milling tool leaves a wavy surface

finish. Chip thickness may grow exponentially at a chatter frequency depending on the phase shift between two succeeding waves [96]. Tobias [100] first introduced linear chatter stability models for orthogonal cutting. In orthogonal cutting, the cutting force direction remains unchanged. However, in milling, the cutting forces vary along the helical edge of the cutter and the process is intermittent and periodic. Insperger and Stepan developed a semi-discrete time domain model for milling chatter stability [101]. Tlusty et al. [102] proposed a time domain simulation approach to analysis chatter in high speed milling. Altintas and Budak [103] developed a two dimensional zero and higher order analytical solution of the milling chatter analysis. The zero order analytical solution willing be explained in the following paragraphs.

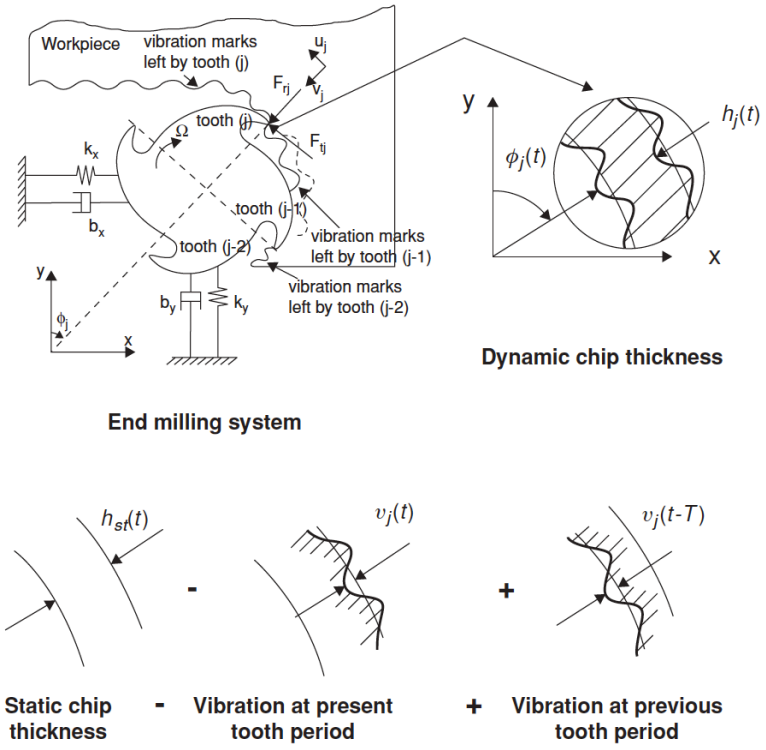

Figure 35: Milling chatter vibration in X and Y directions [96].

As it is shown in Figure 35, the dynamic chip thickness without the static part can be expressed as:

$$h(\phi_j) = (v_{j,0} - v_j)g(\phi_j), \tag{2.5.2.1}$$

where $v_{j,0}$ and v_j are the previous and present dynamic displacement of the cutter. The g function takes into account whether or not the tooth is in cut and it is defined as:

$$g(\phi_j) = \begin{cases} 1 & if\ \phi_{st} \le \phi_j \le \phi_{ex} \\ 0 & elsewhere \end{cases}. \tag{2.5.2.2}$$

The difference of the dynamic displacements can be projected into X and Y directions:

$$(v_{j,0} - v_j) = (x - x_0)\sin\phi_j + (y - y_0)\cos\phi_j, \tag{2.5.2.3}$$

$$\Delta v = \Delta x \sin\phi_j + \Delta y \cos\phi_j. \tag{2.5.2.4}$$

Substituting Equation (2.5.2.4) into Equation (2.5.2.1):

$$h(\phi_j) = (\Delta x \sin\phi_j + \Delta y \cos\phi_j)g(\phi_j). \tag{2.5.2.5}$$

Tangential and radial cutting forces are proportional to the uncut chip area (the axial force is neglected for simplicity):

$$F_{tj} = K_{tc} a h(\phi_j), \tag{2.5.2.6}$$

$$F_{rj} = K_{rc} a h(\phi_j) = K_r F_{tj}, \qquad K_r = \frac{K_{rc}}{K_{tc}}. \tag{2.5.2.7}$$

Projecting the tangential and radial cutting forces into X and Y directions:

$$F_{xj} = -K_{tc} a (\Delta x \sin\phi_j + \Delta y \cos\phi_j) g(\phi_j)(\cos\emptyset_j + K_r \sin\phi_j), \tag{2.5.2.8}$$

$$F_{yj} = -K_{tc} a (\Delta x \sin\phi_j + \Delta y \cos\phi_j) g(\phi_j)(\sin\phi_j + K_r \cos\phi_j). \tag{2.5.2.9}$$

The total cutting forces can be expressed as the summation of forces on all engaging teeth:

$$F_x = \sum_{j=0}^{N-1} F_{xj}, \tag{2.5.2.10}$$

$$F_y = \sum_{j=0}^{N-1} F_{yj}. \tag{2.5.2.11}$$

It can be rewritten in matrix form:

$$\begin{Bmatrix} F_x \\ F_y \end{Bmatrix} = \frac{1}{2} a K_{tc} \begin{bmatrix} a_{xx} & a_{xy} \\ a_{yx} & a_{yy} \end{bmatrix} \begin{Bmatrix} \Delta x \\ \Delta y \end{Bmatrix}. \tag{2.5.2.12}$$

The directional coefficient matrix depends on the milling mechanics and the matric elements a_{xx}, a_{xy}, a_{yx}, and a_{yy} can be expanded as:

$$a_{xx} = \sum_{j=0}^{N-1} -g_j \left[\sin\phi_j + K_r\left(1 - \cos 2\phi_j\right)\right], \tag{2.5.2.13}$$

$$a_{xy} = \sum_{j=0}^{N-1} -g_j \left[\left(1 + \cos\phi_j\right) + K_r \sin 2\phi_j\right], \tag{2.5.2.14}$$

$$a_{yx} = \sum_{j=0}^{N-1} g_j \left[\left(1 - \cos\phi_j\right) - K_r \sin 2\phi_j\right], \tag{2.5.2.15}$$

$$a_{yy} = \sum_{j=0}^{N-1} -g_j \left[\sin 2\phi_j - K_r\left(1 + \cos 2\phi_j\right)\right]. \tag{2.5.2.16}$$

Since the immersion angle $\emptyset_j$ is a function of time, the directional coefficient matrix and the dynamic displacements can be written with respect to time. Equation (2.5.2.12) can be rewritten as:

$$F(t) = \frac{1}{2} K_{tc} a A(t) \Delta(t). \tag{2.5.2.17}$$

To transfer the force function from the time domain into frequency domain, the Fourier series expansion of the force function can be taken since $A(t)$ is periodic. If the most simplistic approximation, the average component of the Fourier series expansion (zero order), is considered, then:

$$[A_0] = \frac{1}{T}\int_0^T [A(t)]dt = \frac{1}{\phi_p}\int_{\phi_{st}}^{\phi_{ex}} [A(\phi)]\, d\phi = \frac{N}{2\pi}\begin{bmatrix} b_{xx} & b_{xy} \\ b_{yx} & b_{yy} \end{bmatrix}. \quad (2.5.2.18)$$

Elements in the B matrix are:

$$b_{xx} = \frac{1}{2}[\cos 2\phi - 2K_r\phi + K_r \sin 2\phi]_{\phi_{st}}^{\phi_{ex}}, \quad (2.5.2.19)$$

$$b_{xy} = \frac{1}{2}[-\sin 2\phi - 2\phi + K_r \cos 2\phi]_{\phi_{st}}^{\phi_{ex}}, \quad (2.5.2.20)$$

$$b_{yx} = \frac{1}{2}[-\sin 2\phi + 2\phi + K_r \cos 2\phi]_{\phi_{st}}^{\phi_{ex}}, \quad (2.5.2.21)$$

$$b_{yy} = \frac{1}{2}[-\cos 2\phi - 2K_r\phi - K_r \sin 2\phi]_{\phi_{st}}^{\phi_{ex}}. \quad (2.5.2.22)$$

In frequency domain, the current and previous dynamic displacement in X and Y directions can be expressed as:

$$\begin{Bmatrix} x(\omega) \\ y(\omega) \end{Bmatrix} = \begin{bmatrix} \Phi_{xx} & \Phi_{xy} \\ \Phi_{yx} & \Phi_{yy} \end{bmatrix} \begin{Bmatrix} F_x(\omega) \\ F_y(\omega) \end{Bmatrix}, \quad (2.5.2.23)$$

$$\begin{Bmatrix} x_0(\omega) \\ y_0(\omega) \end{Bmatrix} = (1 - e^{-i\omega T} \begin{Bmatrix} F_x(\omega) \\ F_y(\omega) \end{Bmatrix}, \quad (2.5.2.24)$$

$$\Delta(\omega) = \begin{Bmatrix} x(\omega) - x_0(\omega) \\ y(\omega) - y_0(\omega) \end{Bmatrix} = (1 - e^{-i\omega T}) \begin{bmatrix} \Phi_{xx} & \Phi_{xy} \\ \Phi_{yx} & \Phi_{yy} \end{bmatrix} \begin{Bmatrix} F_x(\omega) \\ F_y(\omega) \end{Bmatrix}. \quad (2.5.2.25)$$

The force function in frequency domain can be obtained by the substitution of Equation (2.5.2.18) and (2.5.2.25):

$$\begin{Bmatrix} F_x(\omega) \\ F_y(\omega) \end{Bmatrix} = \frac{N}{4\pi} K_{tc} a (1 - e^{-i\omega T}) B \begin{bmatrix} \Phi_{xx} & \Phi_{xy} \\ \Phi_{yx} & \Phi_{yy} \end{bmatrix} \begin{Bmatrix} F_x(\omega) \\ F_y(\omega) \end{Bmatrix}. \quad (2.5.2.26)$$

The force function can be rearranged and the problem becomes an eigenvalue problem:

$$\left[I - \frac{N}{4\pi} K_{tc} a\left(1 - e^{-i\omega T}\right) B\Phi(\omega)\right] F(\omega) = 0, \tag{2.5.2.27}$$

$$[I + \lambda\Phi_0(\omega)]F(\omega) = 0, \tag{2.5.2.28}$$

where $\Phi_0(\omega)$ is the oriented FRF (frequency response function) of the system which is the product of the B matrix and the FRF matrix $\Phi(\omega)$. λ is a complex number which is equal to:

$$\lambda = \lambda_R + i\lambda_I = -\frac{N}{4\pi} K_{tc} a\left(1 - e^{-i\omega T}\right). \tag{2.5.2.29}$$

The eigenvalue of Equation (2.5.2.28) can be solved for a given chatter frequency ω_c which is usually closed to a natural frequency of the system, cutting coefficients, radial immersion and the FRF of the structure. If the FRF are obtained in two orthogonal directions X and Y (i.e., $\Phi_{xy} = \Phi_{yx} = 0$), Then λ becomes roots of a quadratic function:

$$a_0\lambda^2 + a_1\lambda + 1 = 0, \tag{2.5.2.30}$$

where

$$a_0 = \Phi_{xx}(i\omega_c)\Phi_{yy}(i\omega_c)(b_{xx}b_{yy} - b_{xy}b_{yx}), \tag{2.5.2.31}$$

$$a_1 = b_{xx}\Phi_{xx}(i\omega_c) + b_{yy}\Phi_{yy}(i\omega_c). \tag{2.5.2.32}$$

By substituting the solution of λ into Equation (2.5.2.29), the axial depth of cut a can be obtained:

$$a = -\frac{2\pi}{NK_{tc}}\left[\frac{\lambda_R(1-\cos(\omega_c T)) + \lambda_I \sin(\omega_c T)}{1-\cos(\omega_c T)} + i\,\frac{\lambda_I(1-\cos(\omega_c T)) - \lambda_R \sin(\omega_c T)}{1-\cos(\omega_c T)}\right], \tag{2.5.2.33}$$

The depth of cut value should be positive and real. As a result, the imaginary part of Equation (2.5.2.33) should be zero:

$$\lambda_I(1-\cos(\omega_c T)) - \lambda_R \sin(\omega_c T) = 0, \tag{2.5.2.34}$$

$$K = \frac{\lambda_I}{\lambda_R} = \frac{\sin(\omega_c T)}{1-\cos(\omega_c T)}. \tag{2.5.2.35}$$

Substituting Equation (2.5.2.35) into the real part of Equation (2.5.2.33):

$$a = \frac{-2\pi\lambda_R}{NK_{tc}}(1+K^2). \tag{2.5.2.36}$$

Since λ has two solutions for a given chatter frequency, there would be two depth of cut limits. The positive minimum value of the depth of cut should be chosen.

Equation (2.5.2.35) can be rearranged as:

$$K = \tan\psi = \frac{\cos(\omega_c T/2)}{\sin(\omega_c T/2)} = \tan(\frac{\pi}{2} - \frac{\omega_c T}{2}), \tag{2.5.2.37}$$

$$\psi = \tan^{-1} K = \tan^{-1}(\frac{\lambda_I}{\lambda_R}). \tag{2.5.2.38}$$

ψ is the phase shift of the eigenvalue.

$$\omega_c T = \pi - 2\psi + 2\pi k = \varepsilon + 2\pi k. \tag{2.5.2.39}$$

ε is the phase shift between the two succeeding waves. The term $2\pi k$ represents full-vibration waves with k being an integer number ($k = 0,1,2 \ldots$). The tooth pass period T can be solved as:

$$T = \frac{\varepsilon+2\pi k}{\omega_c}. \tag{2.5.2.40}$$

The spindle speed in terms of T is:

$$n = \frac{60}{NT}. \tag{2.5.2.41}$$

In summary of the zero order analytical model for milling chatter stability, if the cutting force coefficients ($K_{tc},\ K_{rc}$) and the FRFs of the system in X and Y directions are known, by scanning the around the natural frequency of each mode of the system and solving for the eigenvalues, the positive minimum depth of cut limits can be calculated, and, as a result, the corresponding spindle speeds can be obtained.

There are several methods to obtain the FRF of the system. The finite element methods [104] relies on the estimation of the dynamic stiffness and damping of the system to obtain accurate results. The dynamic operational methods [105] [106] measure the vibration behaviour of the system under operating conditions to take into account the effect of tool motion on system vibration. The experimental methods [107]instead excite the static system and measure the system response.

The experimental tap testing method is widely used in practice. The excitation of the cutting tool is usually done by either an impact hammer or a shaker (input) at the tool tip in X and Y directions with an accelerometer attached on the opposite side of the tool tip to measure the response of the system (output). After the FRFs are obtained, processing software such as CutPro® and LMS Test.Lab® can be used to perform modal analysis in order to identify modal parameters such as natural frequencies, damping ratios, stiffness, and mode shapes.

In the context of this thesis, cutting force coefficients will be obtained by testing tests on AM artifacts. Modal analysis will be conducted on the tool-workpiece system. With the cutting force coefficients and vibration parameters of the system, chatter stability analysis will be performed in order to determine chatter free spindle speed and depth of cut which ensure dimensional accuracy and productivity.

2.6 Proposed AM and SM Process Workflow

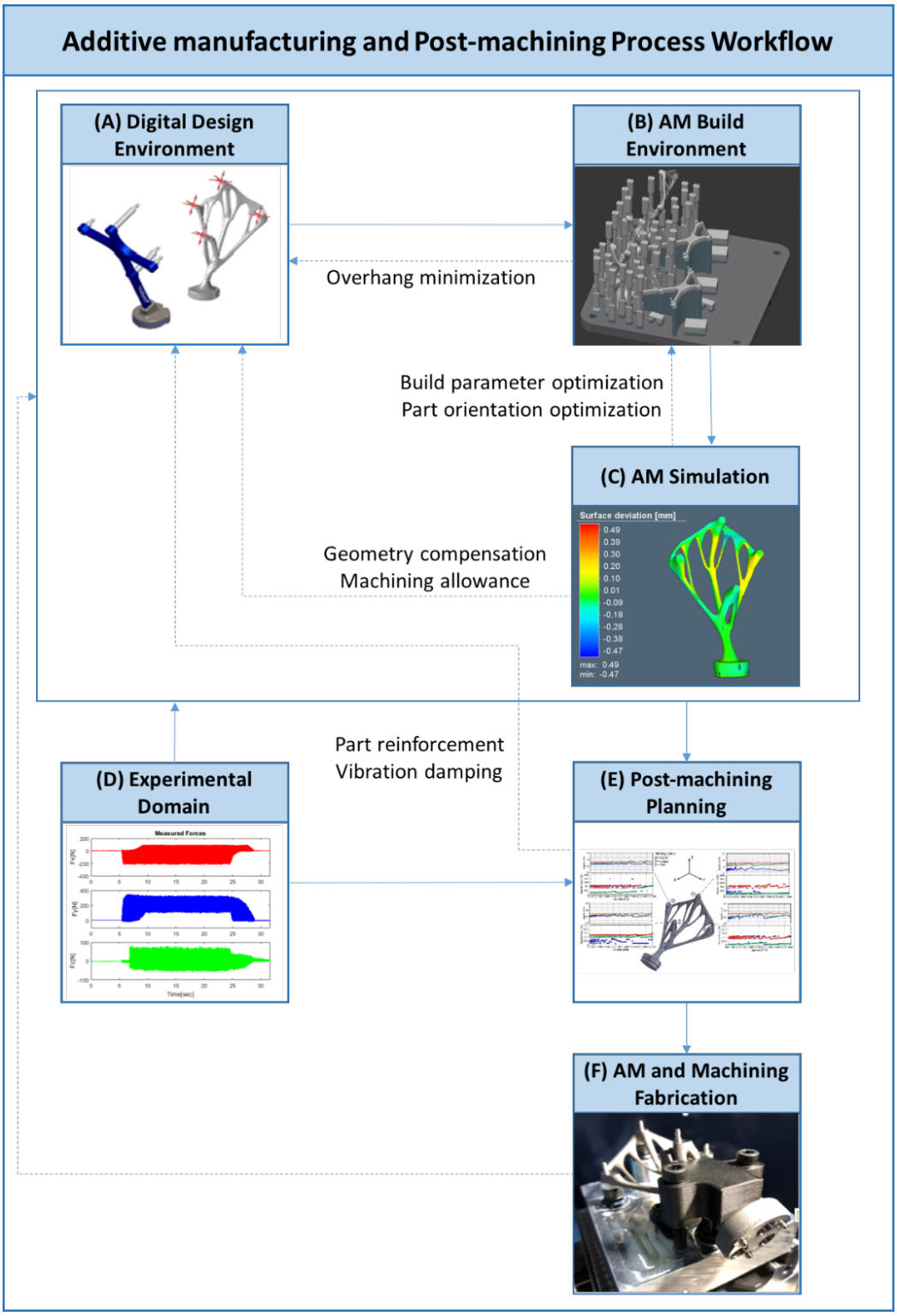

Figure 36: AM and SM process work flow.

In this thesis, the proposed strategy for the integration of AM and CNC post-machining has six modules (Figure 36): (A) digital design, (B) AM build design, (C) AM process simulation, (D) experimental domain, (E) post-machining planning, and (F) AM and SM fabrication environment. The process of manufacturing a successful finished part flows through the six modules and some of the modules may be revisited during iteration steps, where we try to generate the optimized digital build and machining strategy for the final printing and machining steps.

In the CAD design environment (Figure 36 A), with a more detailed description of this step is offered in Appendix A), an initial part design is first created and optimized. The optimization path for this thesis included assembly consolidation and structural topology optimization. Next, all critical features that require surface finishing as well as their corresponding tolerances are identified. In order to mount the part rigidly on the CNC machine in the machining step, clamping fixtures may be added to the design in a way that ensures accessibility of the cutter to all critical features, while minimizing the impact on the AM process. Also, internal connections and bridges or external encapsulation fixtures may be designed in order to improve the stiffness of the part and therefore avoid chatter and fracture of the part under cutting forces. Once the part design is ready through multiple iterations steps, it is then sent to the build design environment.

In the build design module (Figure 36 B), the optimized printing orientation is obtained so that only minimal support structures will be required. The CAD design environment (Figure 36 A) may be revisited if further reduction of support structures is desired by modifying the part or fixtures. Support structures are designed for down-facing surfaces to allow for easy removal, reducing waste materials and distortion of the printed part. Process parameters such as laser power, laser speed, layer thickness, scanning patterns will be set up in this step as well.

In the AM process simulation environment (Figure 36 C), work focuses on predicting the distortion of the printed part from the ideal CAD model by a thermomechanical FEA model, typically based on the build orientation and parameters selected in the build design module (Figure 36 B). Geometric compensation is made to the CAD design (re-iterating in the CAD design environment, Figure 36 A) according to the simulated distortion results. Machining allowance may also be required based on the results of the simulations. Redesigning the support structures or tuning the process parameters in the build environment may be helpful in reducing distortion. Upon completing the iterations through CAD design optimization (Figure 36 A), build design setup (Figure 35 B), and AM process simulation (Figure 36 C), an AM optimized digital build with some fixation features and machining allowance will be ready.

In order to gain understanding of how the part or cutting tool will behave in the CNC machining process, in the physical/experimental domain (Figure 36 D), cutting force coefficients and vibration modes of the workpiece-cutter-machine assembly need to be identified. Investigations need to be carried out to examine how the cutting force coefficients may be affected by AM scanning strategies, AM process parameters, microstructures, etc. By identifying the vibration modes and structural parameters the part, tooling, and machine, chatter may be avoided during the post-machining process.

With understanding of the CNC machining process, the digital build is sent to the machining simulation environment (Figure 36 E). Cutting forces are simulated by the identified force coefficients, machining conditions, and tool geometry. Optimized tool paths can be obtained by avoiding chatter while maximizing productivity through careful selection of spindle speed, depth of cut, and feedrate. The above analysis can be done using software such as CutPro® and MachPro™. FEA simulations may be conducted for part distortion under cutting forces to predict

if the machined part quality is going to be acceptable. If FEA results show significant deformation, the following options may help with minimizing deformation: adjusting tool paths or feedrate values, modifying any internal connections or external encapsulations in the CAD model to increase part stiffness. The part and fixture can be updated to avoid chatter and to withstand the expected machining forces as well, thus potentially re-iterating back to the CAD design environment (Figure 36 A), build design setup (Figure 36 B), and AM process simulation (Figure 36 C).

Once all requirements are satisfied, typically after a few iterations, the part can be additively manufactured and then heat treated to release some of the AM induced residual stress and reduce deformation, after removal from the substrate (Figure 36 F). This may introduce further part dimensional changes. In this work, the heat treatment was captured in the AM process simulation (Figure 36 C), however quantifying the direct impact of such was beyond the scope of this study. The part is then mounted on the CNC machine rigidly. 3D scan or probing is performed to locate the printed part and align it with the CAD model. Once the finishing is complete, the part is validated again via CMM or a 3D scan.

The surgical navigation tracker design presents a challenge and opportunity to study the AM topology optimization design potential and secondary processing of complex structures via machining. The process of manufacturing a successful finishing part flows through the six modules of the workflow iteratively. Chapter 3 provides general experiment datasets such as powder size, hardness, porosity distribution, and surface roughness of the printed Ti64 parts which was done in Module D - experimental domain. Chapter 4 focus of the AM process which includes part design using topology optimization (Module A), AM build setup (Module B) and geometric distortion simulation (Module C). Chapter focus on the post-machining process which includes cutting tests,

tap testing (Module D) and chatter stability analysis for identifying chatter free depth of cut and spindle speed (Module E). Lastly, Chapter 6 describes the fabrication of the tracker deploying AM and post-machining (Module F).

Chapter 3

General Experimental Datasets

3.1 Materials and Methods

3.1.1 Powder materials

The LPBF fabrication of the trackers and the related artefacts is conducted by using Ti-6Al-4V ELI-0406 (Ti64), a Titanium alloy powder, provided by Renishaw®, on the AM 400 machine. According to the data sheet, the Ti64 alloy comprises titanium mass fraction up to 90% with up to 6.75% aluminum, 4.5% vanadium and other minor elements. The powder was characterized for size distribution using a particle size analyzer (Retsch Camsizer X2, Newtown, PA).

3.1.2 Artifact designs

Three tensile test artefacts (labeled as Z1, Z2, and Z3) with dimensions as shown in Figure 37 as well as three meander (labeled as M1, M2, and M3) and three stripe (labeled as S1, S2, S3) machining blocks with dimensions as shown in Figure 38 were printed. Meander and stripe are two of the scan strategies which will be explained in section 4.1.2. The tensile samples were printed vertically and the machining blocks were printed flat.

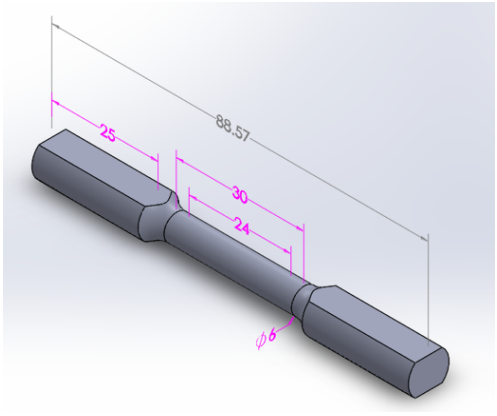

Figure 37: Tensile samples.

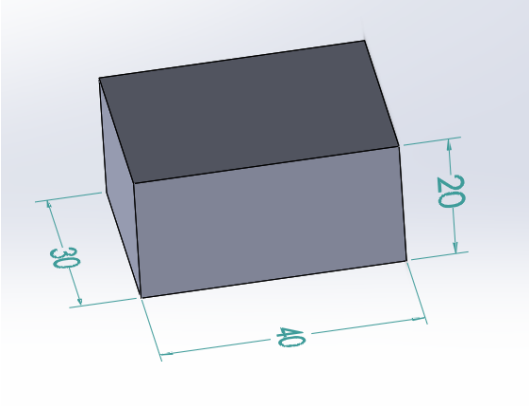

Figure 38: Machining blocks.

3.1.3 Surface roughness

The surface roughness of the as-printed tensile and machining artifacts was characterized via a 3D laser scanning microscope (Keyence VK-X250, Osaka, Japan) at x20 magnification. Image processing and measurements were done by using the microscope scan processing software (Keyence VK-H1XME, Osaka, Japan). The roughness was measured at three locations along each side (A, B, C, and D) of the gauge portion (along the build direction) of the tensile samples and at three locations at the top surface (perpendicular to the build direction) of meander and stripe blocks, as shown on Figure 39. The measurements were taken from approximately the same location on all samples for the tensile and machining artifacts. The scanning area of each surface scan is about 1940 x 520 μm. Surface correction for side surface curvature was employed when scanning the tensile samples.

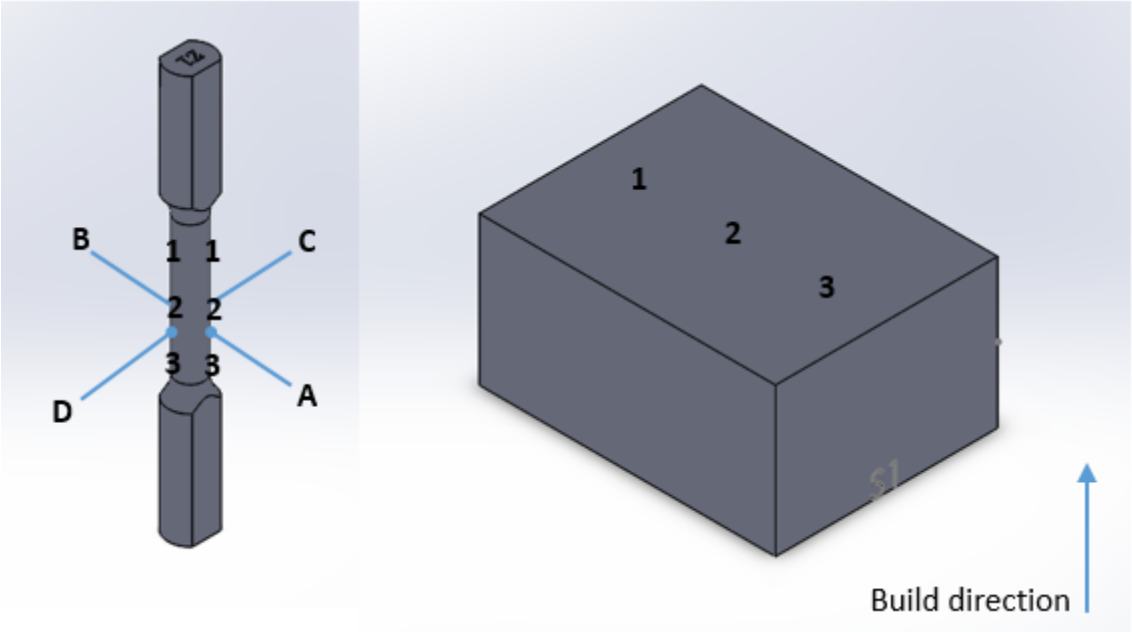

Figure 39: Surface roughness measurement locations.

3.1.4 Hardness

A Rockwell hardness tester was used to measure the hardness of the printed Ti64 blocks with C scale. Six indentations were made across the machined surface of the meander and stripe blocks by a diamond penetrator ("BRALE") under a 150 kg load (Figure 40). Based on the depth of penetration, a hardness value expressed in HRC was obtained for each indentation. An average hardness value was calculated using the six measurements for each artifact. The result was compared to the hardness value of conventional Ti64 (Grade 5). For this study, only hardness of the machined top surface was measured, potential hardness variation on surfaces normal and parallel to the build direction due to anisotropic mechanical properties of AM parts was not investigated.

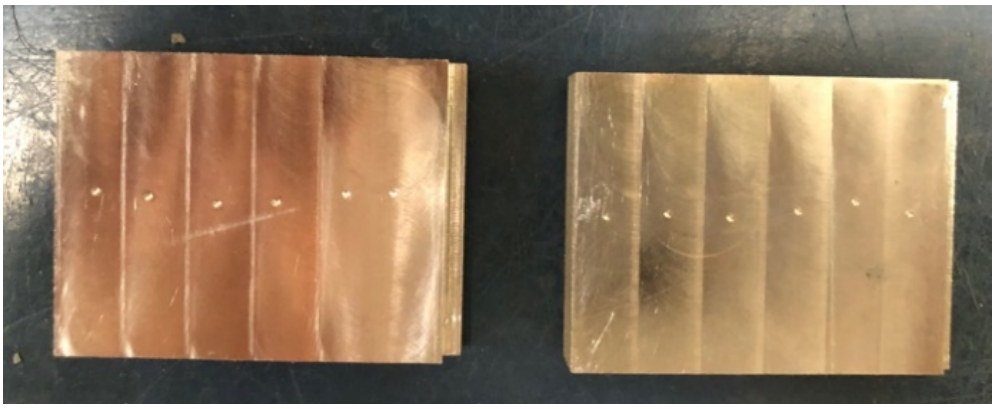

Figure 40: Hardness test indentations.

3.1.5 Computed Tomography (CT)

In order to gain an insight of the pore size and location within the printed tensile samples, CT scanning was performed by a Zeiss Xradia 520 Verse X-ray microscope, with the following Scout-and-Scan software settings applied for all sample analysis.

Table 1: Scout-and-Scan settings for CT imaging.

Parameter	Unit	Value
Source power	[W]	8
X-ray energy	[kV]	140
Filter	-	Air
X-ray optic	-	0.4Xlens
Source position	[mm]	15.002
Detector position	[mm]	87.997
Exposure time	[s]	0.5
Binning level	-	2
Voxel size	[μm]	10

After scanning, images were automatically reconstructed into 16-bit greyscale TIF for further processing (thresholding, binarizing, etc.) via specific image processing algorithms (MATLab) in order to quantify details regarding the pore size, location, orientation and shape within the sample volume. 3D pore distribution was projected to the center plane to obtain a 2D view of the pore distribution.

3.2 Results

3.2.1 Powder materials

The powder size distribution was determined as shown in Figure 41 which follows a gaussian distribution with the mean equal to 33.12 μm and the standard deviation equal to 9.07 μm. The size of 10% of the powder particle fails under 20.90 μm (D_{10}), 50% fails under 33.25 μm (D_{50}), and 90% fails under 44.8 μm (D_{90}). The layer thickness (build bed piston displacement) in this study was selected as the default 30 μm, as the steady state actual layer thickness is much higher due to densification of the previously solidified layer(s) in steady state. This is a typical layer thickness for this type of powder size distribution.

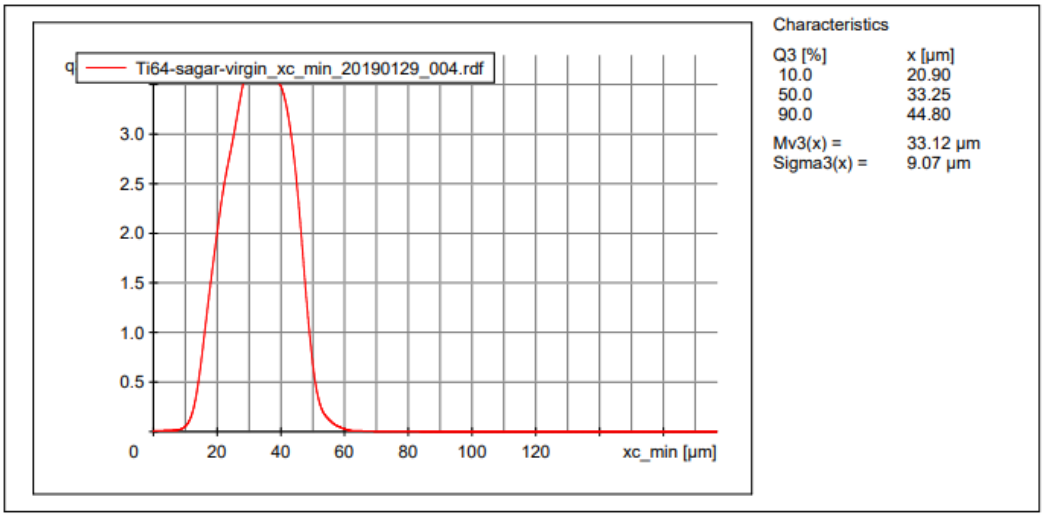

Figure 41: Powder size distribution of Ti6Al4V ELI-0406.

3.2.2 Surface roughness

The surface roughness measurements were summarized in Table 2 and Table 3. The surface roughness metric "Sa" stands for the "arithmetical mean height". "Sdr" is the standard deviation. In general, top surfaces of the machining block are smoother than the side surfaces of the tensile samples. This suggest that build orientation of the parts have effect on the surface roughness. Since the printed part is buried in powder during the LPBF process, partially melted powder tend to adhere to the side of the solidified part, which creates rougher surface. The results indicate that the top surface of the meander block is rougher than that of the stripe block, which implies that scan pattern may influence surface roughness, with implication for machining strategies. The Side A is generally the smoothest and Side D is the roughest for all samples.

Table 2: Tensile samples surface roughness measurements.

Tensile sample	Z1		Z2		Z3	
Scan location	Sa (μm)	Sdr	Sa (μm)	Sdr	Sa (μm)	Sdr
A_1	8.54	0.4451	10.45	0.5349	10.07	0.7856
A_2	9.16	0.4875	10.66	0.4773	13.64	0.8100
A_3	10.30	0.4558	9.26	0.5609	10.80	0.6031
B_1	16.55	0.8473	14.21	0.5102	10.62	0.5037
B_2	18.75	1.022	12.57	0.5791	15.87	0.7147
B_3	14.21	0.7039	11.31	0.5390	10.76	0.5962
C_1	13.08	0.6583	11.63	0.6902	12.08	0.6016
C_2	11.61	0.4565	10.18	0.5491	15.62	0.6984
C_3	10.03	0.5574	7.62	0.5850	10.30	0.5607
D_1	19.20	1.305	19.66	1.178	18.39	1.282
D_2	19.32	1.614	18.14	1.273	17.99	1.306
D_3	18.05	0.9426	17.34	1.162	17.75	1.290

Table 3: Machining block surface roughness measurements

Machining block	Meander		Stripe	
Scan Location	Sa (μm)	Sdr	Sa (μm)	Sdr
1	7.09	0.1312	5.18	0.1101
2	7.06	0.1778	6.52	0.1493
3	9.62	0.1934	6.48	0.1170

Side surface roughness is affected by process parameters, chamber gas flow, and part location on the build plate. In theory, surface roughness increases along the movement of the re-coater as fine powder tend to settle down on the build plate first leaving the coarse powder at the end. Surfaces facing the gas flow may be smoother than opposing side surfaces due to particle ejections and condensates following the gas flow trajectory, thus contributing to regions of higher surface roughness. The experimental result follows a similar trend (Figure 42).

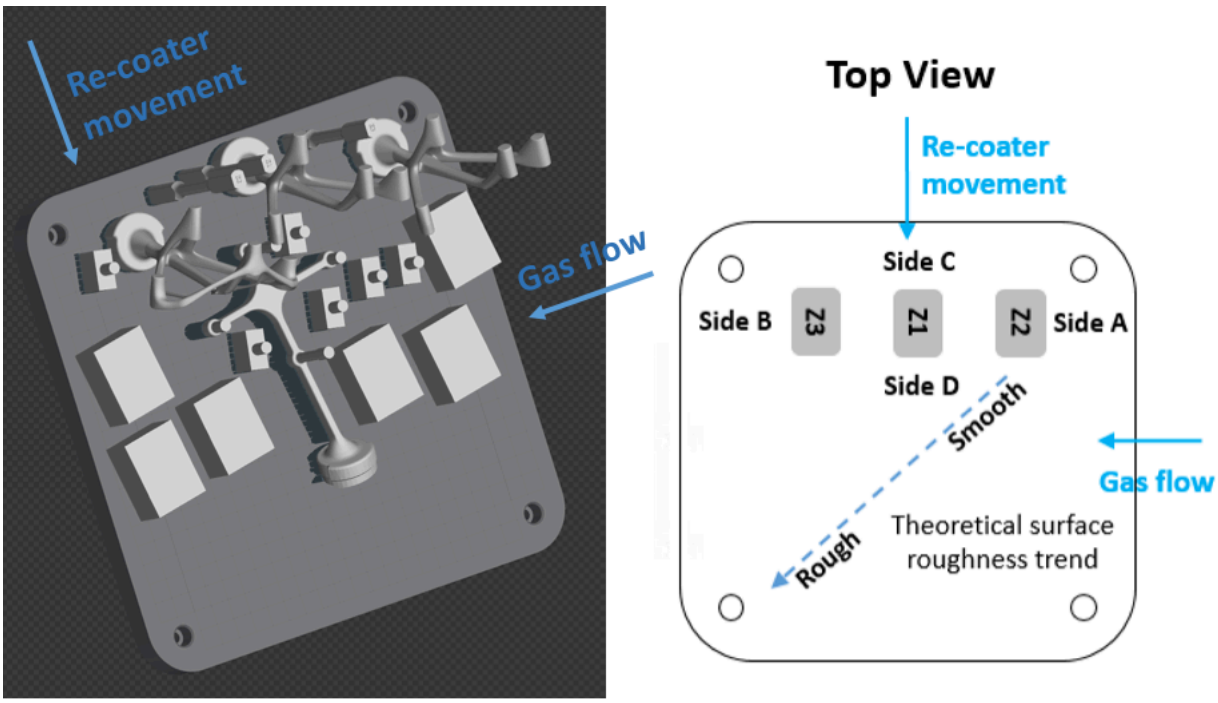

Figure 42: Tensile sample location and orientation in build environment.

3.2.3 Hardness

Hardness results (Table 4) show that the hardness of the printed artifacts is consistent. On average, the meander artifact is about 2.7 HRC harder than the stripe one. The hardness of the printed artifacts is close to that of the conventional Ti-6Al-4V (Grade 5) which is about 36 HRC [108]. Hardness of the machining blocks may have effect on the cutting forces during machining.

Table 4: Hardness test results (unit: HRC).

Location / Artifact	1	2	3	4	5	6	Average	Standard Deviation
Meander	39	39.5	39	39	39	38	38.9	0.449
Stripe	37	36	35	36	36	37	36.2	0.688

3.2.4 Computed Tomography

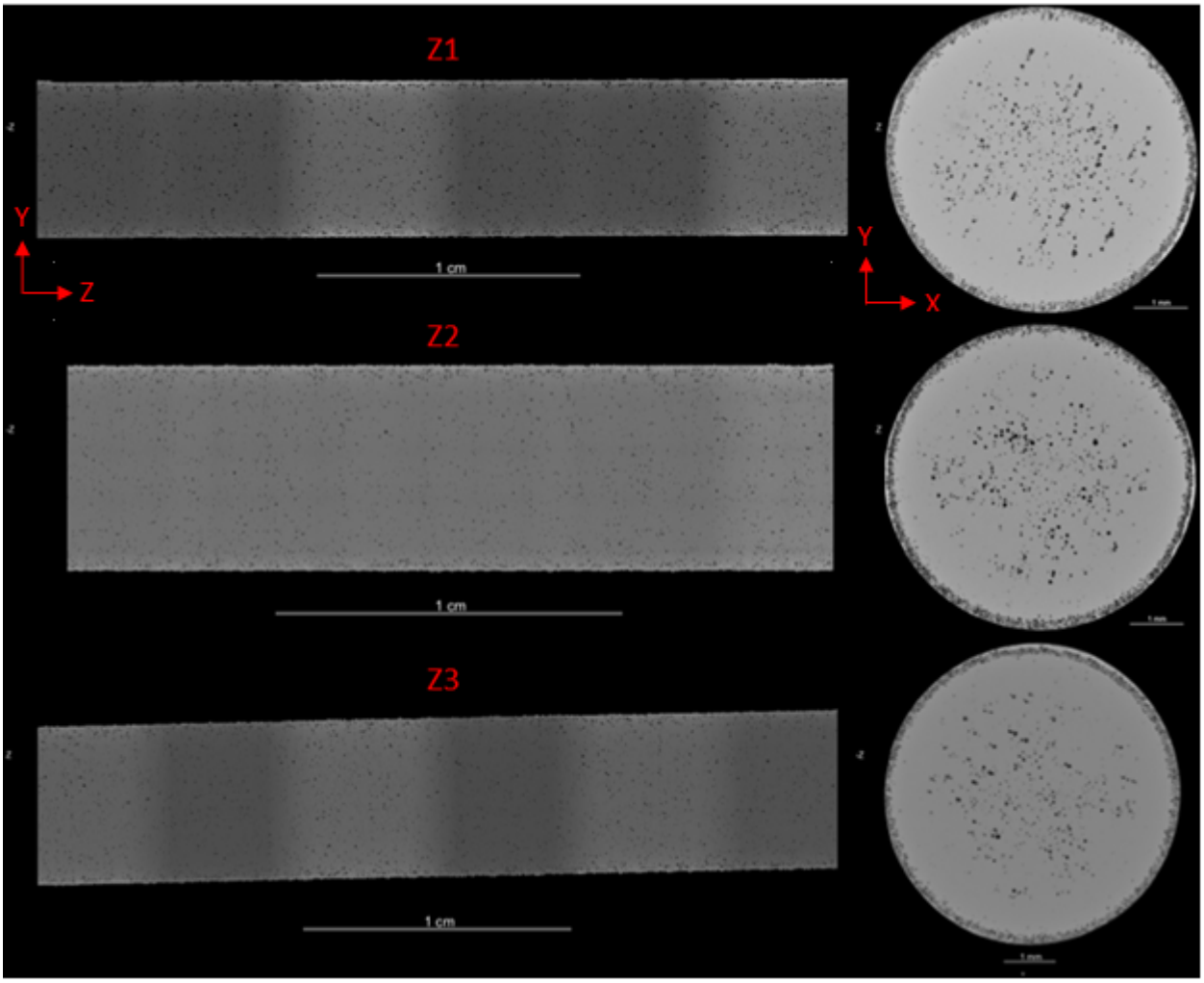

Figure 43: Porosity projections of tensile samples.

The porosity projections of the gauge portion of the tensile samples (Z1, Z2, and Z3) on the Y-Z and X-Y planes are shown in Figure 43. It can be seen that pores mostly concentrated at the surface and the center of the cylinder. Porosity distribution along the Z axis was consistent. Results also show that, in general, all tensile samples achieve >99.94% solid fraction. Studies have shown that porosity is highly dependent on the energy input, which is determined by print parameters such as laser power, laser speed, scan strategies and layer thickness [47] [109]. Lack of energy (un-melted powder) or excessive energy (material ejection from keyhole mechanism)

can all lead to porosity. In order to improve mechanical properties of printed parts, optimum print parameters need to be found. Surface porosity may be eliminated by post-machining to improve part fatigue life. The focus of this study was not on process parameter optimization, and the density obtained was considered acceptable for the purpose of this work.

Chapter 4

Design Considerations and Build Considerations for Additive Manufacturing

4.1 Methodology

4.1.1 Topology optimization and build optimization

SolidThinking Inspire (hereafter referred to as Inspire), which implements the SIMP topology optimization algorithm, was used to generate design candidates. Before importing the part into Inspire, the part was divided into design and non-design spaces in Solidworks. After loading the part with subdivisions into Inspire, the design space and non-design space were defined, as shown in Figure 44. The material of both the design space and the non-design space were specified as Ti64. Topology optimization was performed on the design space, while the non-design space remained untouched. The four posts and the base of the tracker were defined as being outside the design space, since they will be either press-fitted with reflective spheres, or will be sitting on a kinematic mounting platform respectively and should adhere to pre-defined design topologies. There is no intention to modify any external parts or mounting faces interfacing with this tracker design. In this design, the relative position among the posts and the base of the tracker is desired to be fixed.

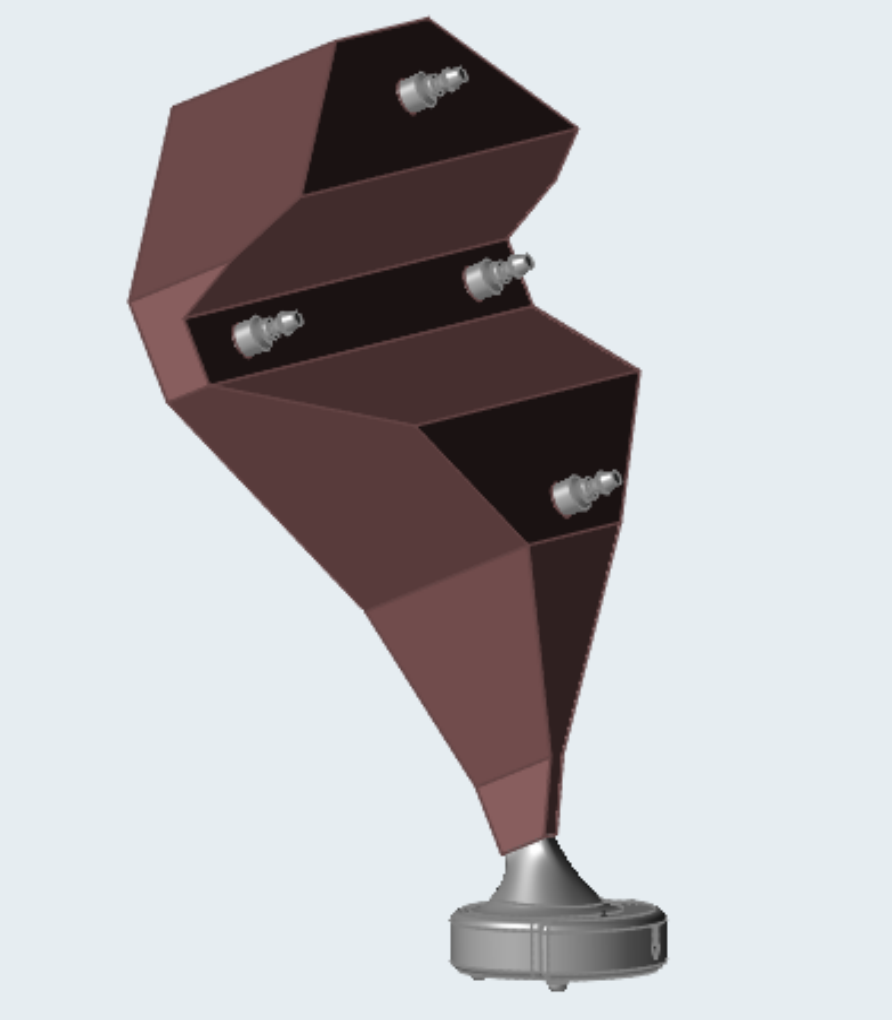

Figure 44: Design (in claret) and non-design spaces (in grey).

The design space was created with the consideration of functional criteria of the tracker. For example, it is desired that the tracker will not impinge on soft tissues of the patient; it should be graspable by an adult hand without touching the tips of the posts; all spheres attached to the posts should be visible to the camera; the centre of gravity should be as low as possible to avoid part toppling during use; and the overall height of the tracker should not exceed 150 mm. The functional design criteria is summarized in Table 5.

Table 5. Tracker design criteria.

Criterion No.	Functional design criteria description
1	The relative position among the posts and the base must be fixed
2	It is desired that the tracker will not impinge on soft tissues of the patient
3	It should be graspable by an adult hand without touching the tips of the posts
4	The tracker body should be matte
5	All spheres attached to the posts should be visible to the camera
6	The centre of gravity should be as low as possible to avoid toppling
7	The overall height of the tracker should not exceed 150 mm
8	External mating parts interfacing with this tracker should not be modified

The next step in topology optimization is to apply loads and constraints. Loads and supports can only be applied upon non-design space (design independent loads). In order to create a structure of which the posts and the base are rigidly connected with each other, different load cases are considered as shown in Figure 45. For comparison, the case where there are only forces (each of 30N) acting normal to the surfaces of the four posts (load case 1) was also run. The magnitude of the force acting on each post is 30 N. This force is approximately three times the maximum force that the product will be expected to see during operation based on user input. The direction of the forces changes in different load cases with the base of the tracker always fixed.

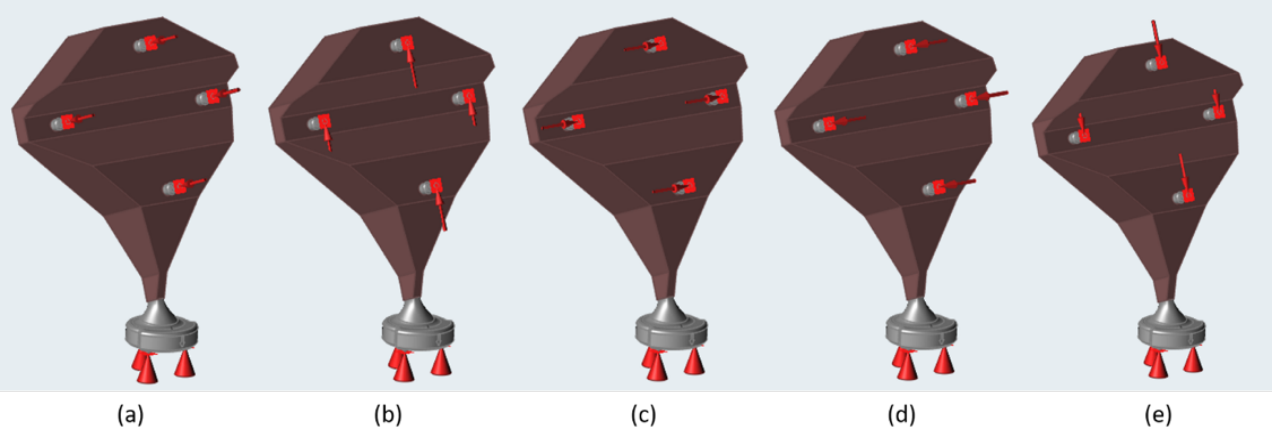

Figure 45: (a) Load case 1 with normal acting forces; (b) Load case 2 with upwards acting forces; (c) Load case 3 with rightwards acting forces; (d) Load case 4 with leftwards acting forces; (e) Load case 5 with downwards acting forces.

An overhang shape constraint of 45° relative to the build direction is applied (Figure 46) in order to obtain self-supporting designs. Topology optimization without the overhang shape constraint was also run for comparison.

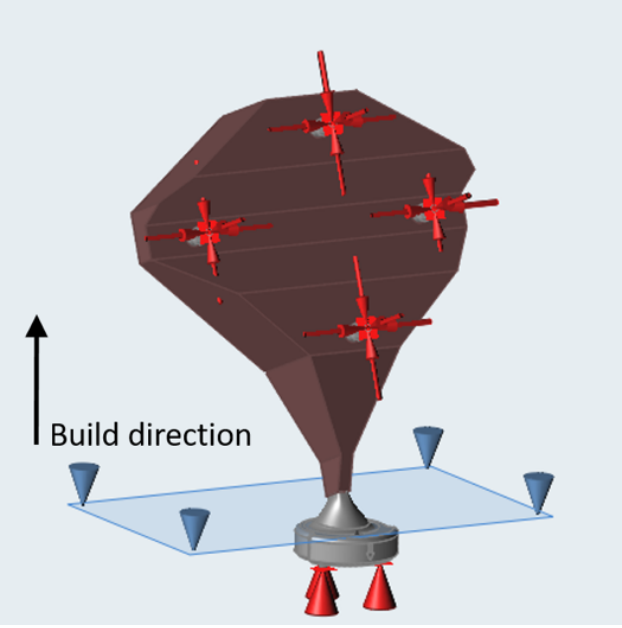

Figure 46: 45° overhang shape constraint.

The structure is then optimized by setting the objective as maximizing stiffness with mass targets of 5%, 10%, 15%, 20%, 25% and 30% of the original design space. The minimum thickness

(checker board filter radius) is chosen to be 3 mm. Gravity is ignored in all simulations. The compliance, safety factors and mass of the generated candidates were compared.

4.1.2 AM build environment and parameters

The QuantAM software (Renishaw) was used to visualize parts in the build environment and to perform pre-processing such as finding the optimum build orientation, determining overhangs and generating support structures, slicing the part based on specified layer thickness and defining print parameters such as scan pattern, laser power, layer thickness and etc. Figure 47 below illustrates an example of the visualization of parts laid out on a build plate in the build environment.

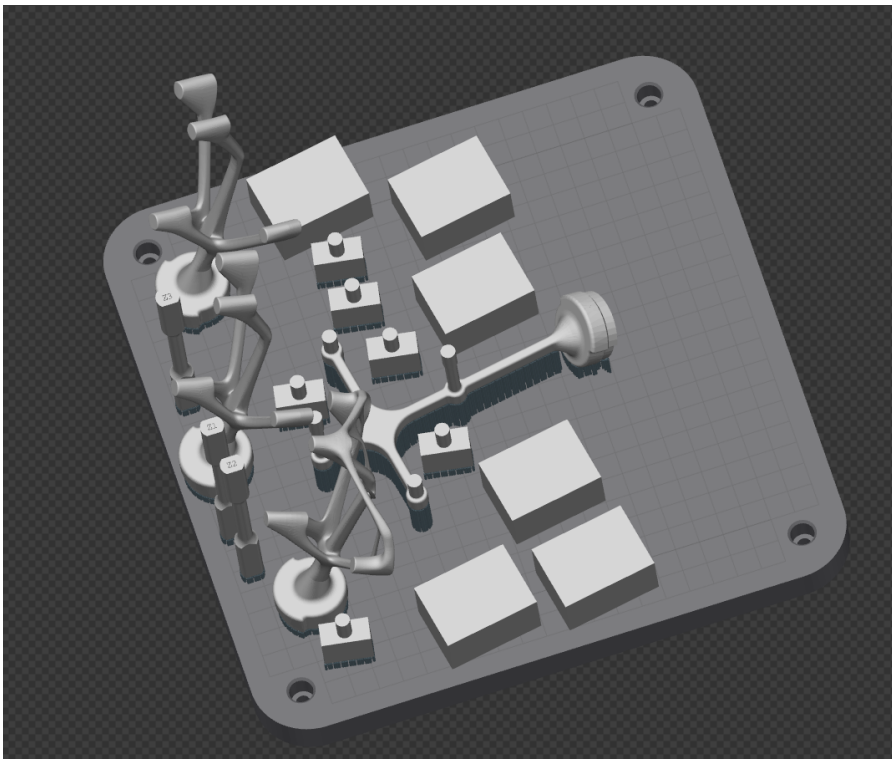

Figure 47: Build Setup in QuantAM.

All parts were printed using stripe pattern except that three of the machining blocks were printed using meander pattern. Figure 48 illustrates 4 typical scanning patterns which are meander,

stripe, chessboard, and total fill. This study focus was on examining different properties of meander and stripe parts. The actual tracker designs were printed using stripe scanning pattern. For meander pattern, the entire layer is swept by uniform hatch lines which are rotating 67° from on layer to another. For stripe pattern, each layer is divided in to sections according to the specified stripe size, and then each section is filled by hatch lines. Meander pattern is usually adopted when printing thin-wall structures while stripe pattern is more suitable for thicker parts for the purpose of minimizing residual stress.

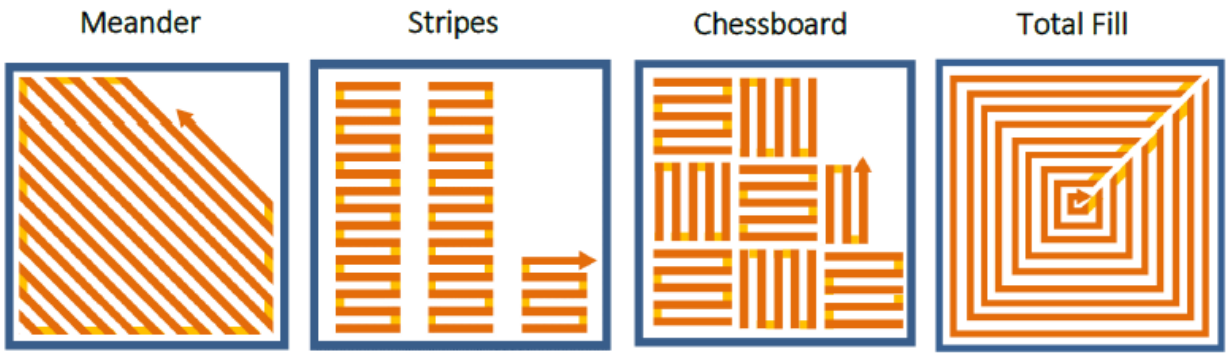

Figure 48: Scanning Patterns [110].

For this study, the stripe parts were printed using the QuantAM recipe "Ti6Al4V_200_1112_08_30µm_strips" and the meander parts were printed using the QuantAM recipe "Ti6l4V_200_1112_08_30µm_meander". The main process parameters of the two recipes were listed in Table 6 and Table 7 respectively. Renshaw's AM 400 machine utilizes a modulated laser which moves discretely from hatch point to hatch point. The laser is turned on for the specified exposure time at each hatch point and it is turned off while moving to the next hatch point. One layer of upskin was applied on up-facing surfaces and one layer of downskin was applied on down-facing surfaces. The core of the part was scanned using the volume parameters and two borders were applied at the periphery of each volume layer to improve

surface quality. Border distance is 0.06 mm for the meander recipe and 0.04 mm for the stripe one.

Table 6: QuantAM print parameters for Ti64 with stripe pattern and 30 m layer thickness.

Ti6Al4V_200_1112_08_30um_stripe(QuantAM)								
	Power (W)	Beam width (mm)	Exposure time (ms)	Hatch point distance (mm)	Hatch distance (mm)	Stripe Size (mm)	Stripe Offset (mm)	Layer thickness (mm)
Volume	200	0.075	50	55	0.105	5	0.01	0.03
Border	100	0.075	40	45	-	-	-	-
Upskin	175	0.075	75	50	0.065	-	-	0.03
Downskin	175	0.075	75	50	0.065	-	-	0.03

Table 7: QuantAM print parameters for Ti64 with meander pattern and 30 m layer thickness.

Ti6Al4V_200_1112_08_30um_meander(QuantAM)						
	Power (W)	Beam width (mm)	Exposure time (us)	Hatch point distance (mm)	Hatch distance (mm)	Layer thickness (mm)
Volume	200	0.075	50	75	0.065	0.03
Border	100	0.075	40	45	-	-
Upskin	175	0.075	50	75	0.065	0.03
Downskin	175	0.075	50	75	0.065	0.03

4.1.3 Simulation of the AM process

The thermomechanical model developed by Simufact Additive® for geometric distortion of LPBF parts was examined. The general LPBF simulation process was as shown in Figure 49.

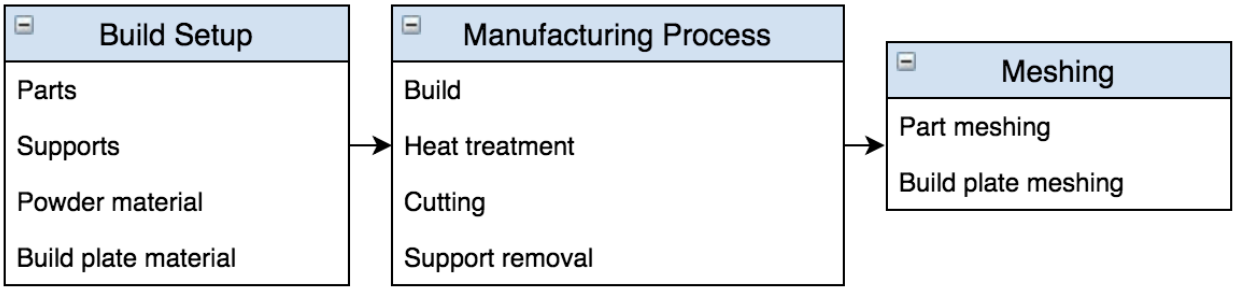

Figure 49: LPBF simulation process.

First, the stl files of the parts were imported and positioned on the build space. For this study, the trackers were placed at the lower left corner, the upper right corner, and the center of the build plate (Figure 50).

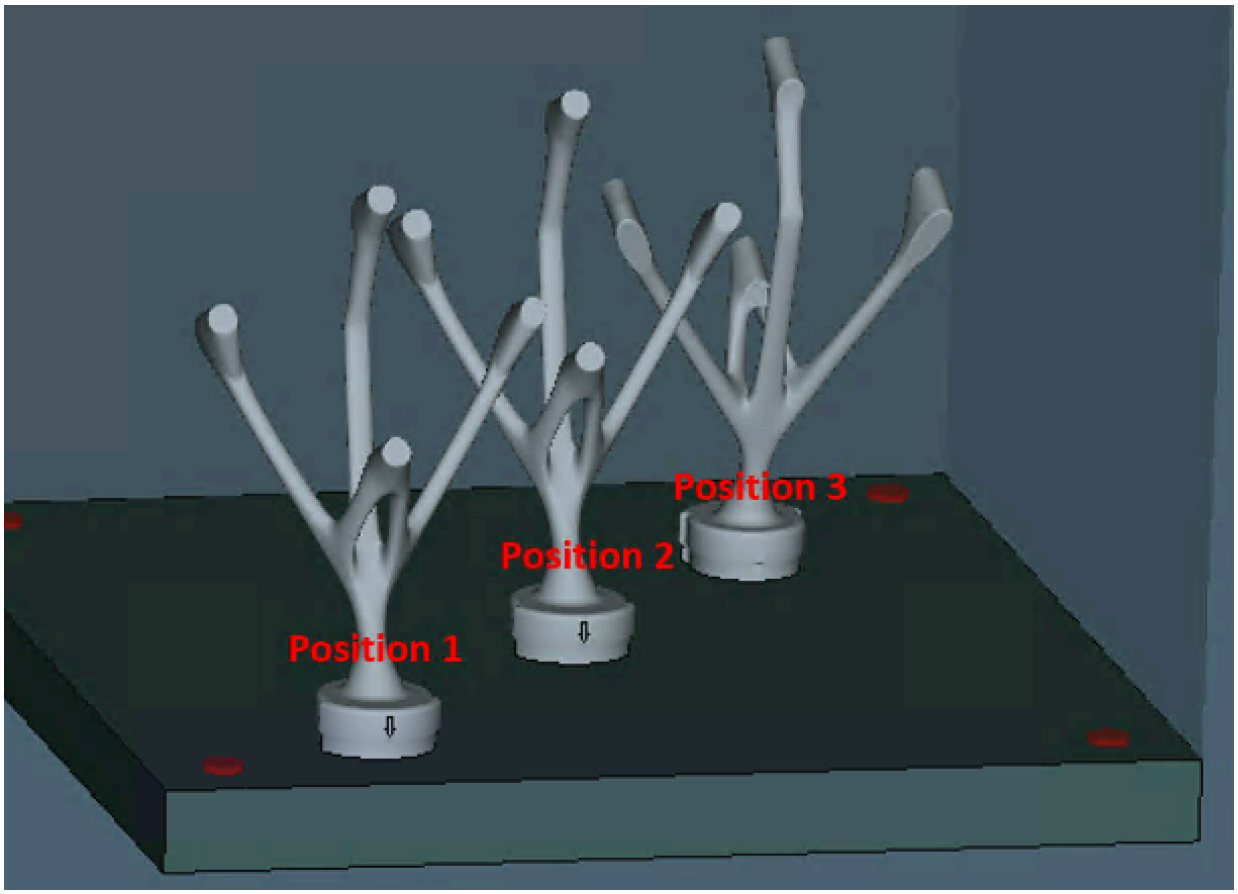

Figure 50: Geometry import and positioning.

A trial simulation was run and surface deviation of all parts were computed. As it is shown in Figure 50, no significant difference was observed in the surface deviation of parts located on

different locations. The software may not take into account the effect of nuisance factors such as powder distribution, gas flow, and re-coater motion on geometric deviation or their effect is small in this case. As a result, the actual simulation was run with the part placed only at the center of the build plate.

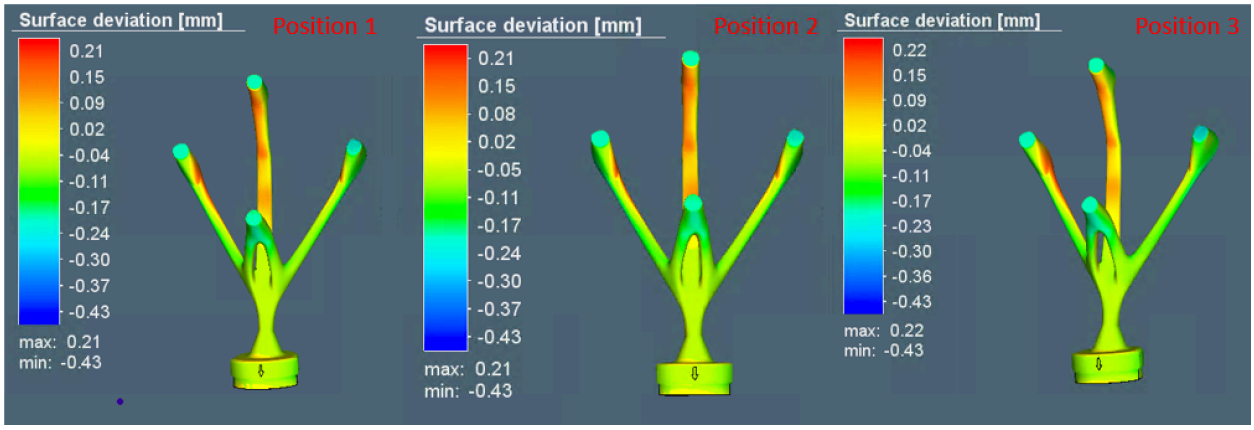

Figure 51: Surface deviation for parts placed on different locations.

For both the Cobra and ET design, no support structures were required as they are self-supported. The software will automatically detect overhangs with an angle greater than 45°with respect to the build direction and generate supports underneath. Ti64 properties loaded from the material library was applied to both the part and the build plate.

In the manufacturing process, the manufacturing plan was configured such that the part would go through building, heat treatment, cutting stages. The support removal stage was excluded in this case as no support structure was needed. Figure 52 and Figure 53 show the build parameters and scanning strategy which were set base on the actual parameters used (Table 6). The software assumes a continuous laser but AM 400 machine utilizes a pulsed laser. A conversion has been done to approximate the equivalent continuous power by the product of pulse laser power and exposure time over the sum of exposure time and travel time between hatch points.

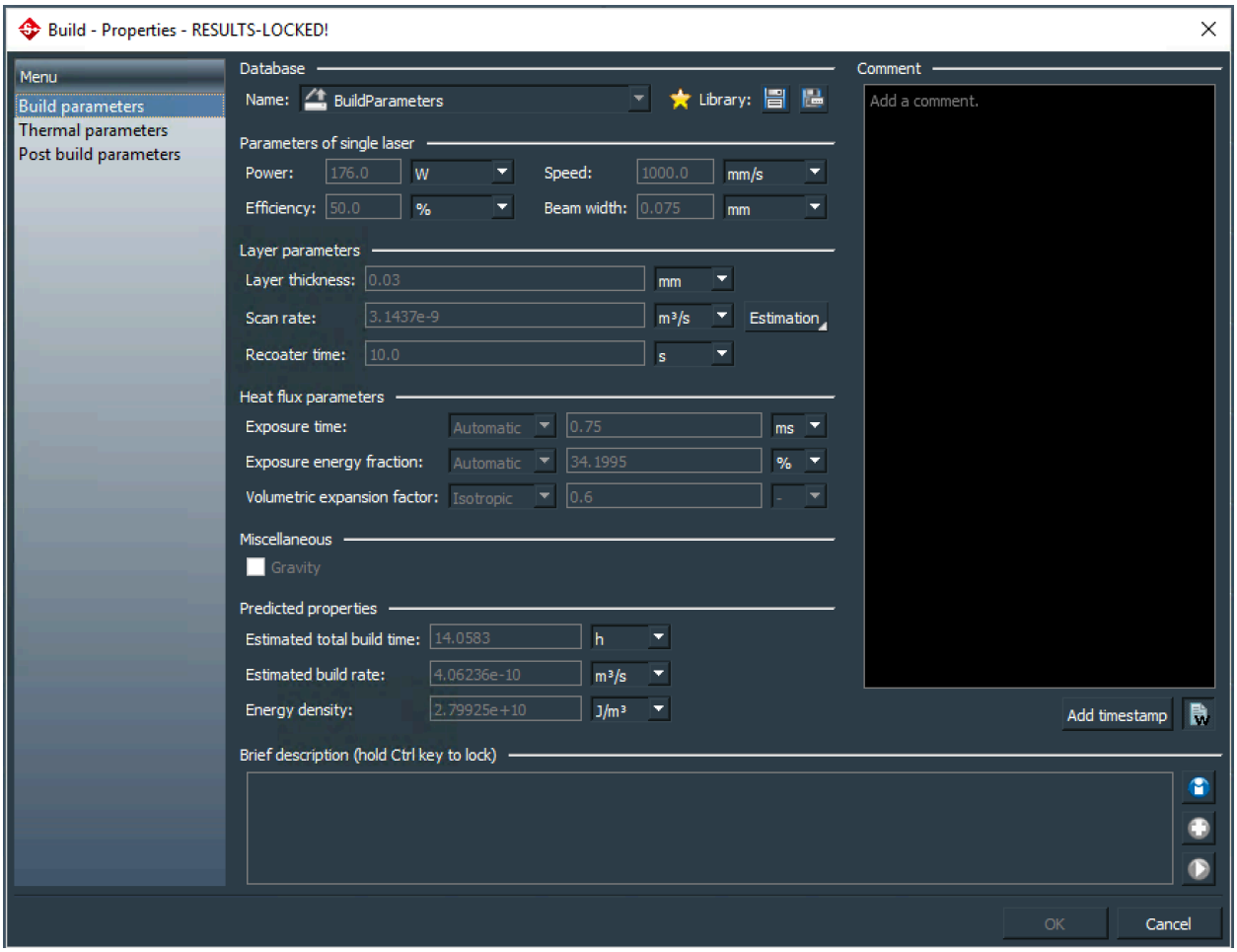

Figure 52: Build parameters.

Figure 53: Scanning strategy.

For post-processing the part was heat treated for the relief of residual stress. The temperature curve shown in Figure 54 mimics the actual heat treatment stage. After heat treatment the part

was cut from the build plate. The final part was best fitted with the initial CAD model to computer geometric deviation.

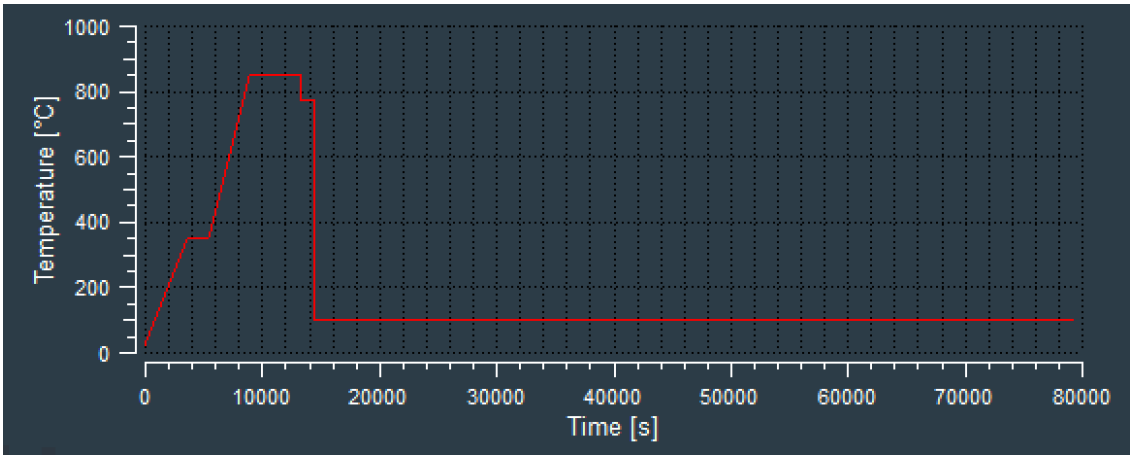

Figure 54: Heat treatment temperature curve.

A convergence check was performed to minimize discretization errors in the simulation. Mesh sizes of 1, 0.75, 0.6, and 0.5 mm were selected and the corresponding node numbers as well as the simulated maximum temperatures were listed on Table 8. A convergence plot was created by plotting the maximum temperatures against number of nodes (Figure 55). Results show that maximum temperatures converge at approximately 0.5 mm mesh size. Simulated distortion with 0.5 mm mesh size were compared with 3D scan results in Section 4.2.2. It took about 3 days for the simulation with 0.5 mm mesh size to complete on a 4 cores, 16 GB desktop. Due to time constraints, no further mesh refinement was performed.

Table 8: Mesh statistics and maximum temperatures.

Mesh size	Nodes	Max temperature	Simulation Time
1	45503	5651.37	2 hrs
0.75	82443	4710.24	5 hrs
0.6	139739	4524.68	2 days
0.5	222263	4792.17	3 days

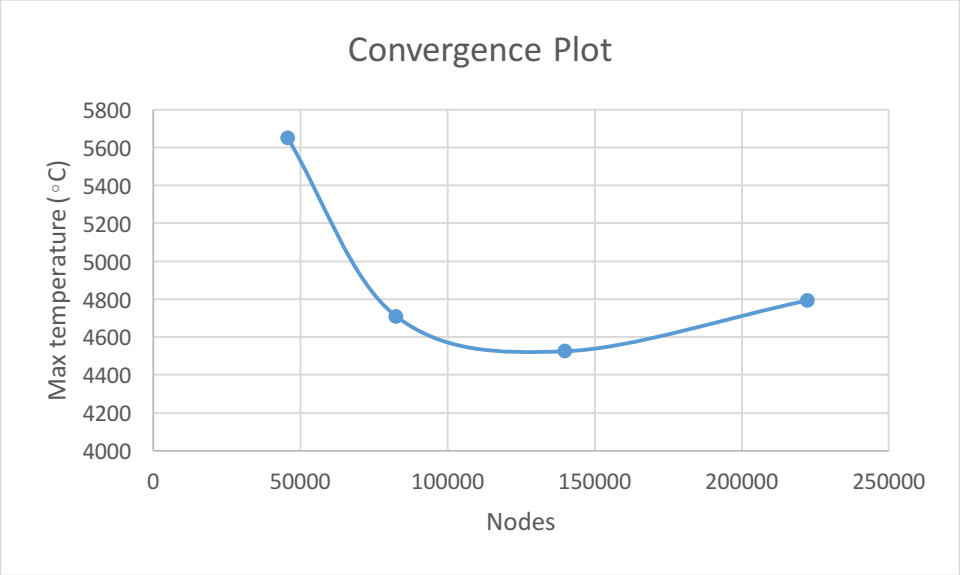

Figure 55: Maximum temperature vs. number of nodes.

4.1.4 Quantification of the AM design, simulation, and manufacturing via 3D structured light scanning

The AICON optical scan system was used to capture the 3D image of the printed design. The scanner was calibrated against a plate with makers at certain locations. The calibration yielded an accuracy of 2 µm. The part was fixed on a turn table at the focal point of the scanner cameras. Firstly, the turn table was automated to turn at every 36° so that a total of 10 images completed a 360° view of the part. The angle change between two sequential scans was selected to make sure there is enough overlapping area between the two scans so that the scanned images can be stitched automatically or, if not, manually. At each part orientation, the projection unit of the system projects a sequence of fringe patterns onto the part. The cameras capture the projected fringe pattern and create an image of the scanned area. The brightness of the projector was adjusted to avoid overexposure. To better capture the surface with probably varying quality, two exposure settings were used and the result is the average of the captured images. The system

allows for maximum four different exposure settings. Four shutters were taken at each turn and the average was computed to filter out noise. After the automated scanning, areas that had not been captured were scanned manually by adjusting the orientation of the part with respect to the camera and making sure area of interest was not hidden from the camera. The scanning process was repeated until all interested area was captured. A three-dimensional point cloud coordinates of the scanned object were calculated and can be exported as a STL file for processing. The inspector module of PolyWorks software (InnovMetric) was used to measure the geometric deviation of the printed part from the CAD model. The scanned object was best fitted with the CAD model at the base of the tracker and a color map showing the general deviation was obtained. Cross sections were taken at the four posts as well as at the vertical and horizontal planes of the base (Figure 56). Geometric deviations along the cross sections were obtained.

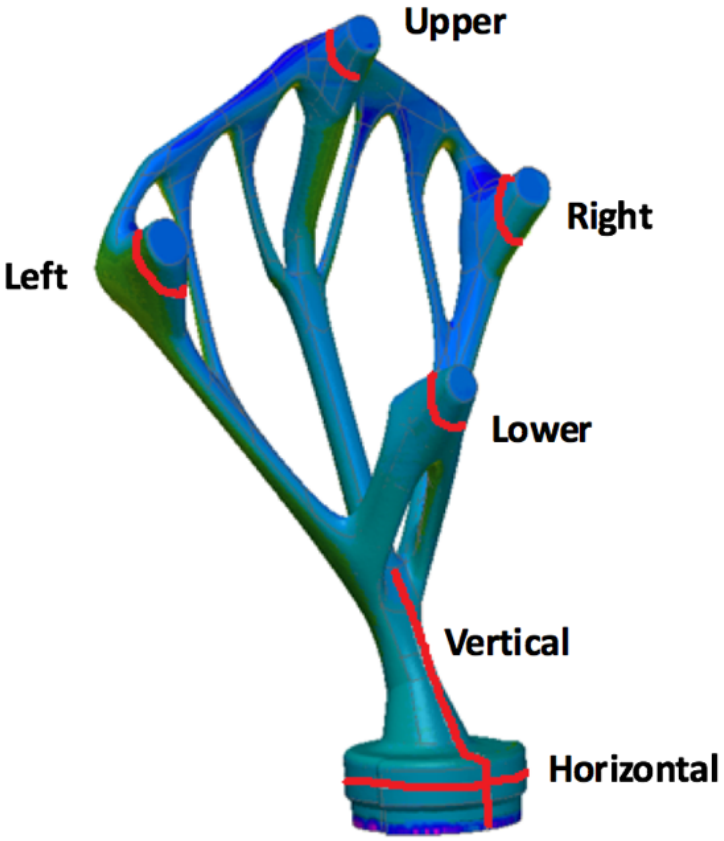

Figure 56: Cross sections where geometric deviations were measured.

4.2 Results

4.2.1 Topology optimization and build optimization

Figure 57 displays design candidates obtained by applying topology optimization settings as shown in Table 9.

Table 9: Topology optimization settings-Scenario 1.

Load direction	Load magnitude	Volume fraction	Overhang constraint
Multiple	30N	30%, 25%, 20%, 15%	45°

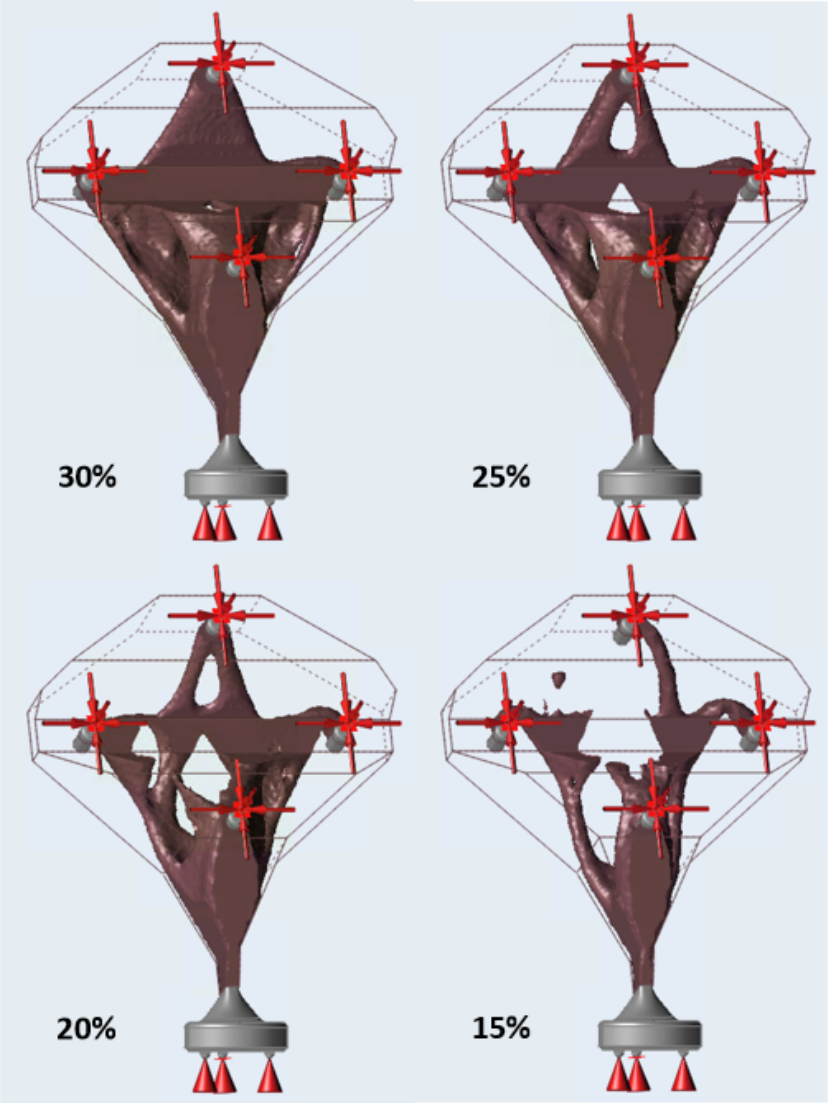

Figure 57: TO with 45° overhang constraint and volume fraction of 30%, 25%, 20%, and 15%.

At about 15% volume fraction, disconnection started to occur in the design. Even with the overhang constraint applied in the structural topology optimization algorithm, support structures are still required under the left and right posts, as they are local minima which require anchoring during the layer by layer LPBF process. Design feature post-processing is necessary to generate self-supporting designs. As a result, a decision was made to run topology optimization without the overhang constraint in order to get more relaxed designs and then manually modify them to make them self-supporting.

Figure 58 is a series of designs with topology optimization settings as listed in Table 10. At about 5% volume fraction discontinuity starts to occur in the design.

Table 10: Topology optimization setting-Scenario 2.

Load direction	Load magnitude	Volume fraction	Overhang constraint
Multiple	30N	30%, 25%, 20%, 15%, 10%, 5%	N/A

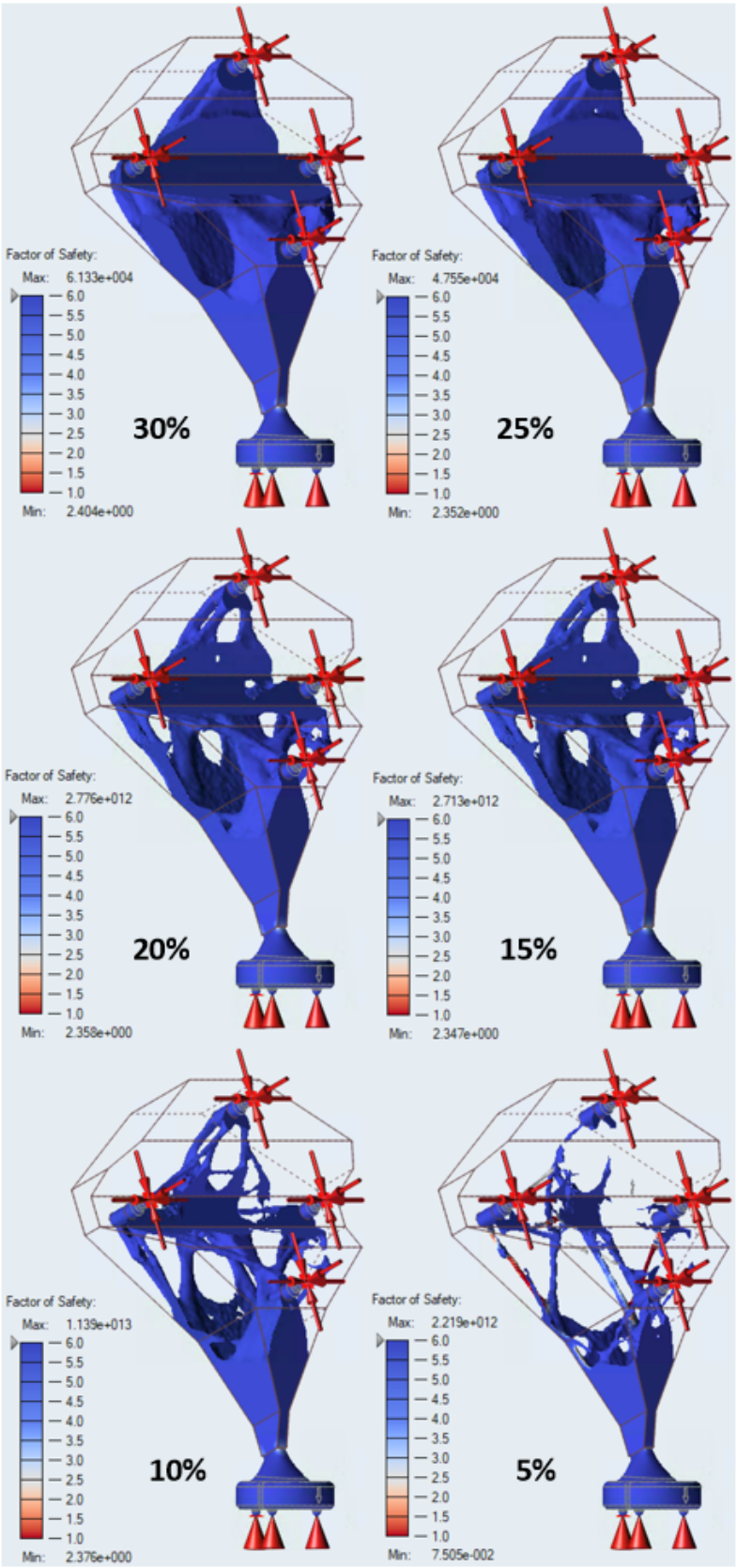

Figure 58: Multiple load cases TO with 30%, 25%, 20%, 15%, 10%, 5% volume constraint.

A Pareto front plot (Figure 59) showing the relation between design volume fraction and compliance (related to strain energy) was created, as the objective of this topology optimization is to minimize strain energy (i.e., maximize stiffness) while keeping the design as light weight as possible. It is shown that when volume fraction is larger than 10%, compliance does not decrease much as volume fraction increases. As a result, the topology design with 10% volume fraction was used as a reference to create a smooth, self-supporting final design.

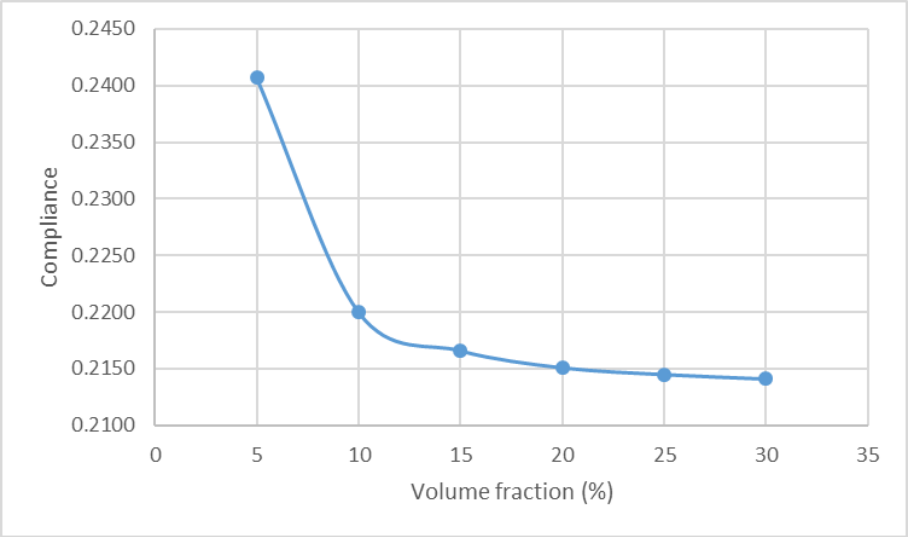

Figure 59: Pareto Front for topology optimization with multi-directionally load cases.

In Inspire, polynurbs were drawn around the topology structure to smooth out the facets, while keeping in mind that all overhangs should have angles larger than 45° relative to the build plate unless the overhang area is small. Inevitably, the final design would not follow the optimized topology design exactly. Some overhangs were eliminated or made self-supporting by rib structures. Some regions were reinforced as they may be too thin to print. The first iteration of the design, which is called the "Cobra", was created as shown in Figure 60. The cobra design grows "smoothly" from the build plate without major jumps in cross sectional areas within one layer and without any >45° overhang features, hence no support structure is required during fabrication via LPBF. It can be noticed that machining allowance (extra materials of about 5 mm

thick) were added to the posts and the bottom of the design. It is desired that, even though the part may be distorted after removal from the build plate, there is enough material left for post-machining to achieve positional and dimensional accuracy.

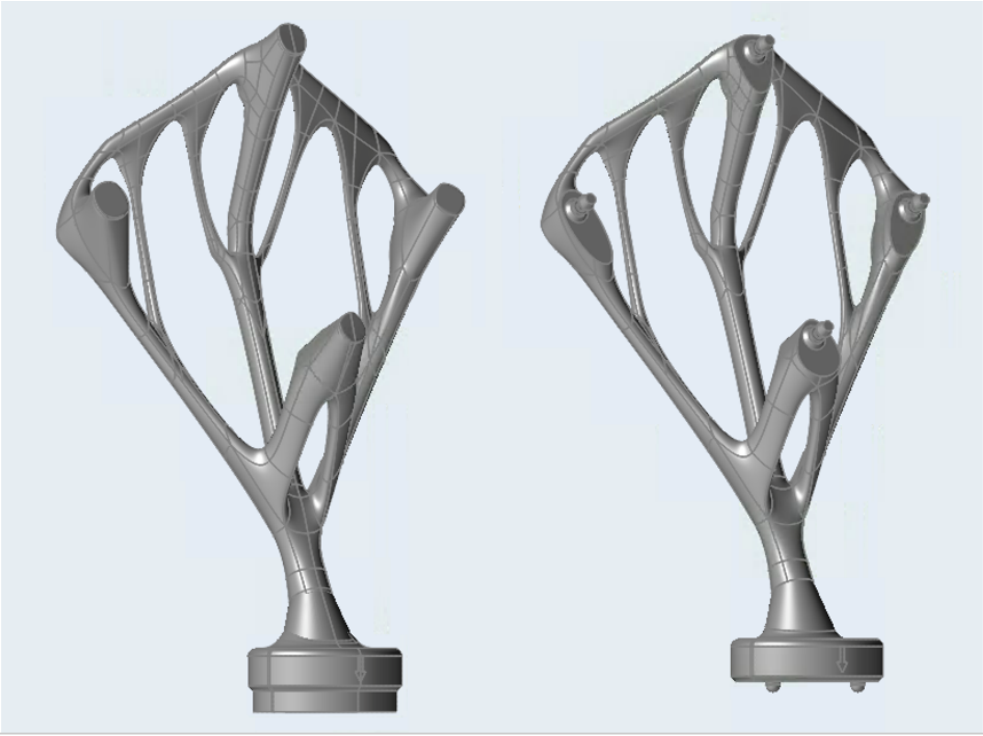

Figure 60: Cobra design before (left) and after (right) post-machining.

Stress analysis was performed on the Cobra design to evaluate its performance under the same loading conditions as applied in topology optimization. Results were listed in Table 11. The total mass of the Cobra tracker demonstrator is 73.5 g. The original tracker product assembly is 54 g. With loadings each of 30 N acting on the posts, the minimum safety factor is 3.178. In fact, a force as large as 30 N is unlikely to be applied on the tracker while the bottom is fixed during operation. As a result, the Cobra design is conservative on fail-safe and material may be removed from the design in next iterations.

Table 11: Cobra design performance.

Total mass	Volume fraction	Compliance	Minimum safety factor
76.5 g	9.7%	0.1967	3.178

Similarly, topology optimization was run with only normal forces acting on the posts of the tracker. Detailed settings were listed in Table 12. Figure 61 shows that, at about 5% volume fraction, the design started to become disconnected.

Table 12: Topology optimization settings-Scenario 3.

Load direction	Load magnitude	Volume fraction	Overhang constraint
Single	30N	30%, 25%, 20%, 15%, 10%, 5%	N/A

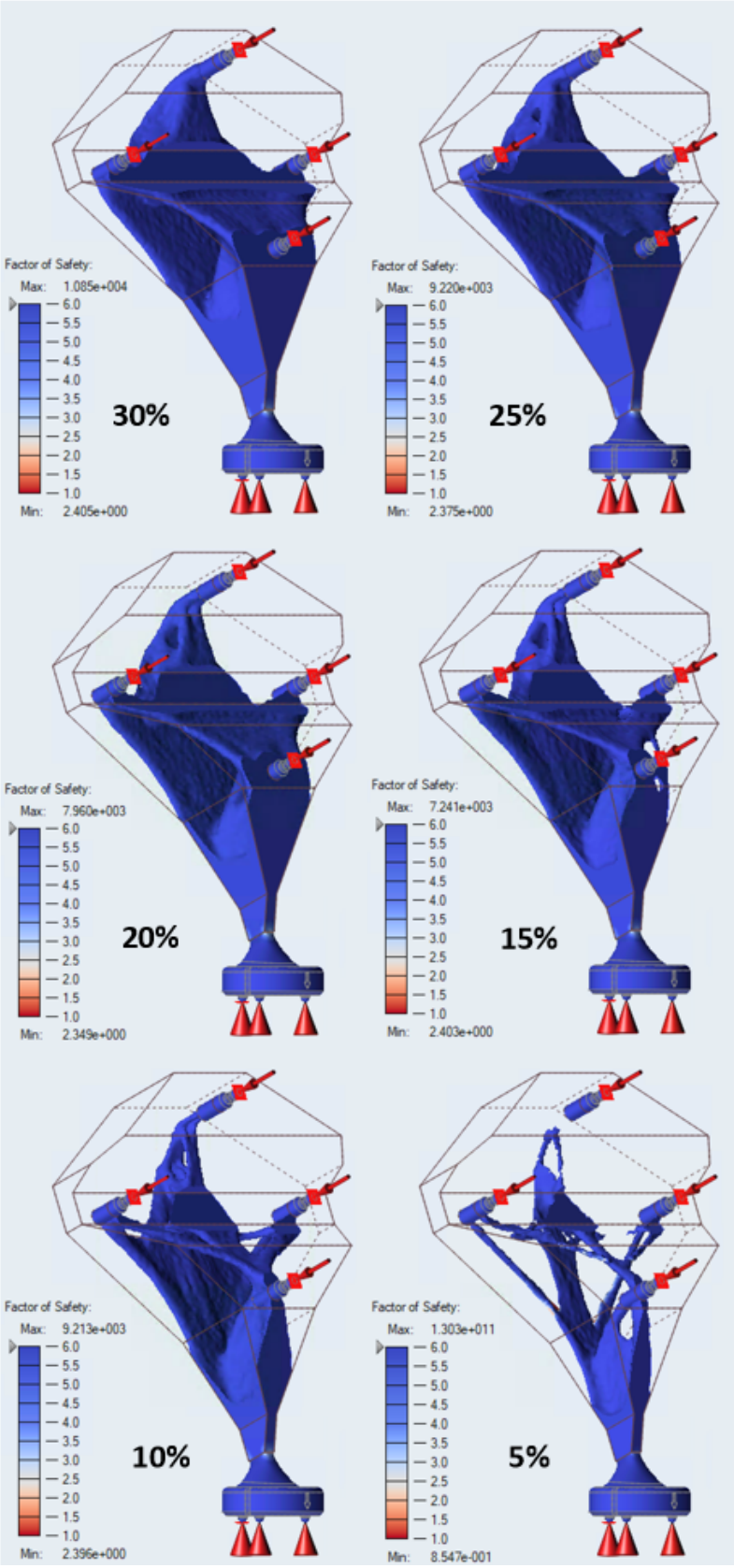

Figure 61: Single load case TO with 30%, 25%, 20%, 15%, 10%, 5% volume constraint.

The Pareto front plot (Figure 62) implies that when volume fraction is larger than 10%, compliance change becomes less sensitive to volume change of the design. As a result, it was aiming to create a design with 10% volume fraction of the design space.

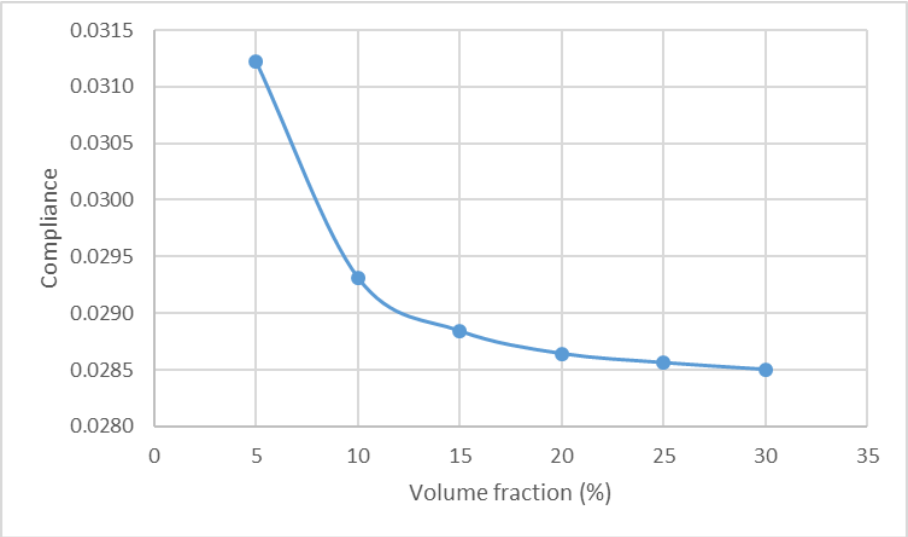

Figure 62: Pareto front for topology optimization with single load case.

Polynurbs were also drawn around the topology structure of 10% volume fraction when trying to trace the topology design and modify it so that it can support itself. The modified design, which is called the "ET", was created as shown in Figure 63. No support structure is needed during the fabrication of the ET design. Machining allowance (extra materials of about 5 mm thick) were added to the posts and the bottom of the design.

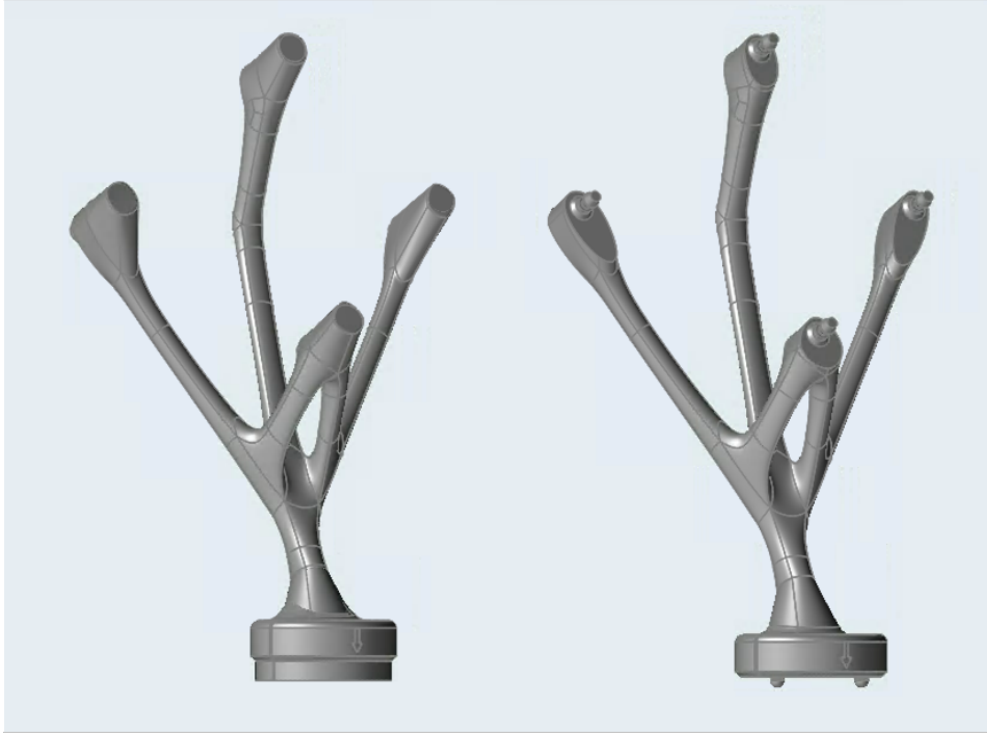

Figure 63: ET design before (left) and after (right) machining.

Stress analysis was performed on the ET design to evaluate its performance under the same loading conditions as applied in topology optimization. Results were listed in Table 13. The total mass of the ET is 69.3 g which is of 8.3% volume fraction of the design space. The minimum safety factor is 2.468 under the same loading as in topology optimization. The ET design is lighter than the cobra design but it is slightly heavier than the original assembly.

Table 13: ET design performance

Total mass	Volume fraction	Compliance	Minimum safety factor
69.3 g	8.3%	0.0717	2.468

Although at the first iteration, the Cobra and ET designs are heavier than the original tracker assembly, they are stiffer than the original design. The original design will yield under the 30N multi-directional loadings as the stress analysis results shown in Figure 64. It is possible to further reduce the weight of the Cobra and ET designs while making sure the performance is still

acceptable. For the first iteration, the Cobra and ET designs were printed and post-machined in order to examine the machinability of complex AM parts.

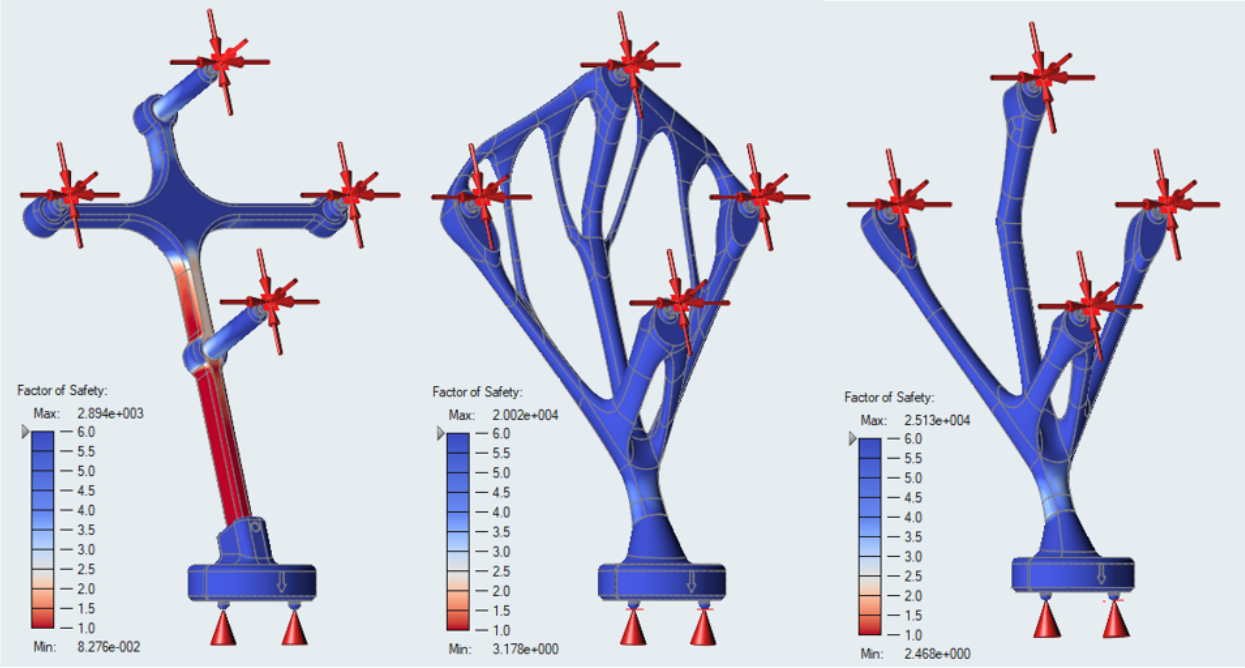

Figure 64: Safety factors of different tracker designs.

4.2.2 Geometric fidelity quantification of the AM design versus simulation and fabricated part

Best fit alignment at the base of the part between the scan data of the printed parts and the CAD as well as between the simulated geometry and the CAD were performed (Figure 65). The best fit alignment compared every point in the scanned or simulated data with their nearest neighboring point in the CAD and calculated a displacement distance. By applying the least squares algorithm the scanned or simulated point set was transformed so that the sum of the squared distance between the matching points in the two sets is minimal.

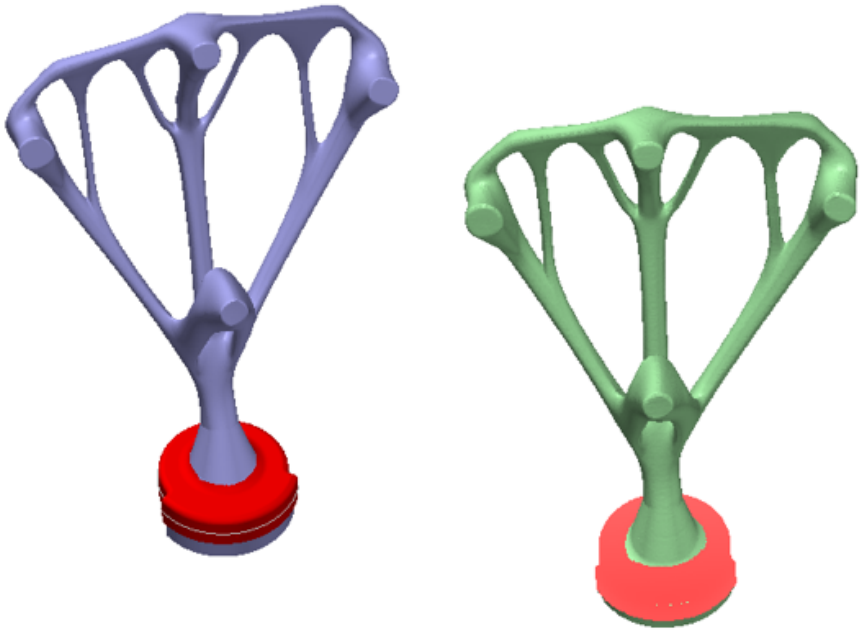

Figure 65: Best fitted region (red) for scanned printed parts and CAD, and simulated part and CAD.

Table 14 and Table 15 summarized the alignment statistics of the Cobra and ET designs with the CAD respectively. Both the scanned and simulated geometries align well with the CAD at the base. For the Cobra and ET designs, both the scanned and simulated results show maximum shrinkage of about 0.2 mm in the radial direction which may result from contraction of metal on cooling.

Table 14: Cobra design scanned and simulated geometric distortion with best-fit alignment at the base with CAD.

	Scan-CAD	Simulation-CAD
Iterations	6	6
Convergence	1.40152e-10	4.07458e-8
Distortion measured at the base cross sections [mm]	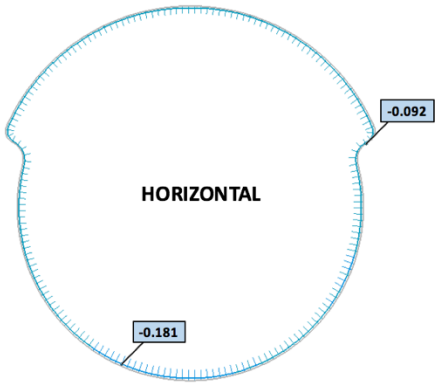	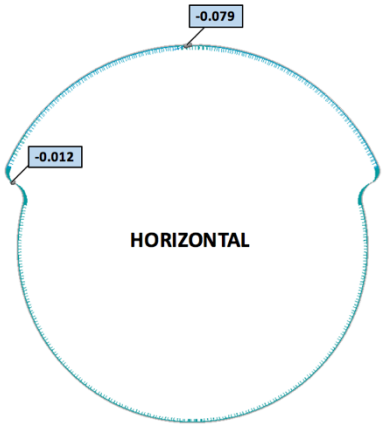
	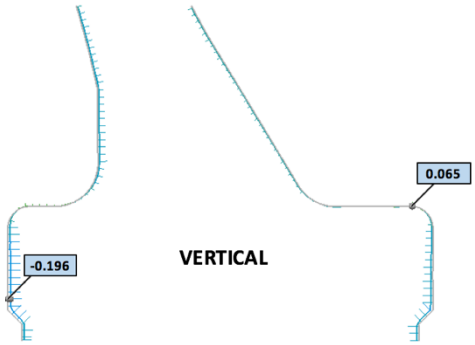	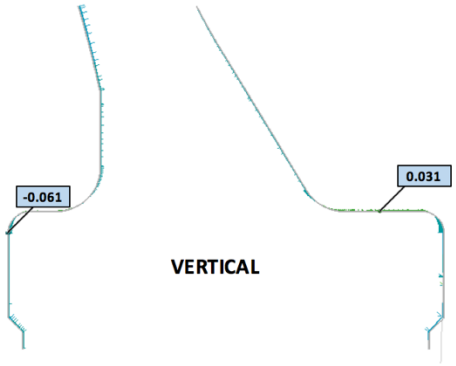

Table 15: ET design scanned and simulated geometric distortion with best-fit alignment at the base with CAD.

	Scan-CAD	Simulation-CAD
Iterations	7	6
Convergence	1.95312e-9	7.16334e-9
Distortion measured at the base cross sections [mm]	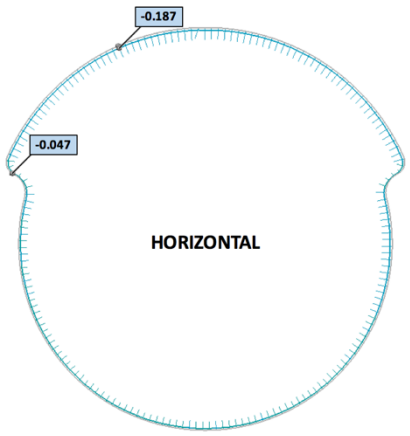	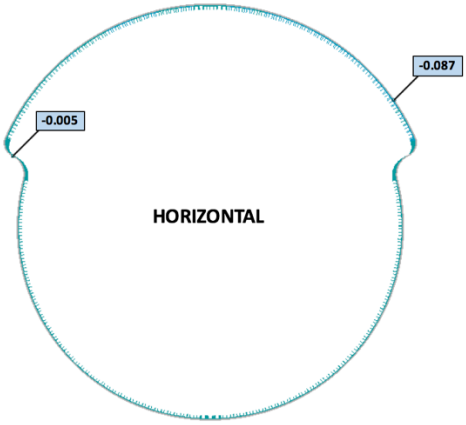
	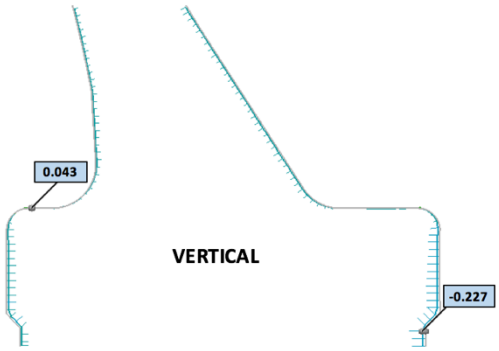	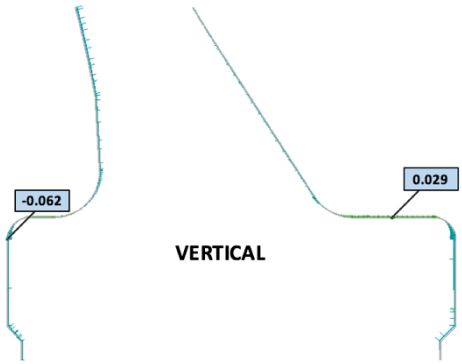

Table 16 compares general scanned and simulated distortion of the Cobra design with best fit alignment at the base. The scanned tracker and the simulated tracker deformed in opposite directions which lead to negative distortion values (a lack of material compared to CAD) at the scanned tracker tips and positive distortion values at the simulated tracker tips (an excess of material).

Table 16: Cobra design general scanned and simulated geometric distortion with respect to CAD.

Scan-CAD [mm]	Simulation-CAD [mm]
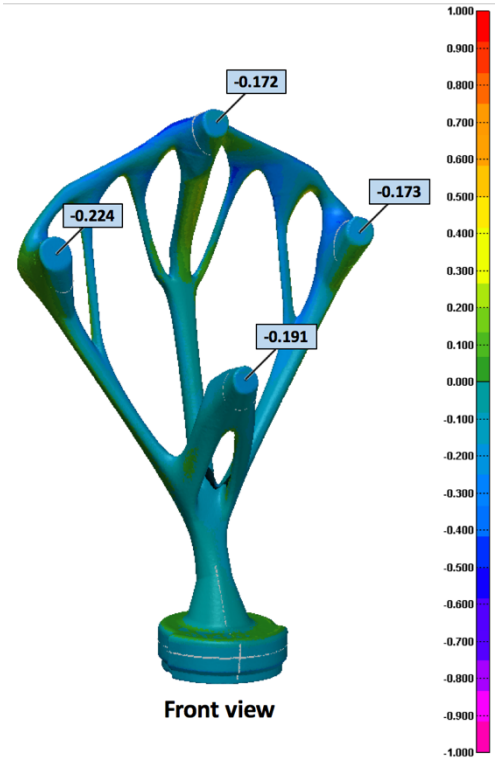 Front view	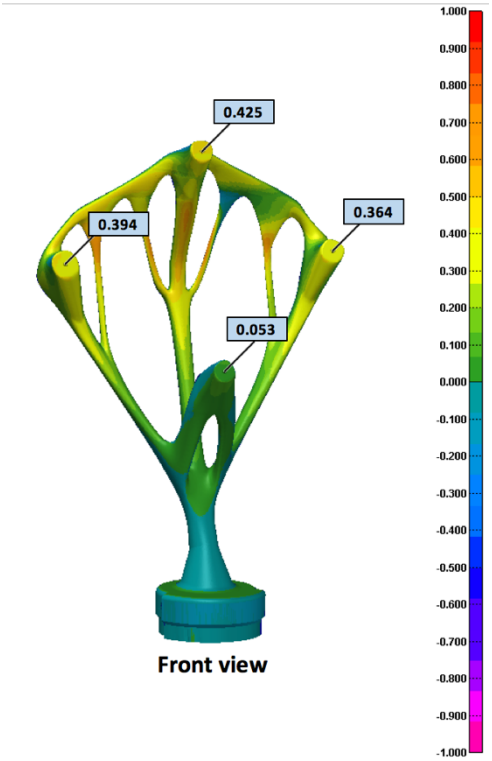 Front view
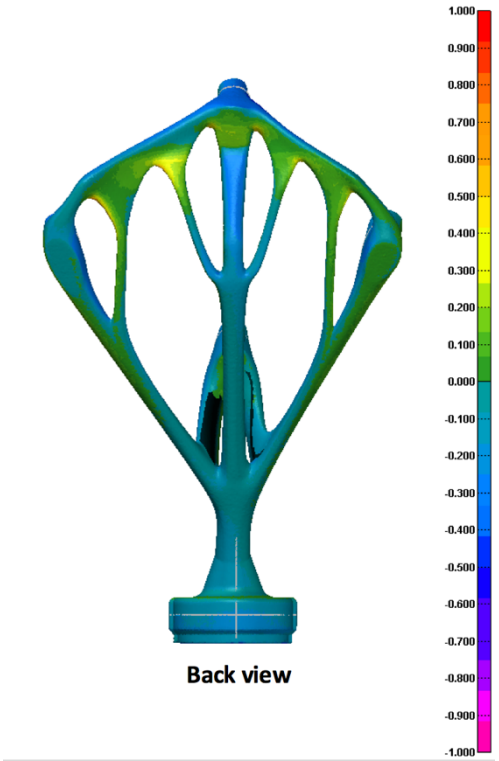 Back view	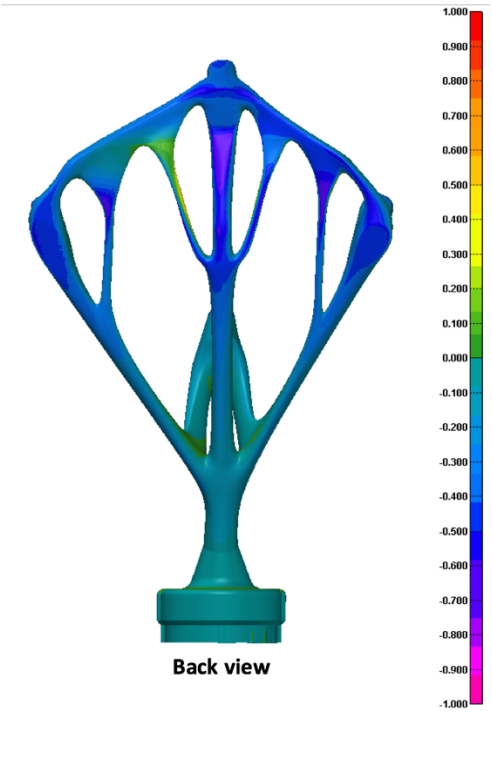 Back view

Table 17: ET design general scanned and simulated geometric distortion with respect to CAD.

Scan-CAD [mm]	Simulation-CAD [mm]
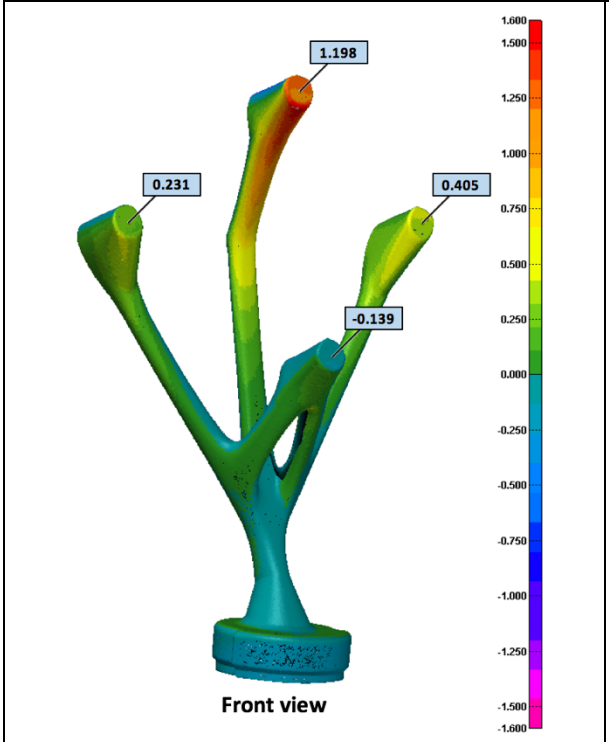	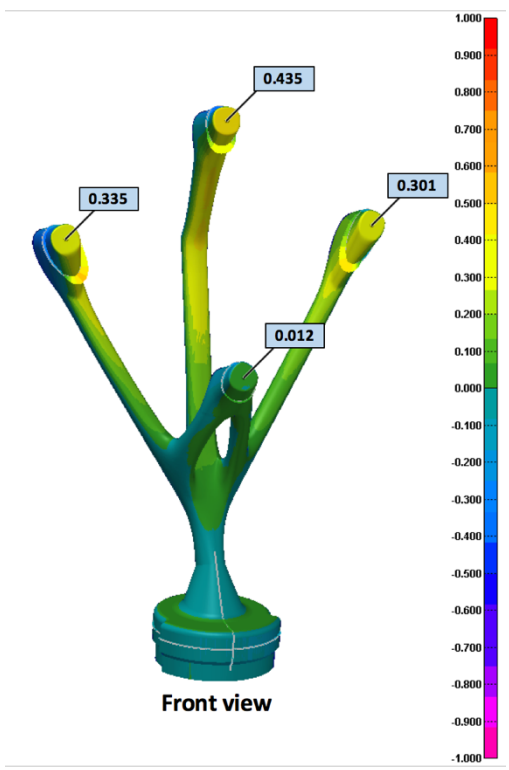
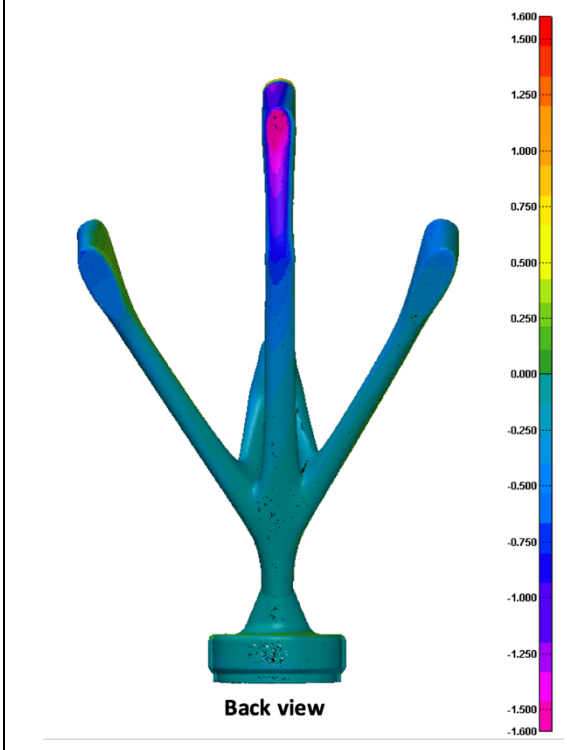	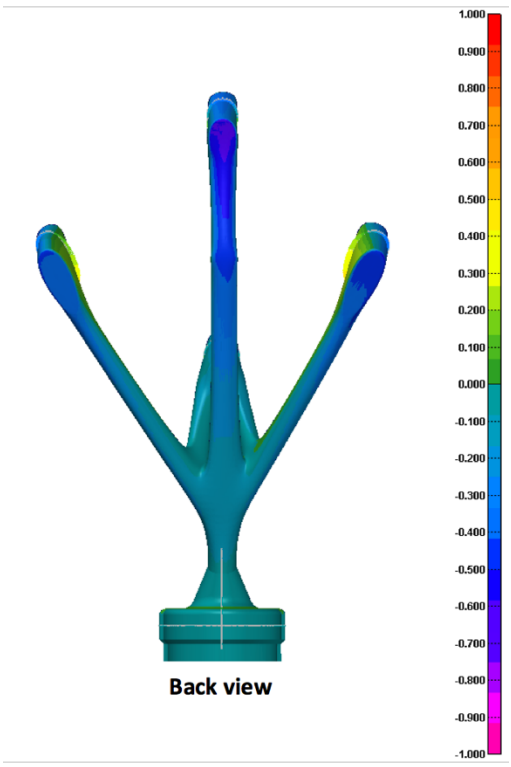

Table 17 shows the comparison between the scanned and simulated general distortions of the ET design. Results show that in the case of the ET design where the upper post is not connected to the left or right post as it is in the Cobra design, actual deviation observed at the tip of the upper post (1.198 mm) is more significant than that in the Cobra design (-0.172 mm). This implies that distortion of printed parts is, as anticipated, geometry-dependent. The scanned and simulated distortion deform in the same direction but the amount of distortion is underestimated in the simulation.

Table 18 and Table 19 display the scanned and simulated distortion measured at post cross sections of the Cobra and ET designs. For the Cobra design, the scanned and simulated parts both shifted downwards by about 0.1 – 0.5 mm at the posts. The scanned cross sections are slightly smaller than the CAD while no obvious difference is observed in the size of the post cross sections of the simulated part and the CAD. The post positions of the scanned and simulated ET tracker also shifted downwards compared to the CAD model with the printed upper post shifted down by as much as about 1.5 mm which was underestimated by the simulation.

Table 18: Cobra design scanned and simulated distortion with respect to CAD (grey) measured at the post cross sections.

Scan-CAD [mm]	Simulation-CAD [mm]
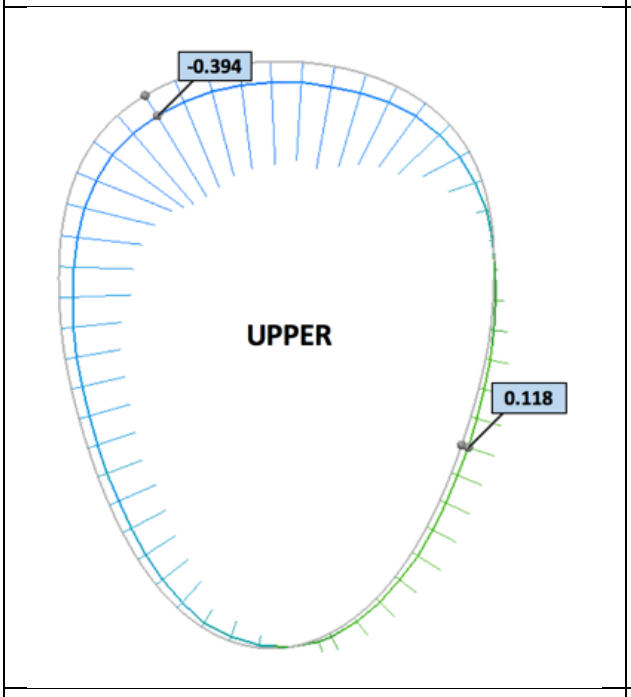	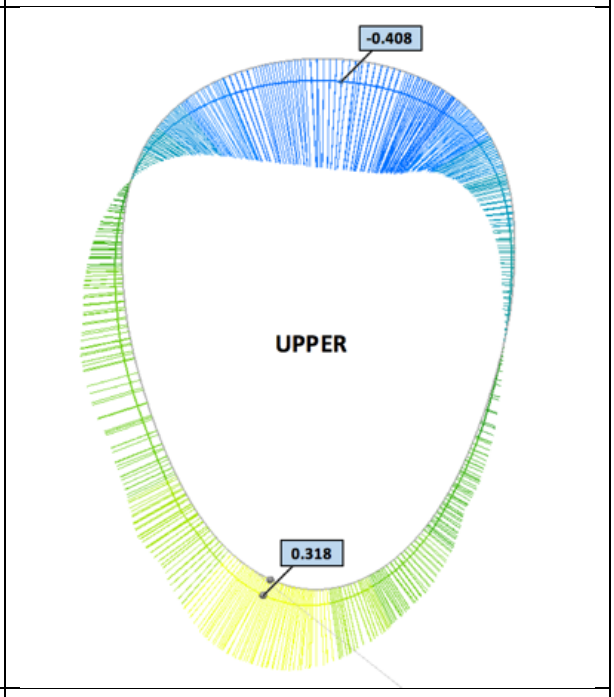
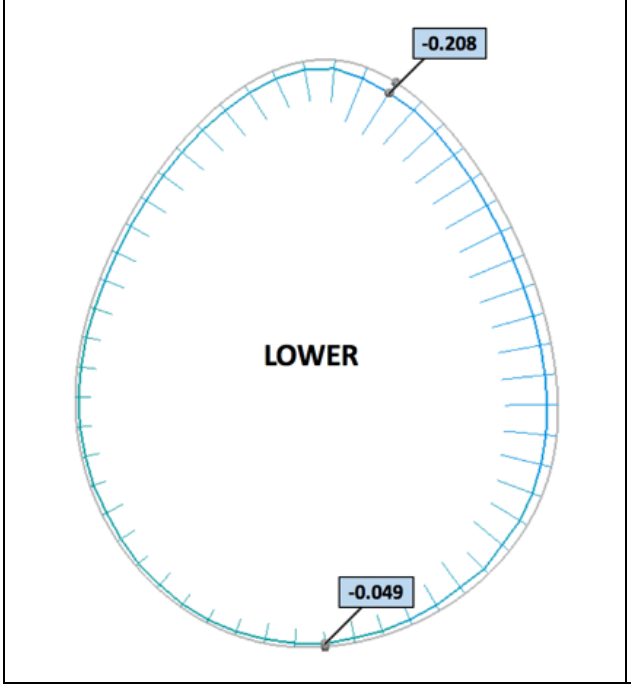	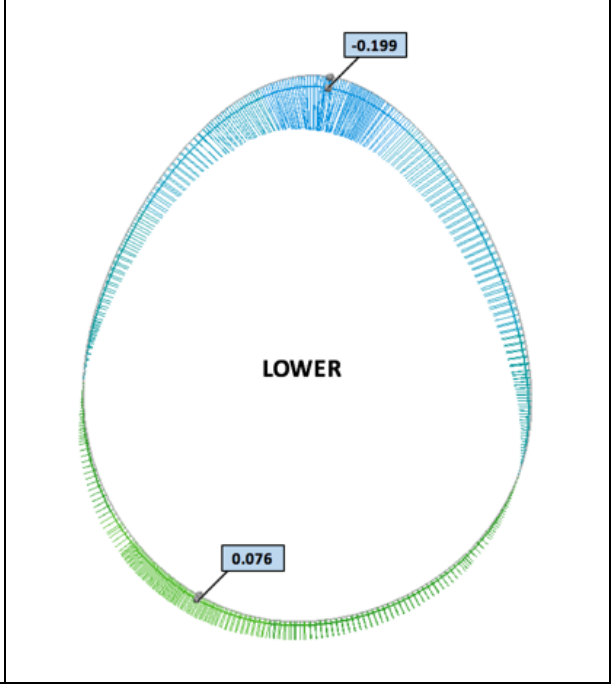

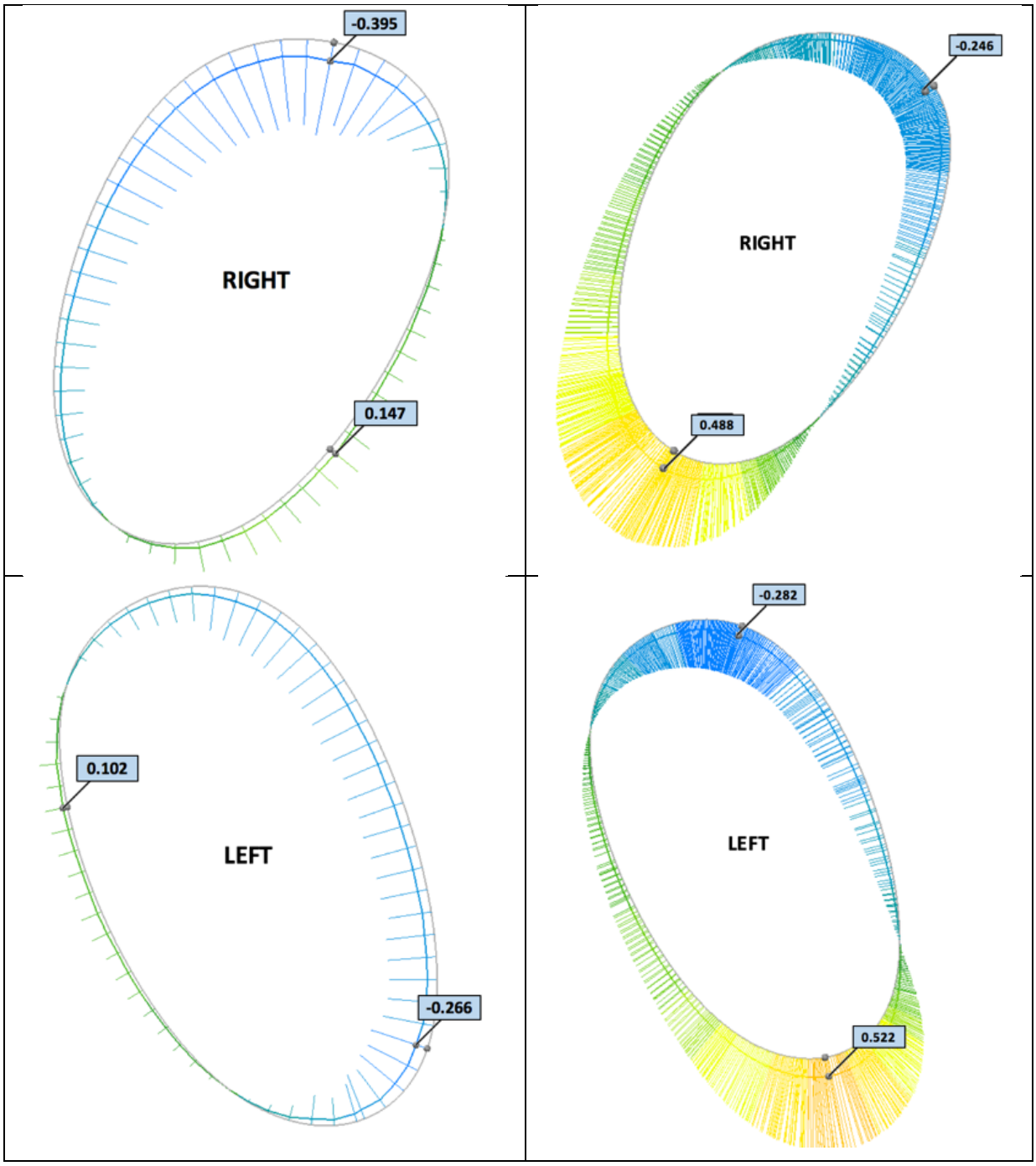
-0.395
RIGHT
0.147
-0.246
RIGHT
0.488
0.102
LEFT
-0.266
-0.282
LEFT
0.522

Table 19: ET design scanned and simulated distortion with respect to CAD (grey) measured at the post cross sections.

Scan-CAD [mm]	Simulation-CAD [mm]
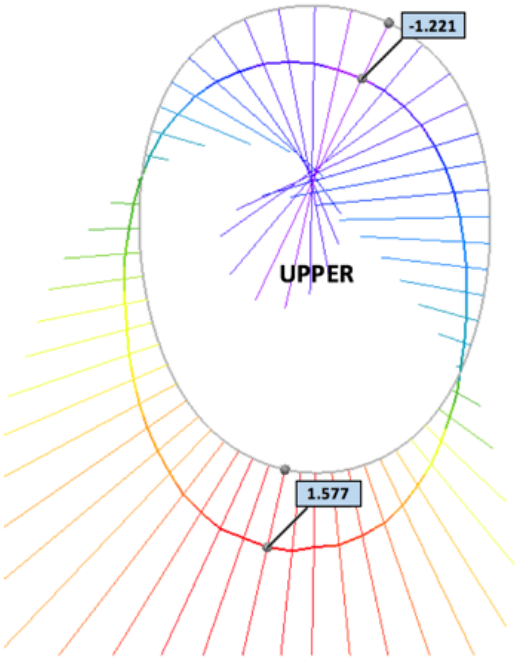	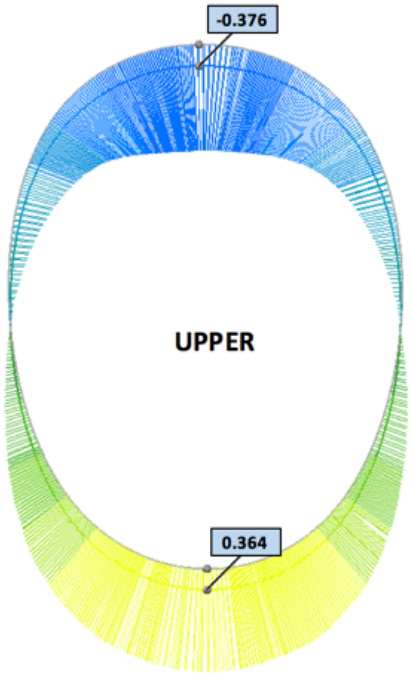
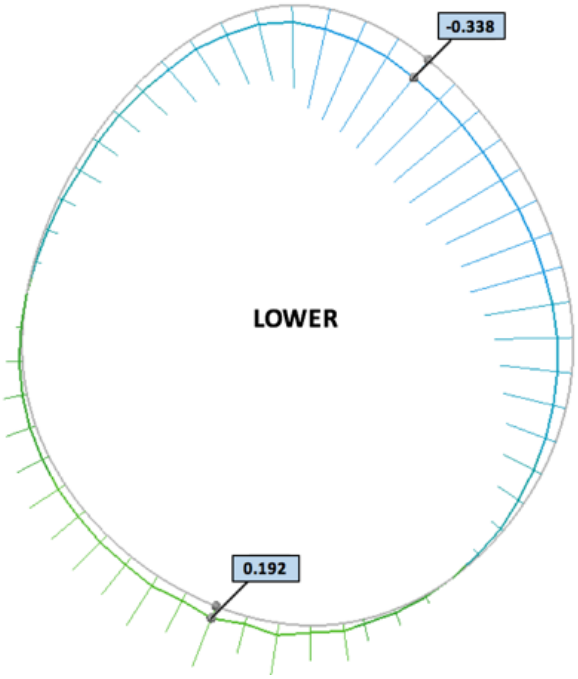	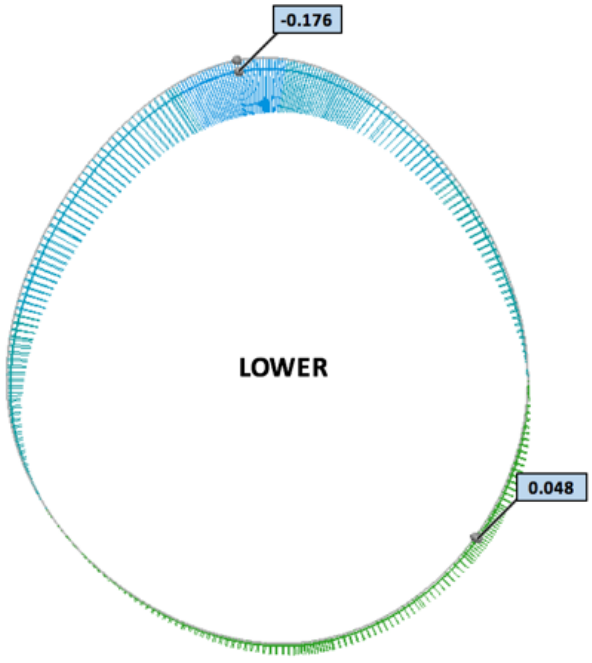

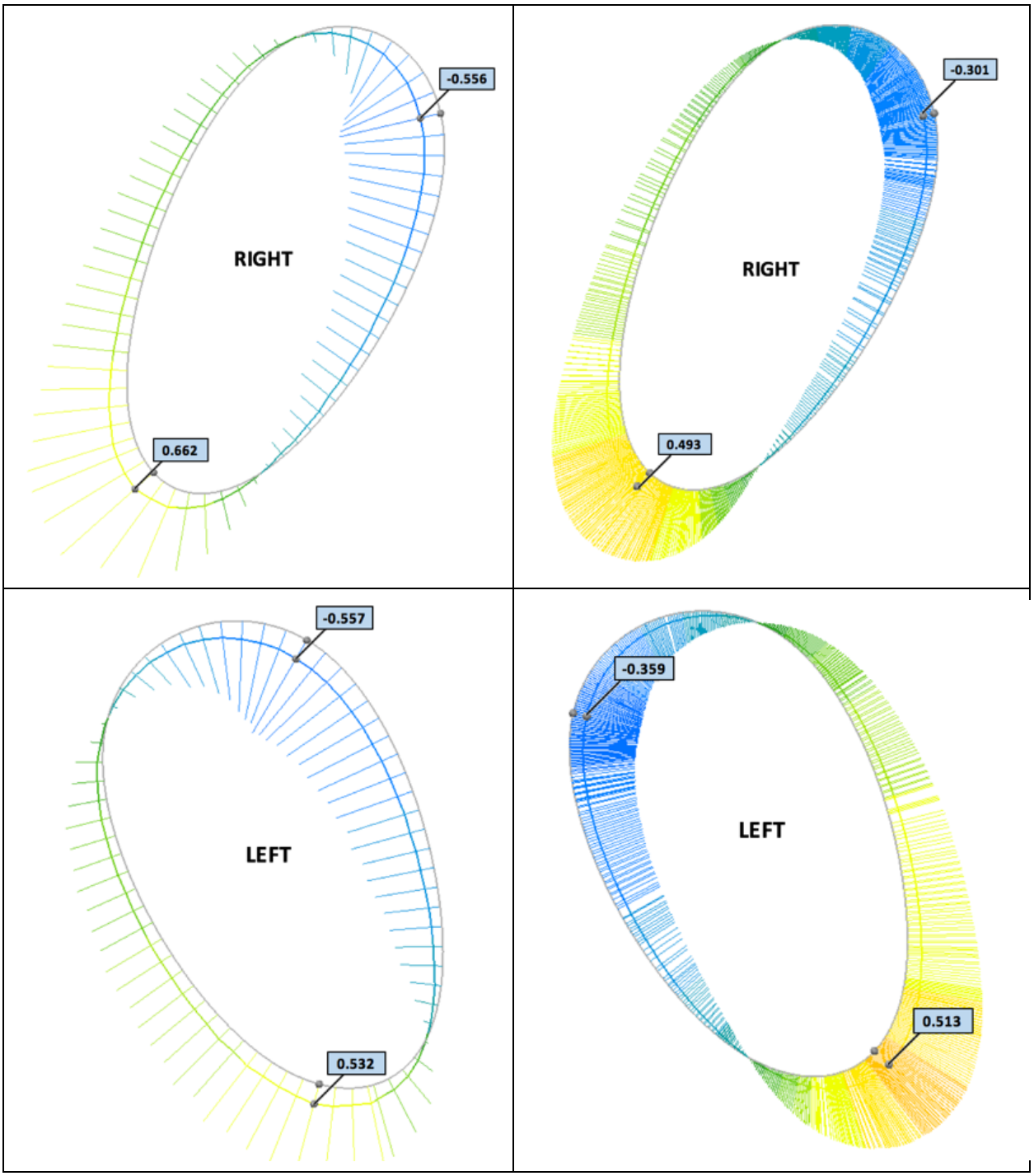
-0.556
RIGHT
0.662
-0.301
RIGHT
0.493
-0.557
LEFT
0.532
-0.359
LEFT
0.513

4.3 Summary

Distortion of printed parts can be minimized through design optimization, since distortion is dependent on part geometry, as it was demonstrated in the Cobra and ET designs. If the simulation can predict distortion accurately, it is possible to compensate the design in order to pre-emptively minimize the distortion after printing or to change design features sensitive to distortion. For instance, the Cobra design has interconnected features between posts, whereas the ET design has free posts.

There are factors which may have led to the deviation between the scanned (actual) and simulated geometric distortion. For example, the thermomechanical model used may have not been able to capture enough physics of the LPBF process. Some of the uncertainty lies in the modeling of the laser-material interaction, where the complexity of the material melting, vaporization, and solidification is simplified to reduce computation time. Especially for complex geometries which consist hundreds of layers, errors could build up as layer increases. To this effect, the print parameters used in this simulation may not reflect accurately the true process parameters in effect. Simulation parameters typically need to be tuned against the measured temperature or distortion. Also small errors which occurred in the best fit alignment at the base can be magnified at the post tips due to the fact that the upper post is about 15 mm away from the base.

The thermal simulated distortion may not reflect the actual distortion accurately. The as-printed part therefore cannot fulfil perfectly the desired positional and dimensional precision, as such, machining allowance of about 5 mm thick was added to regions where post-machining is required to produce matting surfaces that are within tolerance.

Chapter 5

Design and Manufacturing Considerations for Machining

The experimental work involved in this section was done in collaboration with the Precision Control Lab (PCL). The role of the author was data collection and analysis of cutting tests and chatter stability of the milling cutter. Chatter stability comparison of different fixturing methods was done with the help of Dr. Ahmet Okyay from PCL. Machining of the trackers was done at the facility of Renishaw Canada. Machining parameters and tool path planning was done by Mr. Carl Hamann from Renishaw.

5.1 Methodology

5.1.1 Cutting Coefficients Identification

Microstructure and mechanical properties of AM parts may be influenced by printing parameters and, as a result, cutting force coefficients of AM parts may differ from conventional parts made of the same material. Cutting tests have been conducted on AM Ti64 artifacts to identify cutting force coefficients experimentally.

The cutting tests were conducted using the 3-axis Haas CNC machine (Figure 66). A dynamometer (Kistler, 9255A 3-component stationary dynamometer) was mounted on the worktable to measure cutting forces in the workpiece coordinate system. The artifact was fixed on the dynamometer with a vise. The top surface of the artifact was milled ahead of time so that it is perpendicular to the cutter. The dynamometer was connected to a charge amplifier from which the output was sent to a data acquisition card (NI DAQCard). The measurements obtained through the NI DAQCard were

processed using MALDAQ software by CutPro®. In collecting data, a sampling frequency of 10240 Hz was used without any filtering.

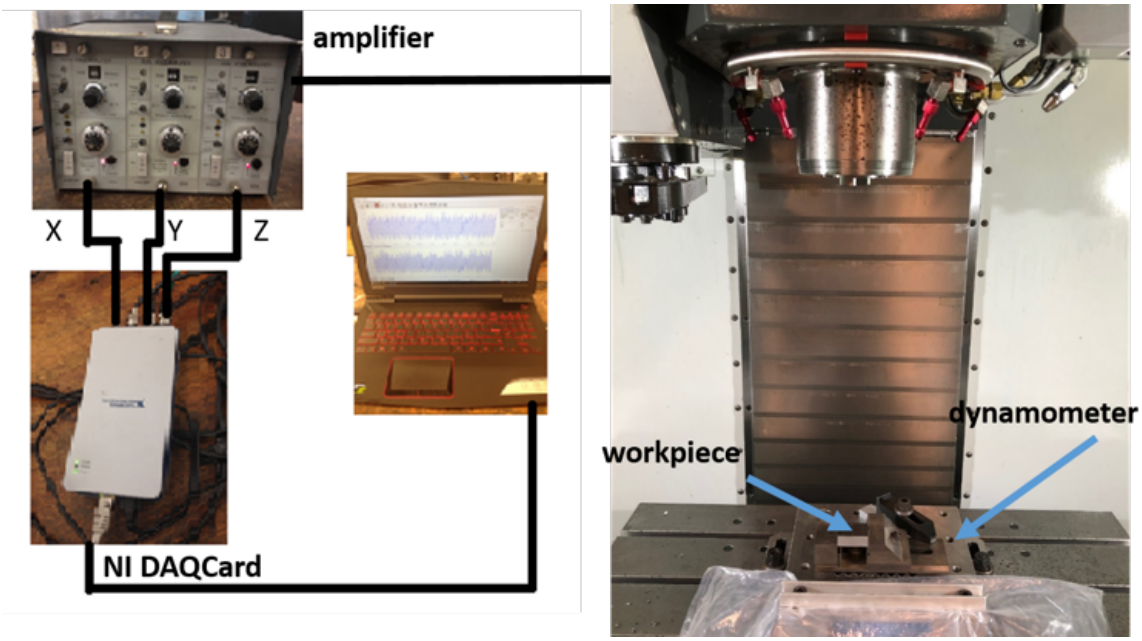

Figure 66: Cutting test setup.

A series of cutting tests in the down-milling direction were performed with a 4 flutes, 12.7 mm coated carbine helical end mill with a 5° rake angle. As listed on Table 20, different combinations of cutting parameters (i.e., radial immersion, depth of cut and spindle speed) were considered to explore their effects on cutting coefficients. Each experiment was run at 6 different feedrates and was repeated several layers into the workpiece until there was not enough material left for cutting. Each experiment was repeated at least 3 times. For ¼ radial immersion milling, cutting at each feedrate was repeated twice at each layer (Figure 67).

Table 20. Cutting conditions for cutting experiments.

Experiment No.	Artifact	Radial immersion	Depth of cut [mm]	Spindle speed [rev/min]
1	Stripe	1/2	1	1750
2	Stripe	1/2	3	1750
3	Stripe	1/2	3	1000
4	Stripe	1/4	3	1750
5	Meander	1/2	1	1750
6	Meander	1/4	3	1750
7	Meander	1/4	3	1570

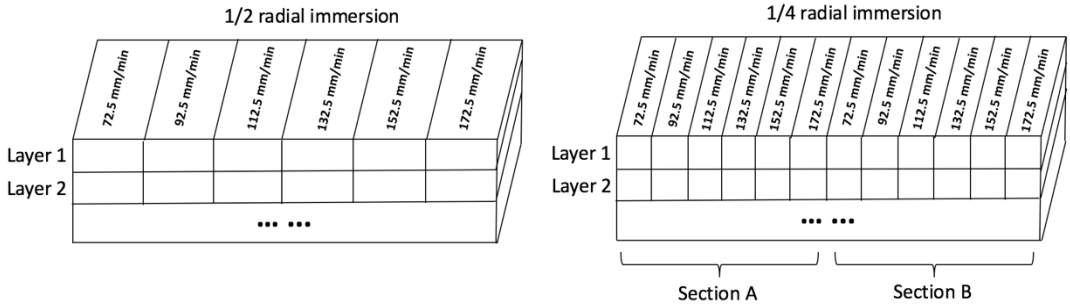

Figure 67. ½ and ¼ immersion milling tests on artifacts.

The average was taken among one hundred force cycles in the steady state region of the measured cutting forces (Figure 68).

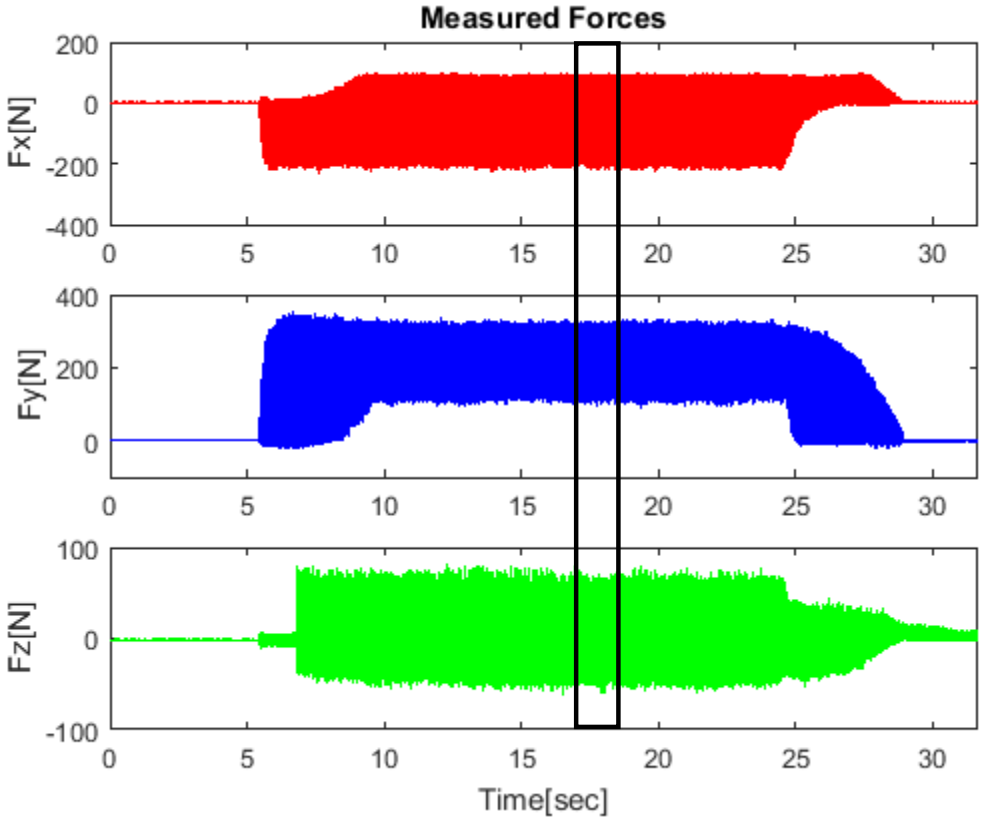

Figure 68: Sample cutting forces in the steady state region.

The average forces per tooth period were calculated which were then plotted versus feed per tooth. According to Equation (2.5.1.17)-(2.5.1.19) in Section 2.5.1, average forces per tooth period ($\bar{F}_x, \bar{F}_y, \bar{F}_z$) and feed per tooth ($c$) have linear relationship. As a result, linear regression was taken between average forces and feed per tooth and the slopes and y intercepts of the fitted trend lines were identified (Figure 69). Cutting coefficients were obtained by solving Equation (2.5.1.26). The identified cutting coefficients were used in cutting force simulation and chatter stability analysis.

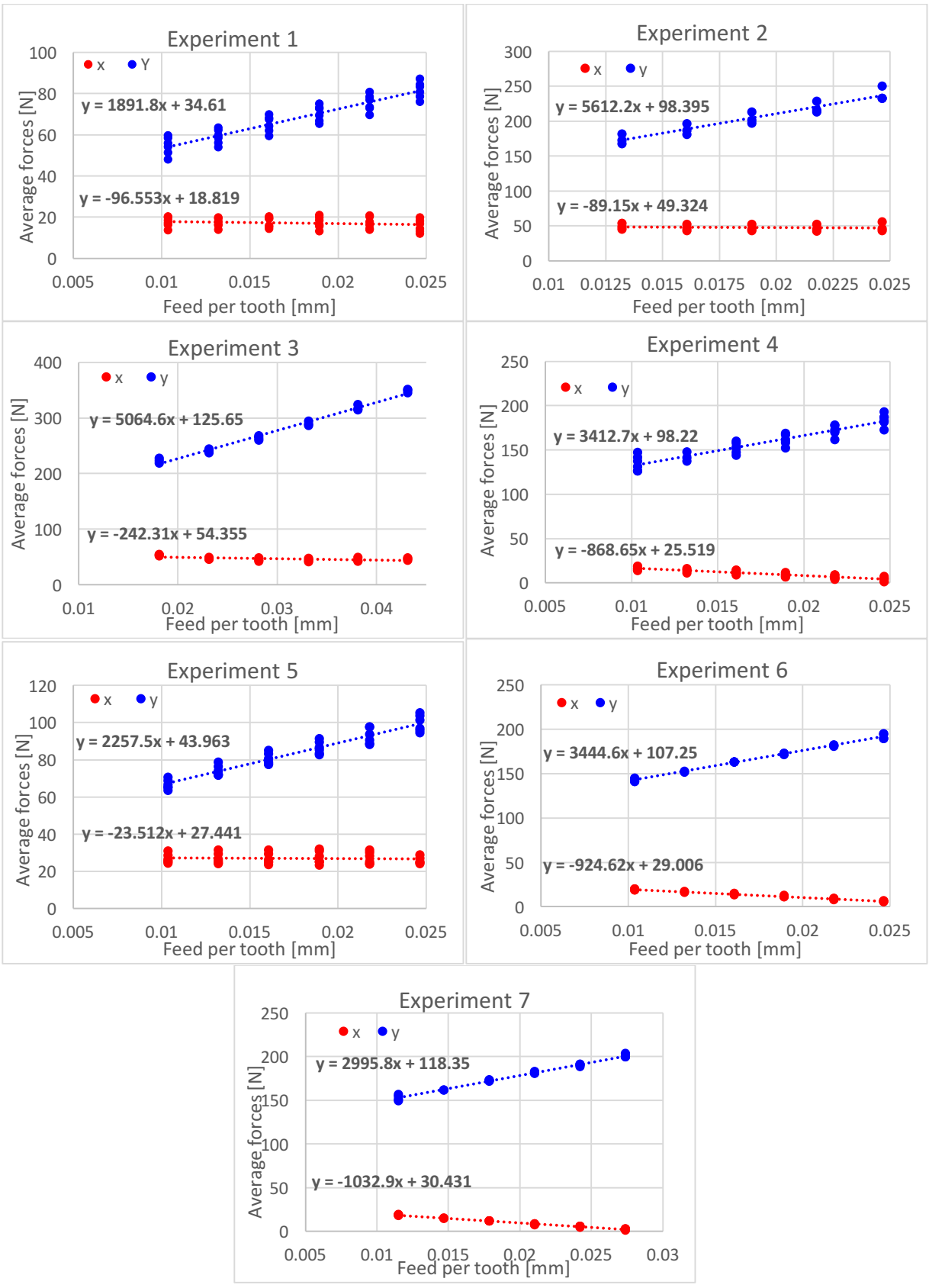

Figure 69: linear regression between average forces and feed per tooth.

5.1.2 Modal Analysis

The vibratory dynamics of a machine tool structure needs to be measured in order to predict the maximum stable depth of cut as a function of spindle speed. Impact hammer testing was conducted at the tip of the milling tool in X and Y directions (Figure 70) to obtain the FRFs (frequency response function).

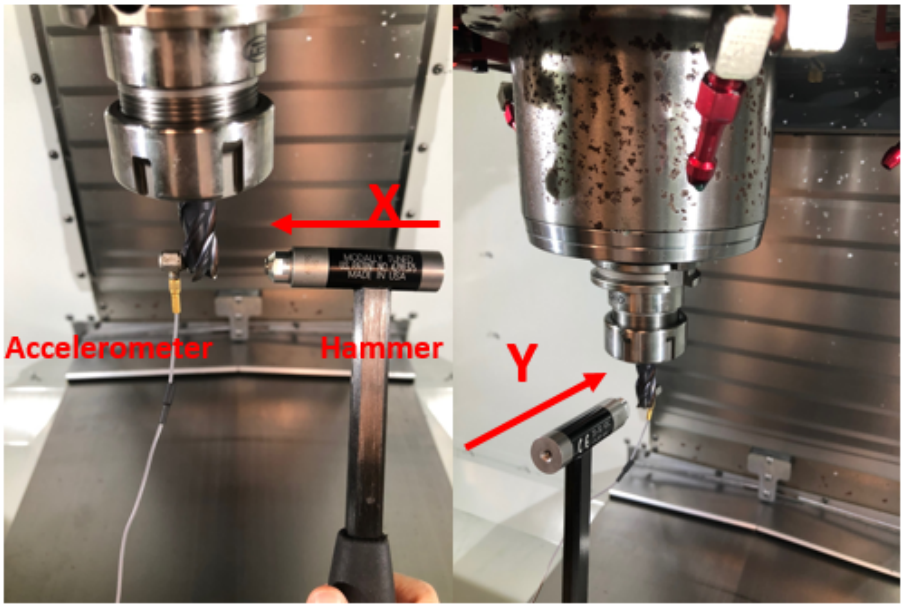

Figure 70: Impact hammer testing at milling tool tip in X and Y direction.

An accelerometer (Dytran Instruments, model: 3055AG) was attached to the tip of the milling tool using special wax to measure acceleration under excitation with a sensitivity of 96.2 mV/g (output signal). An impulse hammer with force sensor and a medium tip (white plastic) (PCB Piezotronics, model: TLD086C01) was used to hit the tool at the tip with as perfect an alignment as possible with the axis measured (input signal with a sensitivity of 11.2 mV/N). Data was collected in the frequency range from 0 to 10000 Hz. Five measurements were taken in each direction and the average was computed in order to cancel out random errors such as electrical

noise during the impact harmer testing. The measurements were processed by using the tap testing module MALTF by CutPro®.

The natural frequencies and damping ratios of the machine tool system were identified by using the "peak picking method" [111]. The peaks or dips of the imaginary part of the accelerance FRF occur at natural frequencies. After finding the natural frequencies (ω_r, where the subscript r denotes the mode number), the damping ratios can be extracted from the real part of the accelerance FRF. The peak/dip frequency pairs ($\omega_{r,1}\ and\ \omega_{r,2}$) in the real accelerance FRF plot each of which enclose a natural frequency were identified. For example, the accelerance FRF of a single degree of freedom (SDOF) system is shown in Figure 71. The natural frequency of the system ω_1 is 5000 Hz. The peak/dip frequency pair ($\omega_{1,1}$, $\omega_{1,2}$) is observed at (4759, 5286) Hz. The damping ratio (ζ_r) can be calculated from the frequency pair using [111]:

$$\zeta_r = \frac{(\omega_{r,2}^2 - \omega_{r,1}^2)(\omega_r)^2}{4\omega_{r,1}^2\omega_{r,2}^2}. \qquad (5.1.2.1)$$

The Imaginary peak (Q_r) of the accelerance FRF is identified as $Q_1 = 10\ \frac{m}{s^2 N}$ for the given SDOF system.

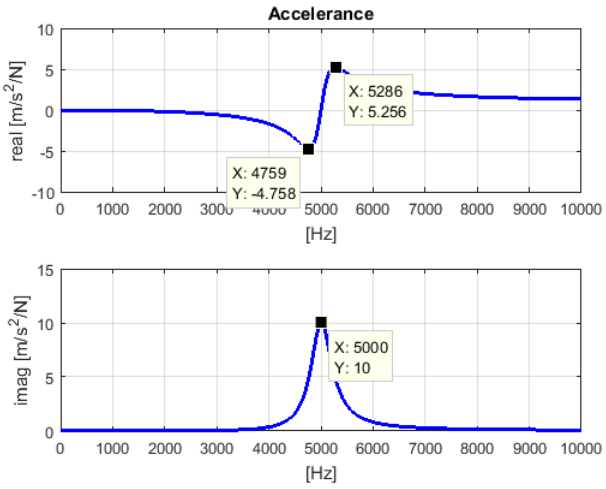

Figure 71: Accelerance FRF of a SDOF system.

The constituent modes broken-down from the FRF can be synthesized by superposition of the identified modes. By comparing the synthesized FRF to with the measured FRF, the accuracy of the identified modes can be assessed. The accelerance FRF ($A(\omega)$) is synthesized using the following formula:

$$A(\omega) = \sum_{r=1}^{N} \frac{-2z_r^2 \zeta_r Q_r}{(1-z_r^2)+j(2\zeta_r z_r)}, \tag{5.1.2.2}$$

where $z_r = \frac{\omega}{\omega_r}$ is the excitation to natural frequency ratio.

The displacement frequency response (receptance ($D(\omega)$) of the impact hammer testing can be obtained from the accelerance FRF by the following relation:

$$D(\omega) = \frac{A(\omega)}{-\omega^2}. \tag{5.1.2.3}$$

It is known that the imaginary part of a SDOF receptance FRF $\left(H(\omega)\right)$ can be expressed as:

$$H(\omega) = \frac{-2\zeta_r z_r}{k_r\left[(1-z_r^2)+(2\zeta_r z_r)^2\right]}, \tag{5.1.2.4}$$

where k_r is the modal stiffness.

It can be noticed that when $z_r = 1$, the imaginary receptance has a peak value ($Imag_{peak}$) which can be identified from the receptance FRF plot. Equation (5.1.2.4) becomes:

$$Imag_{peak} = \frac{-1}{2k_r\zeta_r}. \tag{5.1.2.5}$$

As a result, modal stiffness can be calculated as:

$$k_r = \frac{-1}{2\zeta_r Imag_{peak}}. \tag{5.1.2.6}$$

The modal mass(m_r) and stiffness has the following relation:

$$\omega_r = \sqrt{\frac{k_r}{m_r}} \tag{5.1.2.7}$$

Therefore, by rearranging the above equation, the modal mass can be obtained:

$$m_r = \frac{k_r}{\omega_r^2}. \tag{5.1.2.8}$$

The receptance FRF can also be synthesized as:

$$D(\omega) = \sum_{r=1}^{N} \frac{1}{m_r[(\omega_r^2 - \omega^2) + j2\zeta_r\omega_r\omega]}. \tag{5.1.2.9}$$

5.1.3 Chatter stability lobes of the milling cutter

In the actual machining process of the tracker posts, an 8 mm, 5 flute carbine coated milling cutter with a 5° rake angle was used. Ideally, cutting force coefficients should be identified for the new cutter-material combination. However, in this study, cutting force coefficients obtained from Section 5.2.1 were used when generating the chatter stability lobes as the cutter used in the cutting tests was made of the same material and has the same rake angle. Chatter stability lobes

of the milling cutter were generated using the "Zero Order" analytical solution as described in Section 2.5.2. Frequencies around the natural frequencies were scanned as the chatter frequencies occur near natural frequencies. Chatter stability lobes of the milling cutter (assuming the workpiece is rigid) for full, half, a quarter and 2.5% of the diameter of the cutting radial immersion cuts were compared.

5.1.4 Chatter stability lobes of the workpiece-fixture assemblies

In order to mount the printed part on the CNC machine for post-machining, an encapsulating fixture was designed and printed using ABS material (Figure 72). For the Cobra design, since the scanned geometric distortion is small which is within 0.5 mm, the cavity of the fixture was created by subtracting the CAD model of the Cobra design from the fixture. For the ET design, since the geometric distortion is as large as about 1.5 mm, the cavity was made by subtracting the scanned geometry of the ET design from the fixture.

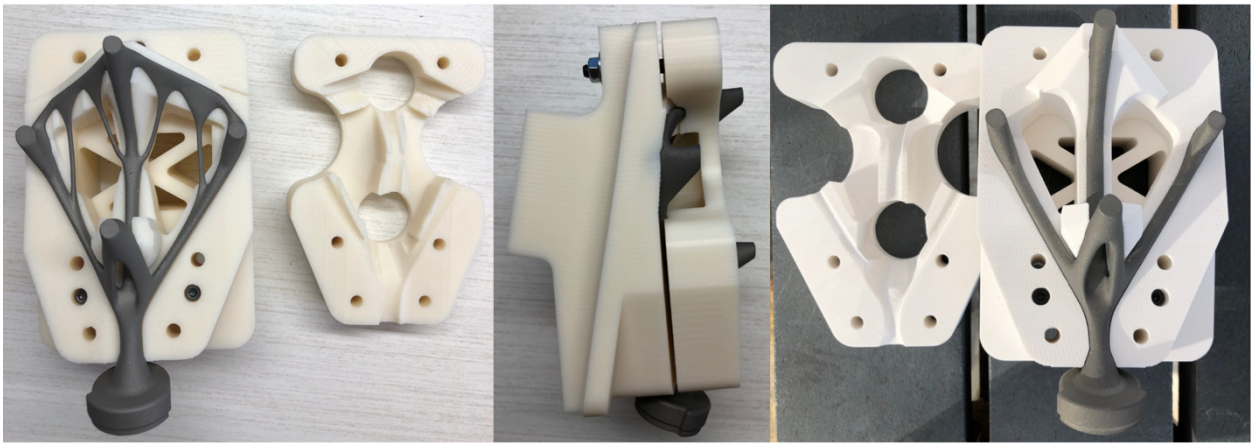

Figure 72: Encapsulating fixture.

During the inspection process of the Cobra design, the machined upper post of the tracker was out of tolerance (±25 μm) due to the fact that the tracker had been deformed under the clamping force exerted by the fixture. Once released from the fixture after machining, the tracker sprang

back and as a result, the high positional precision requirement could not be reached. The fixture with cavity created based on the scanned data of the tracker may solve the deformation issue but the suitability of the same fixture with parts printed at different location of the build plate or different machines cannot be guaranteed.

An alternative fixturing solution is to stabilize the tracker directly under the posts to be machined using UV cured adhesive polymer (Figure 73). It is suitable for fixturing flexible parts but the limitation is the accessibility of the UV device to some region of the part. For example, the UV device was blocked from the lower post of the tracker (image on the left of Figure 73). Severe vibration was observed when machining the lower post since it is not supported. As a result, a small fixture encapsulating the lower post was used along with the UV cured polymer fixture. The result shows that the specified tolerance is achievable.

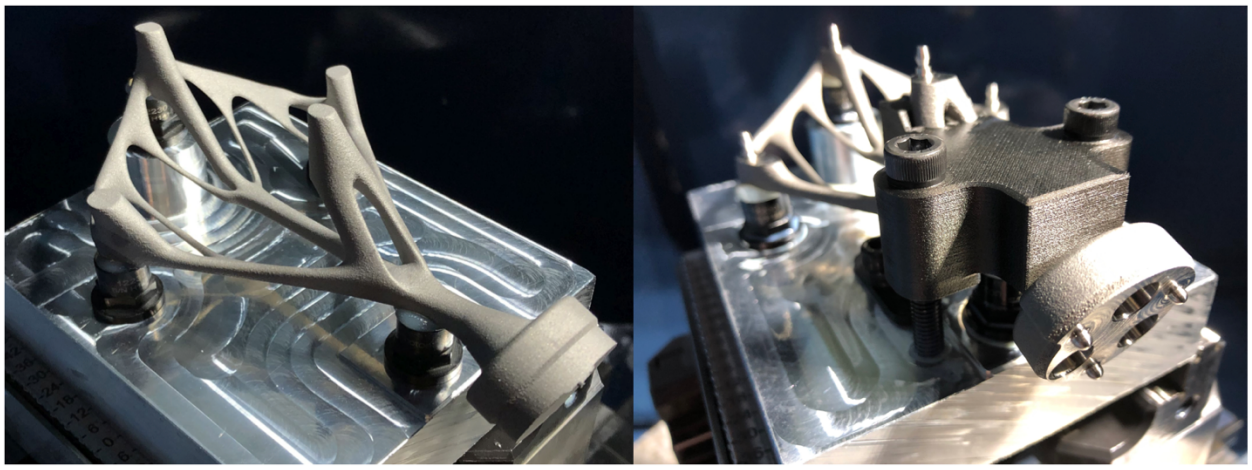

Figure 73: Fixture with UV cured adhesive polymer.

Chatter stability of the Cobra design mounted on the CNC machine with the ABS encapsulating fixture and the UV cured adhesive glue was compared to examine the stiffness contribution of the fixturing methods. Hammer impact testing was conducted on the Cobra design alone, the Cobra design encapsulated in a 3D printed ABS fixture and the Cobra design secured by UV

cured glue (Figure 74). An impact hammer (Dytran Instruments, model: 5800SL) hit the tracker at each post in X and Y directions. An accelerometer (Dytran Instruments, model: 3055AG) attached in the opposite direction measured acceleration outputs. The chatter stability lobes at each post position were generated using CUTPRO® by MAL, Inc.

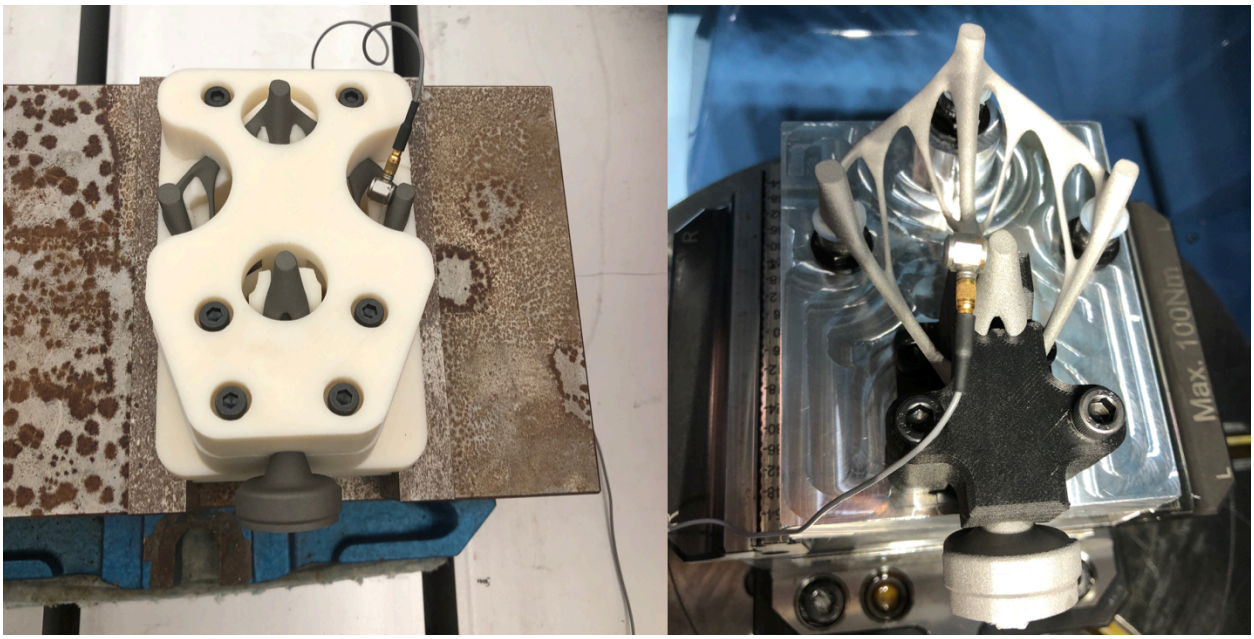

Figure 74: Impact hammer testing on different workpiece-fixture assemblies.

5.2 Results

5.2.1 Cutting coefficients identification

The accuracy of the cutting force coefficients was evaluated by calculating the RMS error and the average percentage error of the simulated average forces per tooth period against the measured average forces for each experiment. Cutting force coefficients identified for each experiments were summarized in Table 21 with the corresponding average RMS and percentage errors of the simulated forces.

By discretizing the helical milling tool along the length (Equation (2.5.1.11)-(2.5.1.13)) and summing up forces in the X, Y, and Z directions, cutting forces (F_x, F_y, F_z) were simulated analytically. Figure 75 and Figure 76 are simulated versus measured forces obtained on the stripe artifact for half and a quarter radial immersion down-milling with 3 mm depth of cut, 1750 rpm spindle speed, and 132.5 mm/min feedrate. Additional simulated and measured cutting forces comparisons under different cutting conditions are shown in Appendix B.

Table 21: Cutting force coefficients and simulated force errors.

Experiment No.	Ktc (N/mm^2)	Krc (N/mm^2)	Kte (N/mm)	Kre (N/mm)	Fx		Fy	
					RMS error	Percentage error	RMS error	Percentage error
1	2779.9	1576.6	12.4	42	1.48	6.20%	3.68	4.91%
2	2689.4	1652.7	12.8	38.7	4.32	7.95%	6.81	2.94%
3	2475.8	1414.6	18.7	47.1	3.02	5.63%	5.06	1.57%
4	3061.7	2257.7	14.1	51.2	0.34	3.72%	7.58	4.94%
5	3234.2	2011.9	13	56.1	2.71	8.80%	3.21	3.31%
6	3130.4	2246.1	14.9	56.2	0.58	4.71%	1.41	0.63%
7	2913.7	1796.9	17.2	61.6	0.51	9.08%	1.69	0.76%

The experimentally obtained cutting force coefficients variy as material and cutting conditions change. Researchers have discovered that cutting force coefficients are dependent of cutting conditions such as spindle speed, feedrate, axial depth of cut, and radial depth of cut. Cutting process and chip formation mechanics change with varying cutting speed, which leads to the change in cutting coefficients [112][113]. The accuracy of the predicted cutting force relies on the accuracy of the identified cutting force coefficients. However, the profound relationship between cutting conditions and cutting coefficients is out of the scope of this study. Usually,

cutting coefficients are identified for a set of cutting conditions and applied on other cutting conditions. For this study the average of the identified cutting coefficients was taken separately for stripe and meander AM parts (Table 22).

Table 22: Average cutting force coefficients.

	K_{tc} (N/mm^2)	K_{rc} (N/mm^2)	K_{te} (N/mm)	K_{re} (N/mm)
Stripe	2751.7	1725.4	14.5	44.8
Meander	3092.8	2018.3	15.0	58.0

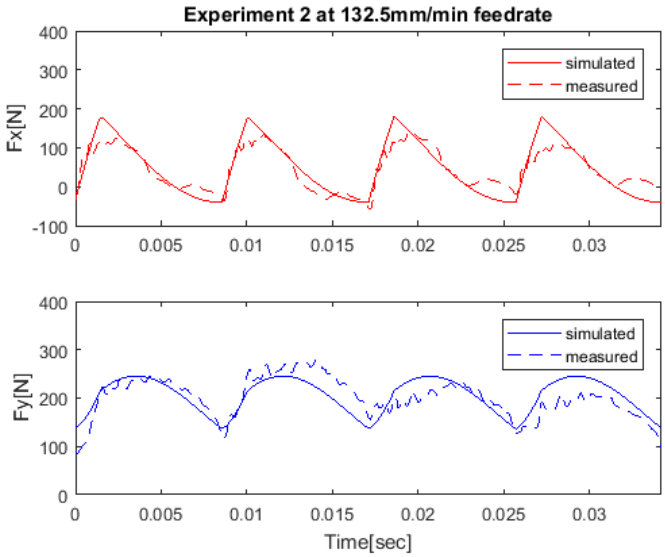

Figure 75: Half immersion down-milling.

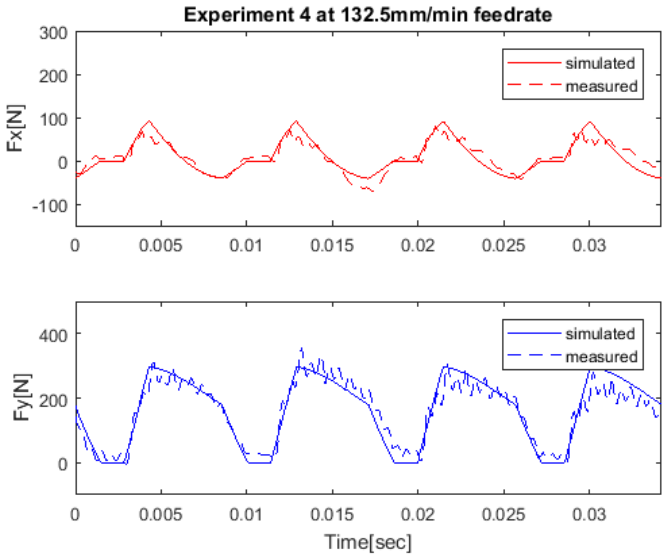

Figure 76: 1/4 immersion down-milling.

Table 21 as well as the figures displaying one cycle of the simulated and measured forces show that the simulated and measured cutting forces have good correlation in X and Y directions with an error less than 10% in the X direction and an error less than 5% in the Y direction. Data drifting occurred during data collection with the dynamometer which lead to inaccurate measurements. Also, since the average cutting force in Z direction is small, high percentage errors were observed in Z direction. As a result, simulated and measured forces comparison in Z direction was excluded.

5.2.2 Modal analysis

Eight modes are identified in each direction and the corresponding vibration parameters are summarized in Table 23 and Table 24. Some minor modes were neglected. The vibration parameters were identified using the method described in Section 5.1.2. Efforts were spent on tuning some of the vibration parameters against the measured FRF especially when modes are close to each other.

Table 23: Vibration modes in X direction.

Milling tool X				
Mode	Natural freq [Hz]	Damping ratio	Stiffness [N/m]	Mass [kg]
1	808	0.04	8.87E+07	3.4396
2	1017	0.05	4.18E+07	1.0247
3	1333	0.06	4.05E+07	0.5767
4	1696	0.045	5.61E+06	0.0494
5	1906	0.02	3.80E+07	0.2649
6	2216	0.05	8.33E+06	0.0430
7	4414	0.022	1.82E+07	0.0236
8	4911	0.03	5.29E+07	0.0556

Table 24: Vibration modes in Y direction.

Milling tool Y				
Mode	Natural freq [Hz]	Damping ratio	Stiffness [N/m]	Mass [kg]
1	766	0.02	2.55E+08	10.9903
2	977	0.05	8.13E+07	2.1575
3	1273	0.04	6.91E+07	1.0795
4	1707	0.06	6.08E+06	0.0529
5	1895	0.04	1.51E+07	0.1065
6	2240	0.07	6.74E+06	0.0340
7	4432	0.02	1.68E+07	0.0216
8	4941	0.05	2.75E+07	0.0286

Figure 77 and Figure 78 are the measured and synthesized receptance FRF plots in X and Y direction. One of the receptance was synthesized using the damping ratios (ζ_r) and the imaginary peaks of accelerance (Q_r) of the identified most significant modes. The other receptance was synthesized using the identified modal stiffness (k_r) and mass (m_r). Result show that the synthesized receptance FRFs match well with the measured FRF.

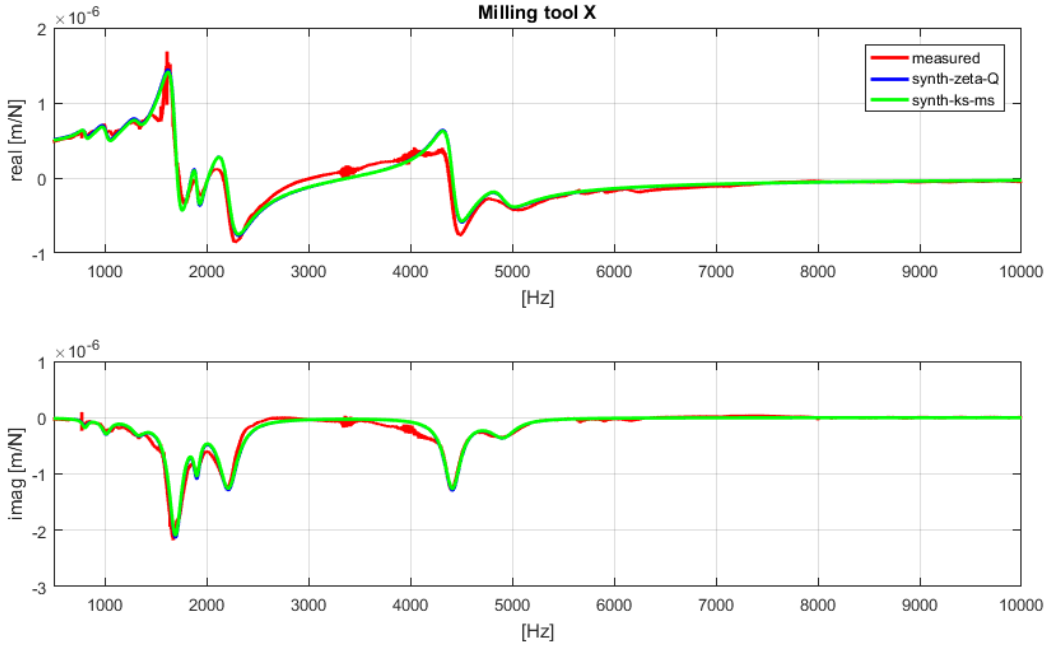

Figure 77: Measured and synthesized accelerance FRF in X direction.

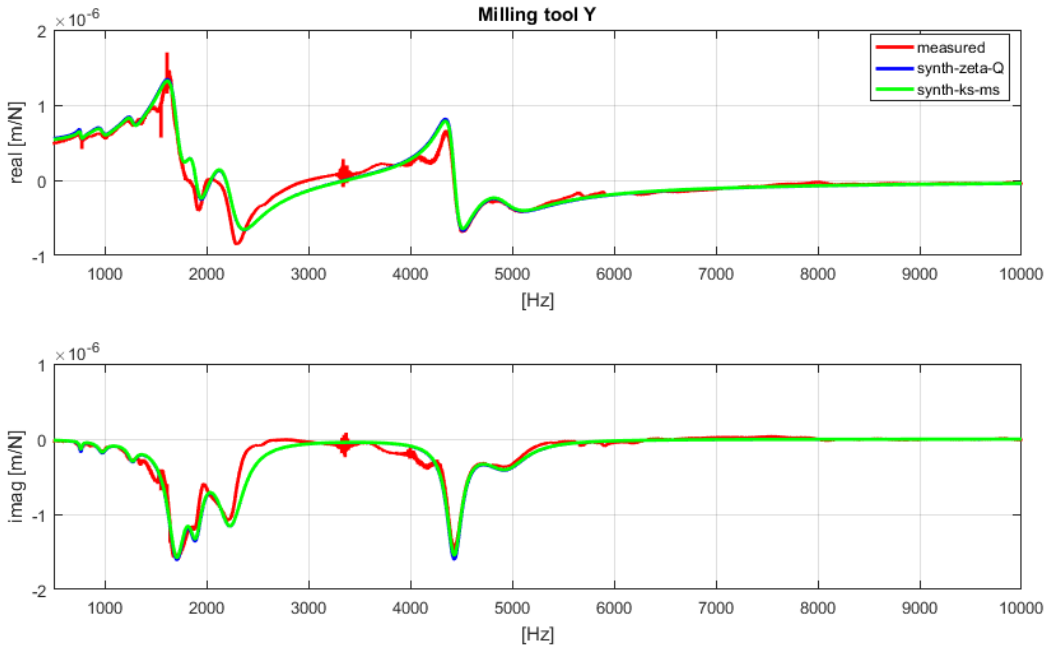

Figure 78: Measured and synthesized accelerance FRF in Y direction.

5.2.3 Chatter stability lobes of the milling cutter

Figure 79-Figure 81 are chatter stability lobes created for the 8 mm milling cutter given the identified cutting coefficients (Section 5.2.1) and vibration parameters (5.2.2) for ½ (4 mm), ¼ (2 mm), and 2.5% (0.2 mm) radial immersion down milling respectively. The axial depth of cut and spindle speed combinations which lie below the chatter stability lobes are considered stable. It can be observed that mode 4 (blue) with a natural frequency of about 1700 Hz and mode 7 (cyan) with a natural frequency of about 4400 Hz were the most significant modes which restrict the chatter free axial depth of cut. As radial immersion increases the allowable chatter free depth of cut increases given the same spindle speed from about 0.2 mm for ½ radial immersion down milling to about 2 mm for 2.5% radial immersion.

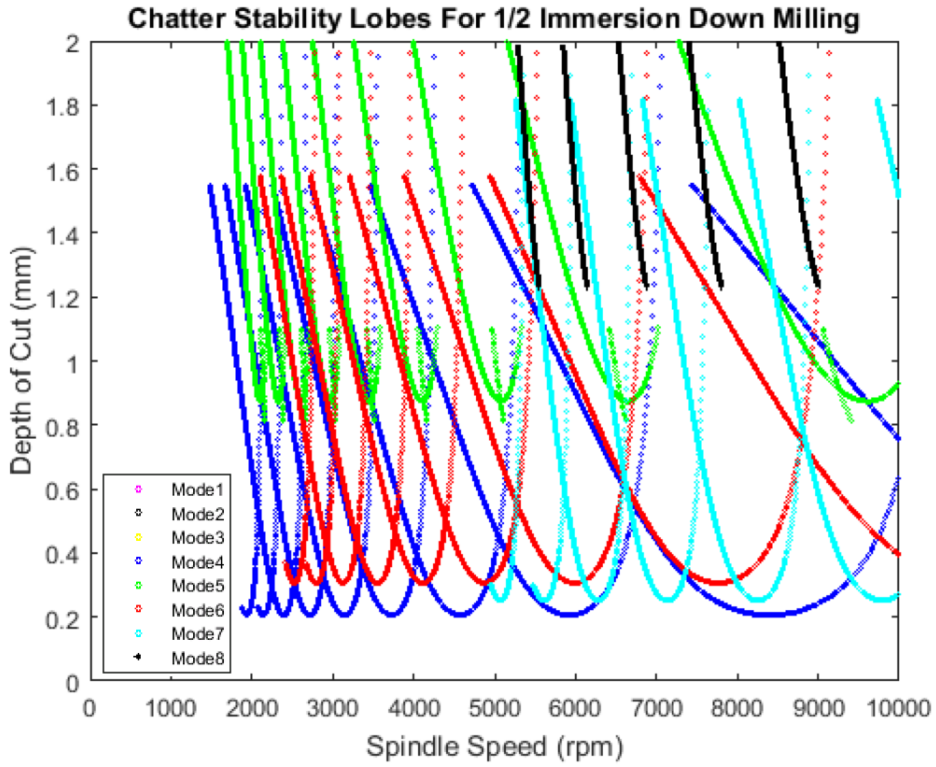

Figure 79: Chatter stability lobes for 1/2 radial immersion down milling.

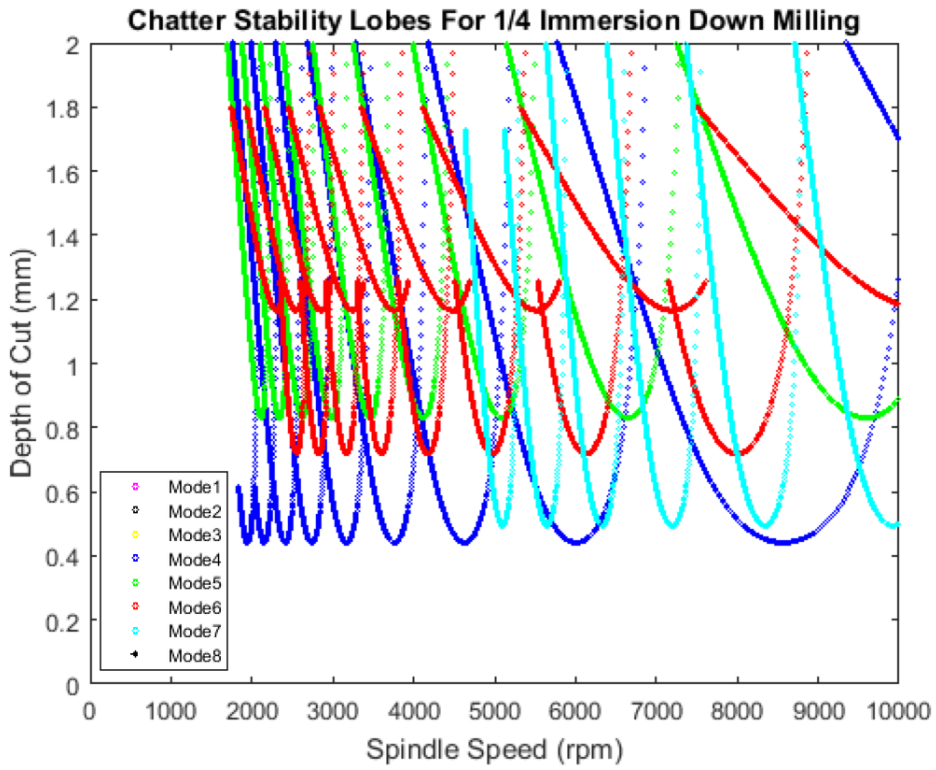

Figure 80: Chatter stability lobes for 1/4 radial immersion down milling.

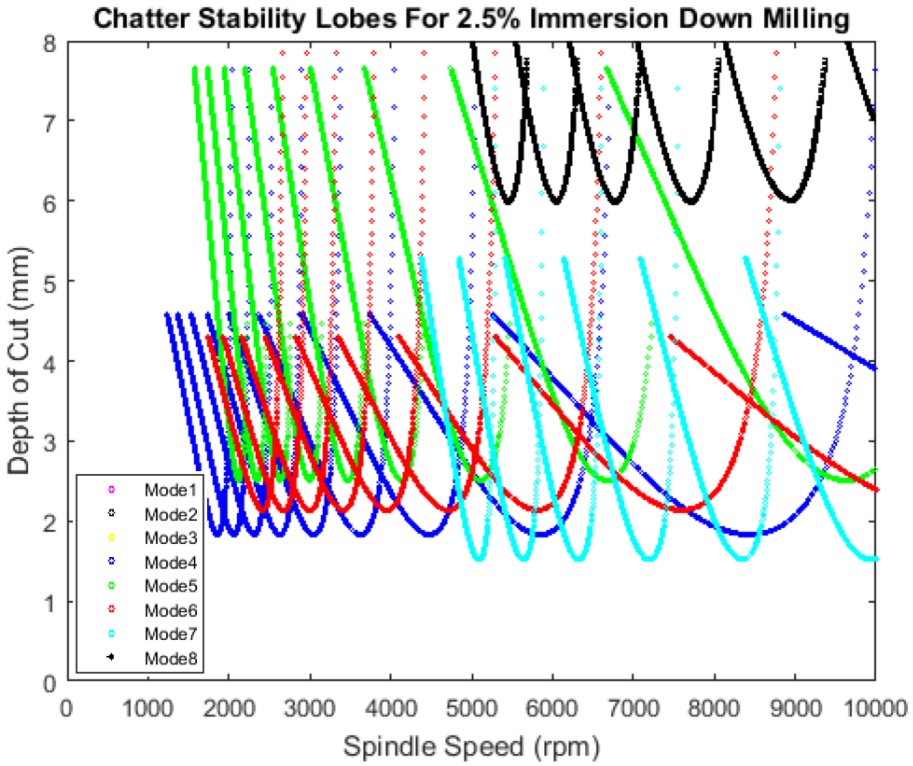

Figure 81: Chatter stability lobes for 2.5% radial immersion down milling.

5.2.4 Chatter stability lobes of the workpiece-fixture assemblies

Figure 82 displays FRFs obtained at four posts of the tracker with different fixturing methods. And Figure 83 shows the corresponding chatter stability analysis results. The blue FRFs (stand) were obtained when the tracker was constrained at the base only and all posts were unsupported. The red FRFs (fixture) were for the tracker and encapsulating fixture assembly and the green FRFs were for the tracker mounted with UV cured polymer. Results show that the encapsulating fixture has higher performance at location 1, 2 and 4 since it allows for a more aggressive axial depth of cut given the same spindle speed. The UV cured polymer solution performs better at location 3 since it used a printed plastic enclosure for the lower post. Although the encapsulating fixture performs better than the UV cured polymer method, there is a risk that fully enclosing the fixture would deform the part prior to machining as mentioned earlier. As a result, the printed plastic fixturing method may be more applicable to cases where the parts are not as flexible as the tracker or the tolerance requirement is not as strict as in this case. The lowest vibration mode occurs at 196 Hz when the tracker is constrained at the base only, as opposed to 1115 Hz when the encapsulating fixture was used. Both fixturing methods improve the stiffness of the tracker with the fixtures provide on average an order of magnitude increase in the permissible depth of cut.

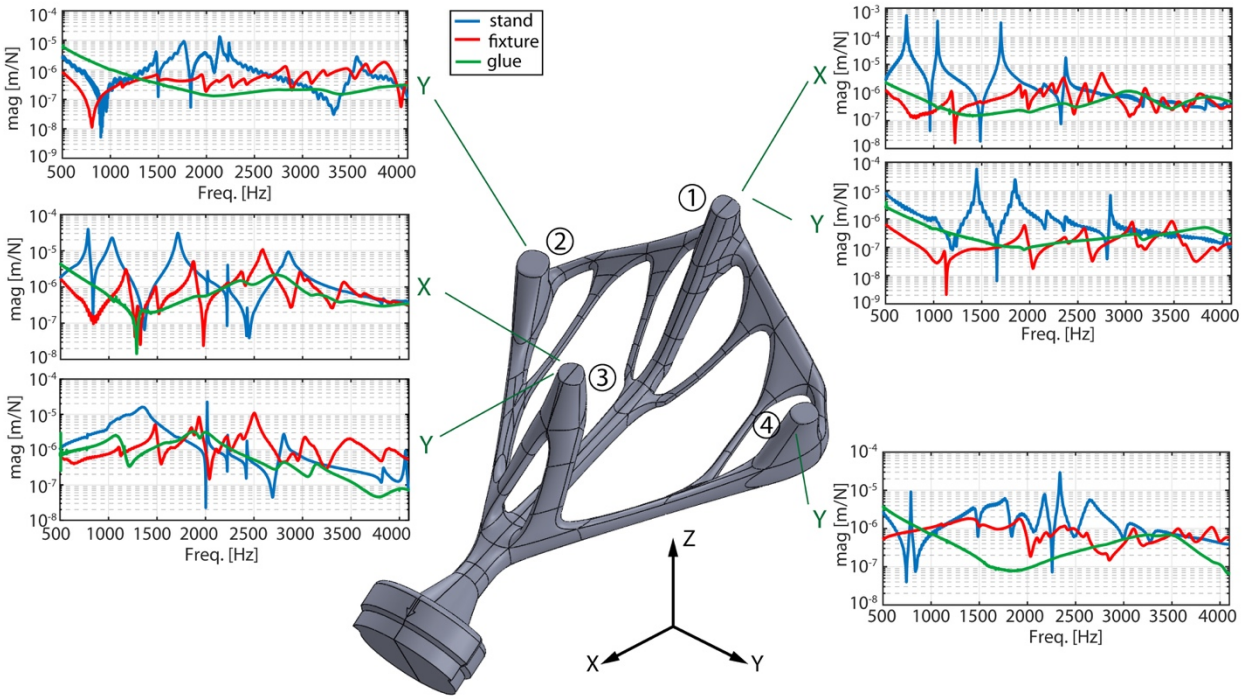

Figure 82: FRFs obtained at four posts.

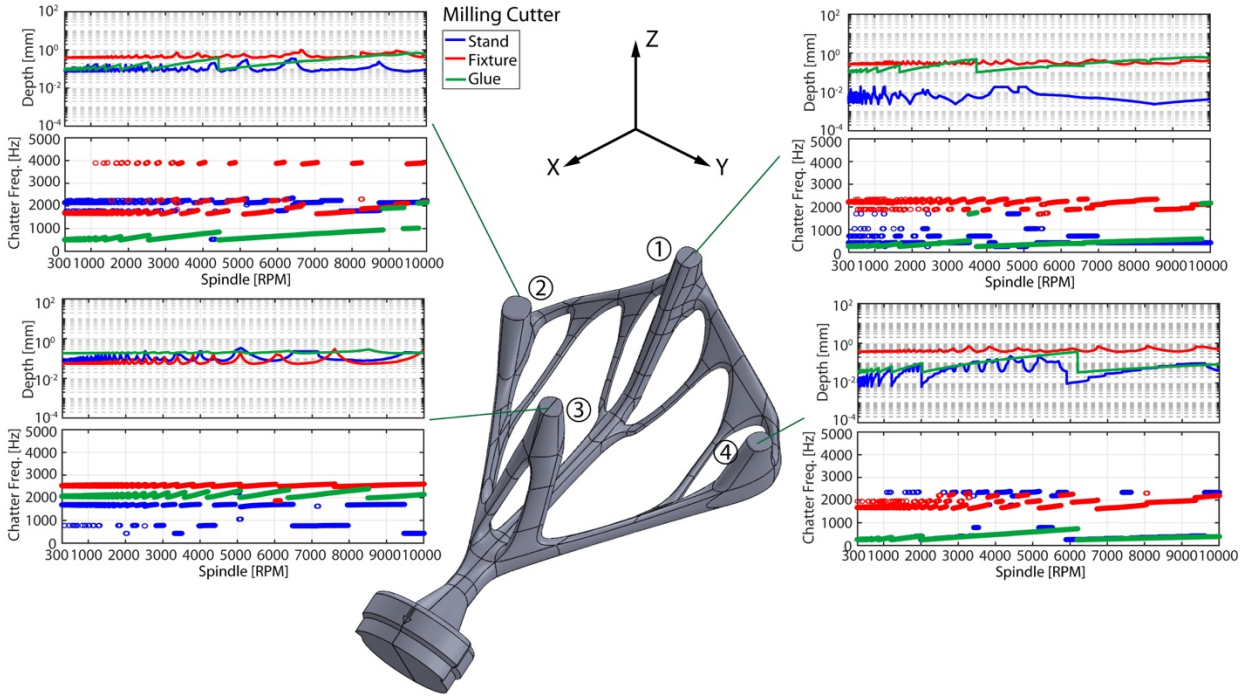

Figure 83: Tracker posts chatter stability.

Chapter 6

Deployment of Additive Manufacturing and Post-Processing Machining

The fabrication and inspection processes were done in collaboration with Renishaw Canada Solutions Centre, with the assistance of Mr. Mark Kirby, Additive Manufacturing Business Manager and Mr. Carl Hamann, Solution Centre Manager.

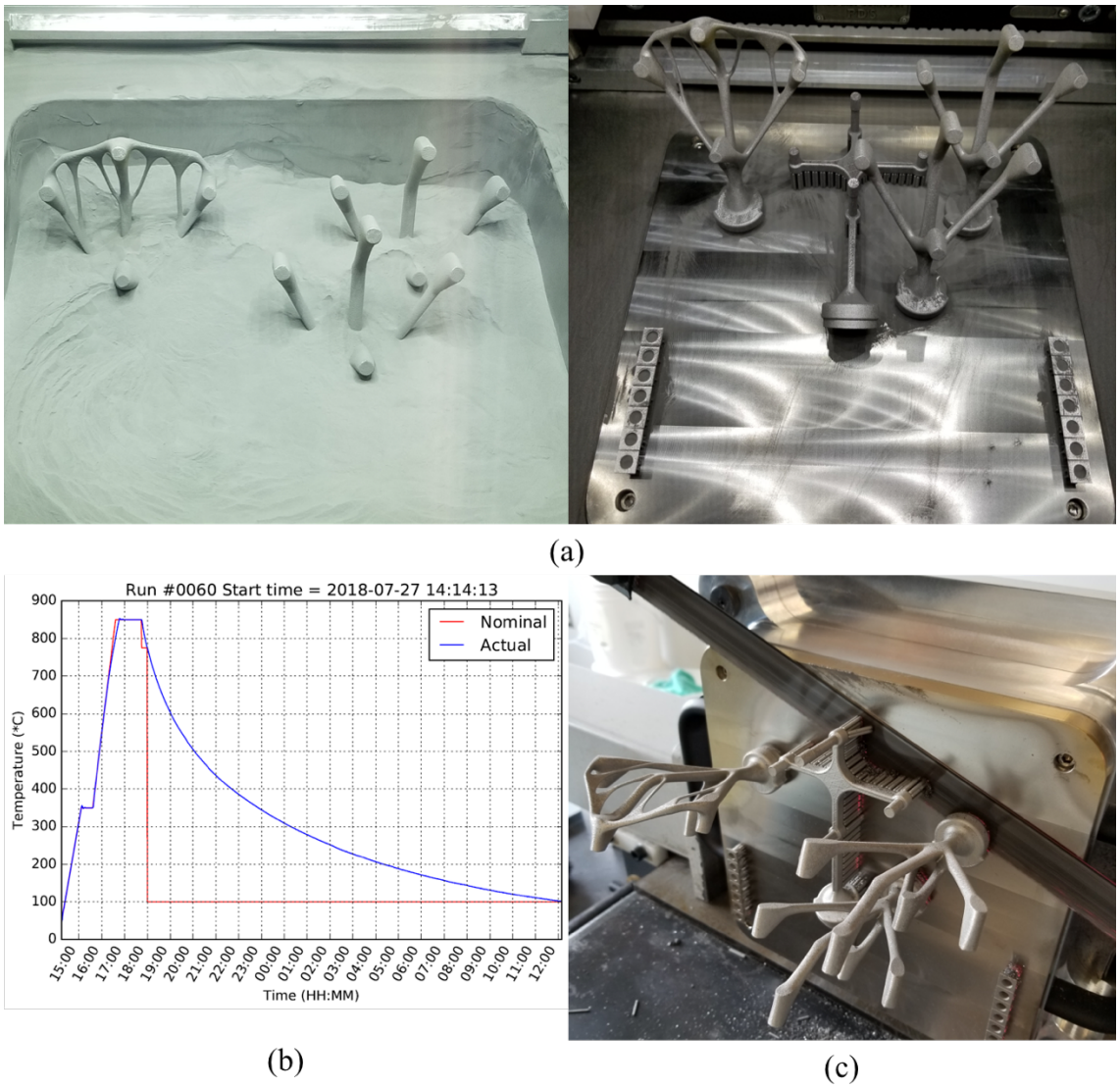

Figure 84: Post-processing of the trackers: (a) powder removal; (b) heat treatment temperature curve, (c) part removal from build plate and support structure removal.

As mentioned the earlier, the trackers were printed on the AM 400 LPBF machine with QuantAM's default recipe "Ti6Al4V_200_1112_08_30um_stripe" (Table 6). Figure 84 shows post-processing steps after the fabrication of the trackers via LPBF and before the machining process. After the removal of excessive powder, the build plate with the trackers attached to it were heat treated for the relief of residual stress. During heat treatment, the temperature was gradually increased to 850°C and was held at 850°C for about an hour. Then the parts were left to cool down to 100°C; the heat treatment is shown also in Figure 84 (b). Next, the trackers were cut off from the build plate by a band saw and support structures were removed as well. The trackers were sand blasted to clear up the uneven surface where the support structures were originally attached. A matte surface finish was left on the tracker after sand blasting which is intended for a non-reflective tracker body during operation in an optical navigation system.

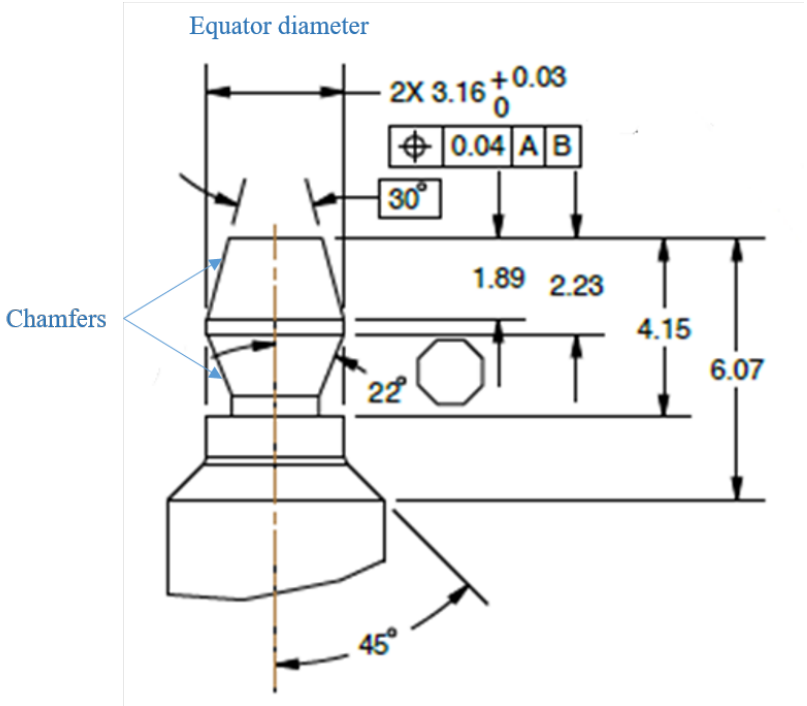

Figure 85: detailed drawing of the tracker post.

The two Cobra trackers were machined with one of the tracker being mounted on the CNC machine with the ABS encapsulating fixture and the other one being fixed by UV cured polymer. Positioning of the part on the CNC machining was done by applying Renishaw's "multi-point" probing alignment method as mentioned in Section 2.3.2. Theoretically, minimum of 6 points were required to determine the 'best-fit' alignment between the workpiece axis and the machine axis with three point to determine the top plane, one point to constraint the X transition, one point to constraint the Y transition, and the last point to constraint the Z axis rotation. Figure 85 is a detailed drawing of the tracker post. Machining planning was done in Fusion 360 by AutoDesk®. An 8 mm milling tool was used to rough (with 0.2 mm radial depth of cut) the equator diameter of the post to leave 0.1 mm stock material from the targeted diameter. Detailed machining parameters were shown on Figure 86. The posts were then machined to reach the targeted diameter with the same cutter. Lastly, a 12.07 mm diameter form tool was used to produce the chamfer form above and beneath the equator. In all cases the tools were cutting at about 5 mm depth of cut which is the height of the equator. It should be aware that the actual machining process was done before the chatter stability analysis of the cutter and the workpiece was conducted. According to the chatter stability lobe of the cutter (Section 5.2.3), for 2.5% radial immersion (equivalent to 0.2 mm radial depth of cut) down milling, chatter free axial depth of cut should be smaller than 2 mm for the selected spindle speed of 4890 rpm. This indicates that chatter may have occurred during the roughing process. If the synergy process workflow is to be repeated for next design iterations, chatter stability analysis should be done to determine chatter free depth of cut and spindle speed prior to the machining process as if the workflow is followed correctly step by step.

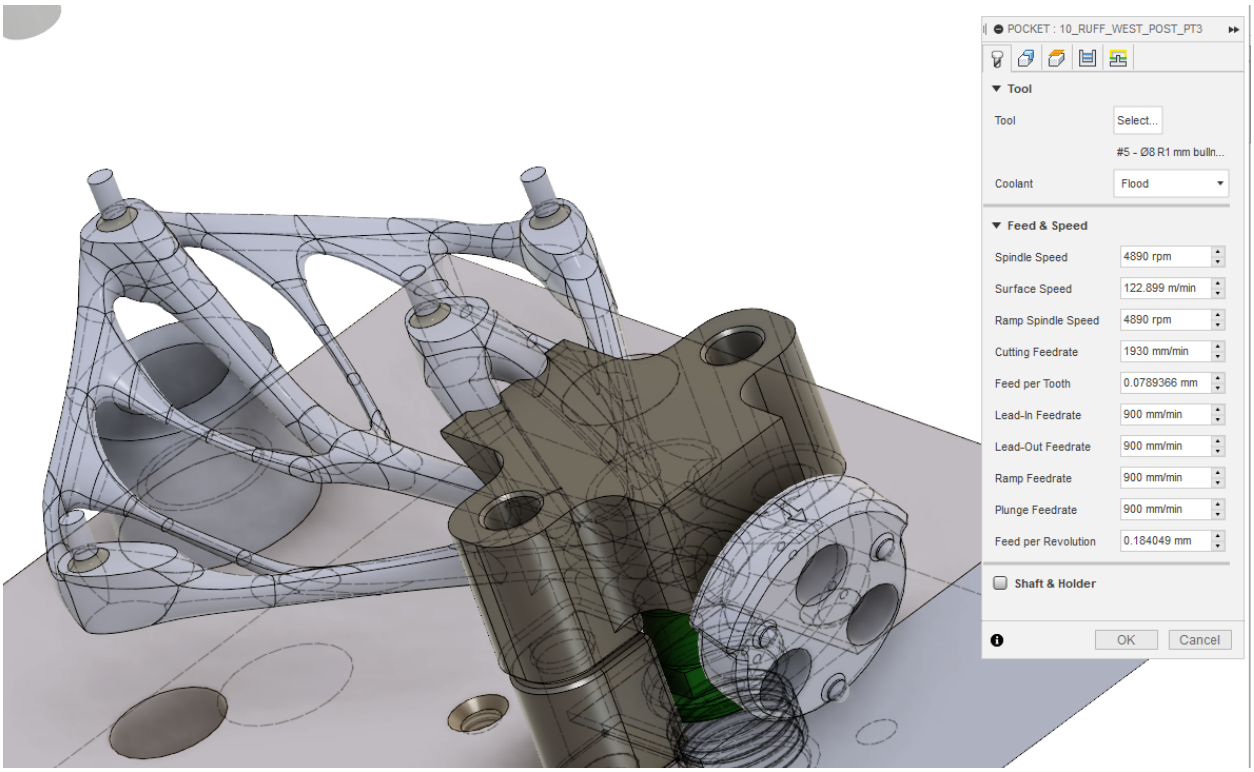

Figure 86: Roughing parameters.

Figure 87 were two machined Cobra trackers in the corresponding fixtures. Inspection results indicate that the clamping force of the ABS encapsulating fixture deformed the tracker prior to machining. The upper post was out of tolerance after the tracker being released from the fixture. For the UV cured polymer fixturing solution, the lower post experienced severe vibration because it was supported initially due to the accessibility of the UV device to the lower post. A plastic mold was printed to constrain and stiffen the lower post as shown on the right image of Figure 87. The plastic enclosure added to the lower post was able to dampen out the vibration.

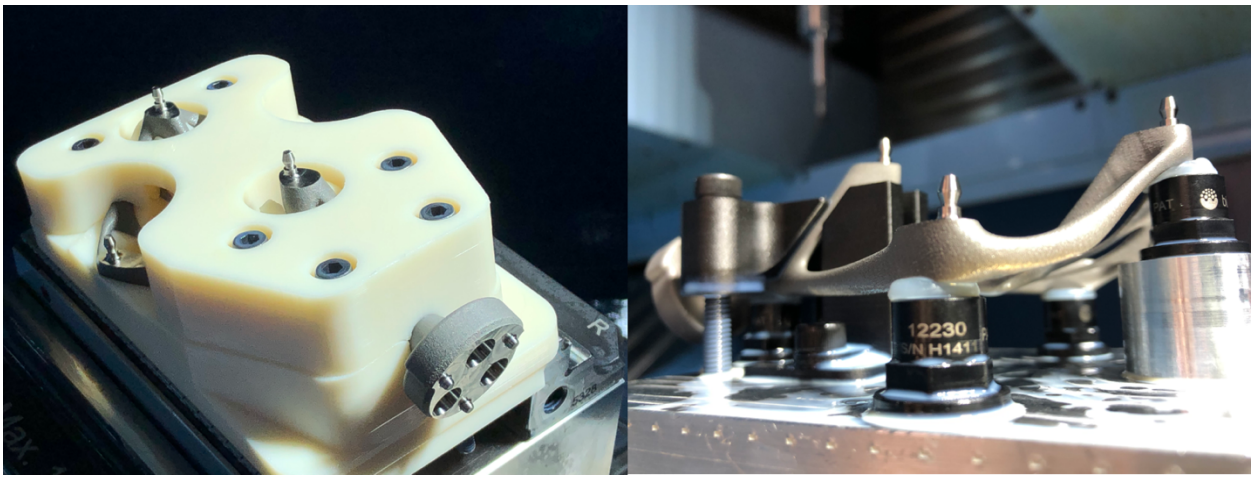

Figure 87: Machined Cobra tracker.

Chapter 7

Conclusions and Future Work

7.1 Summary and conclusions

In this thesis, a workflow which synergizes the AM and post-machining processes has been proposed and deployed in a case study of manufacturing a surgical tool using LPBF followed by post-machining. Using AM, the original tracker assembly was consolidated into one piece so that the high part rejection rate due to dimensional inaccuracy accumulation and tolerance violation during the assembly process. By post-machining of the mating surfaces, surface roughness was reduced and dimensional inaccuracy due to geometric distortion was corrected to fulfil functional requirements. Key findings and future work in regarding the synergy process are as follows:

1) The magnitude of surface roughness was reduced from the order of between 10^0 and 10^1 μm which is typical for an as-printed surface to the order of 10^{-1} μm by machining.
2) Dimensional and positional accuracy of the printed part was improved by post-machining. For instance, the maximum distortion of the ET tracker of 1.5 mm was reduced to be within tolerance by post-machining the reserved machining allowance.
3) Geometric distortion was geometric dependent. The Cobra design with interconnecting posts distorted less compared to the ET design with free posts.
4) Design space, load cases, minimal filter radius, manufacturing constraints can all effect the result of structural topology optimization. The most suitable design should be selected among all candidates considering functional and manufacturing requirements.
5) In this study, the distortion simulation tended to underestimate the actual distortion of the tracker. An accurate simulation of the AM process involved multi-scale physics for

example, laser powder interaction, layer hatching and macro part build up. Simulation accuracy is still limited by computational cost.

6) Unit cost, thermal induced distortion, and support structures were reduced through build orientation optimization.
7) Work holding of complex AM parts is challenging. The encapsulating fixture provided good stiffness and damping to the tracker during machining, but the flexible tracker was pre-deformed under clamping force. The UV system addressed the pre-deformation issue. However, accessibility of the UV device to some regions of the part was prohibited.
8) Cutting coefficients vary as cutting conditions change. Since accurate identification of cutting coefficients is fundamental to reliable cutting force prediction, chatter stability analysis and surface quality simulation, the relationship between cutting force coefficients and cutting conditions need to be studied. For AM materials, cutting force coefficients may also vary as AM parameters and part properties change.
9) Instead of performing chatter stability analysis on the cutter only, the vibratory behavior of the AM part need to be included in the chatter free machining parameter planning as AM parts usually contains thin-wall structures.

Bibliography

[1] F42 Committee, “Terminology for Additive Manufacturing Technologies,” ASTM International.

[2] V. Petrovic, J. Vicente Haro Gonzalez, O. Jordá Ferrando, J. Delgado Gordillo, J. Ramón Blasco Puchades, and L. Portolés Griñan, “Additive layered manufacturing: sectors of industrial application shown through case studies,” *Int. J. Prod. Res.*, vol. 49, no. 4, pp. 1061–1079, Feb. 2011.

[3] D. Ding, Z. Pan, D. Cuiuri, and H. Li, “Wire-feed additive manufacturing of metal components: technologies, developments and future interests,” *Int. J. Adv. Manuf. Technol.*, vol. 81, no. 1–4, pp. 465–481, Oct. 2015.

[4] W. E. King *et al.*, “Laser powder bed fusion additive manufacturing of metals; physics, computational, and materials challenges,” *Appl. Phys. Rev.*, vol. 2, no. 4, p. 041304, Dec. 2015.

[5] V. Bhavar, P. Kattire, V. Patil, S. Khot, K. Gujar, and R. Singh, “A Review on Powder Bed Fusion Technology of Metal Additive Manufacturing,” p. 8.

[6] “Transforming the supply chain with additive manufacturing | Deloitte Insights.” [Online]. Available: https://www2.deloitte.com/insights/us/en/focus/3d-opportunity/additive-manufacturing-3d-printing-supply-chain-transformation.html. [Accessed: 29-Jan-2019].

[7] S. Ford and M. Despeisse, “Additive manufacturing and sustainability: an exploratory study of the advantages and challenges,” *J. Clean. Prod.*, vol. 137, pp. 1573–1587, Nov. 2016.

[8] S. H. Huang, P. Liu, A. Mokasdar, and L. Hou, "Additive manufacturing and its societal impact: a literature review," *Int. J. Adv. Manuf. Technol.*, vol. 67, no. 5–8, pp. 1191–1203, Jul. 2013.

[9] J. Liu, "Guidelines for AM part consolidation," *Virtual Phys. Prototyp.*, vol. 11, no. 2, pp. 133–141, Apr. 2016.

[10] J. Schmelzle, E. V. Kline, C. J. Dickman, E. W. Reutzel, G. Jones, and T. W. Simpson, "(Re)Designing for Part Consolidation: Understanding the Challenges of Metal Additive Manufacturing," *J. Mech. Des.*, vol. 137, no. 11, p. 111404, Oct. 2015.

[11] S. Yang, Y. Tang, and Y. F. Zhao, "A new part consolidation method to embrace the design freedom of additive manufacturing," *J. Manuf. Process.*, vol. 20, pp. 444–449, Oct. 2015.

[12] D. W. Rosen, "Computer-Aided Design for Additive Manufacturing of Cellular Structures," *Comput.-Aided Des. Appl.*, vol. 4, no. 5, pp. 585–594, Jan. 2007.

[13] L. E. Murr *et al.*, "Metal Fabrication by Additive Manufacturing Using Laser and Electron Beam Melting Technologies," *J. Mater. Sci. Technol.*, vol. 28, no. 1, pp. 1–14, Jan. 2012.

[14] L. E. Murr *et al.*, "Next-generation biomedical implants using additive manufacturing of complex, cellular and functional mesh arrays," *Philos. Trans. R. Soc. Math. Phys. Eng. Sci.*, vol. 368, no. 1917, pp. 1999–2032, Apr. 2010.

[15] T. Zegard and G. H. Paulino, "Bridging topology optimization and additive manufacturing," *Struct. Multidiscip. Optim.*, vol. 53, no. 1, pp. 175–192, Jan. 2016.

[16] D. Brackett, I. Ashcroft, and R. Hague, “TOPOLOGY OPTIMIZATION FOR ADDITIVE MANUFACTURING,” p. 15.

[17] M. Langelaar, “Topology optimization of 3D self-supporting structures for additive manufacturing,” *Addit. Manuf.*, vol. 12, pp. 60–70, Oct. 2016.

[18] A. T. Gaynor and J. K. Guest, “Topology optimization considering overhang constraints: Eliminating sacrificial support material in additive manufacturing through design,” *Struct. Multidiscip. Optim.*, vol. 54, no. 5, pp. 1157–1172, Nov. 2016.

[19] M. Langelaar, “An additive manufacturing filter for topology optimization of print-ready designs,” *Struct. Multidiscip. Optim.*, vol. 55, no. 3, pp. 871–883, Mar. 2017.

[20] X. Su, Y. Yang, P. Yu, and J. Sun, “Development of porous medical implant scaffolds via laser additive manufacturing,” *Trans. Nonferrous Met. Soc. China*, vol. 22, pp. s181–s187, Oct. 2012.

[21] C. J. Tuck, R. J. M. Hague, M. Ruffo, M. Ransley, and P. Adams, “Rapid manufacturing facilitated customization,” *Int. J. Comput. Integr. Manuf.*, vol. 21, no. 3, pp. 245–258, Apr. 2008.

[22] J. H. P. Pallari, K. W. Dalgarno, J. Munguia, L. Muraru, L. Peeraer, and S. Telfer, “DESIGN AND ADDITIVE FABRICATION OF FOOT AND ANKLE-FOOT ORTHOSES,” p. 12.

[23] B. Vayre, F. Vignat, and F. Villeneuve, “Designing for Additive Manufacturing,” *Procedia CIRP*, vol. 3, pp. 632–637, 2012.

[24] “Why GM’s Electric Future Is Also an Additive Future.” [Online]. Available: https://www.additivemanufacturing.media/articles/why-gms-electric-future-is-also-an-additive-future. [Accessed: 30-Jan-2019].

[25] S. Goehrke, “Additive Manufacturing Is Driving The Future Of The Automotive Industry,” *Forbes*. [Online]. Available: https://www.forbes.com/sites/sarahgoehrke/2018/12/05/additive-manufacturing-is-driving-the-future-of-the-automotive-industry/. [Accessed: 30-Jan-2019].

[26] “datastream.pdf.” .

[27] S. W. Williams, F. Martina, A. C. Addison, J. Ding, G. Pardal, and P. Colegrove, “Wire + Arc Additive Manufacturing,” *Mater. Sci. Technol.*, vol. 32, no. 7, pp. 641–647, May 2016.

[28] M. Vaezi and S. Yang, “Extrusion-based additive manufacturing of PEEK for biomedical applications,” *Virtual Phys. Prototyp.*, vol. 10, no. 3, pp. 123–135, Jul. 2015.

[29] J. Parthasarathy, B. Starly, and S. Raman, “A design for the additive manufacture of functionally graded porous structures with tailored mechanical properties for biomedical applications,” *J. Manuf. Process.*, vol. 13, no. 2, pp. 160–170, Aug. 2011.

[30] T. Kellner, “How 3D Printing Is Changing Aerospace Manufacturing,” *GE Reports*, 10-Jul-2017. [Online]. Available: https://www.ge.com/reports/mind-meld-ge-3d-printing-visionary-joined-forces/. [Accessed: 11-Feb-2019].

[31] “Article - Optimized Design Yields Complex Bracket | 3D Metal Printing Magazine.” [Online]. Available:

https://www.3dmpmag.com/magazine/article/Default.asp?/2017/2/10/Optimized_Design_Yields_Complex_Bracket. [Accessed: 11-Feb-2019].

[32] "GM and Autodesk are using generative design for vehicles of the future," *3D Printing Progress*, 08-May-2018. [Online]. Available: https://www.3dprintingprogress.com/articles/14248/gm-and-autodesk-are-using-generative-design-for-vehicles-of-the-future. [Accessed: 11-Feb-2019].

[33] "ADDITIVE METAL MANUFACTURING wants to make you more competitive," *Canadian Plastics*. [Online]. Available: https://www.canplastics.com/features/additive-metal-manufacturing-wants-to-make-you-more-competitive/. [Accessed: 11-Feb-2019].

[34] M. P. Bendsøe and O. Sigmund, "Material interpolation schemes in topology optimization," *Arch. Appl. Mech. Ing. Arch.*, vol. 69, no. 9–10, pp. 635–654, Nov. 1999.

[35] E. L. Cardoso and J. S. O. Fonseca, "Complexity control in the topology optimization of continuum structures," *J. Braz. Soc. Mech. Sci. Eng.*, vol. 25, no. 3, pp. 293–301, Sep. 2003.

[36] J. Koga, J. Koga, and S. Homma, "CHECKERBOARD PROBLEM TO TOPOLOGY OPTIMIZATIO OF CO TI UUM STRUCTURES," p. 10.

[37] X. Huang and Y. M. Xie, "Convergent and mesh-independent solutions for the bi-directional evolutionary structural optimization method," *Finite Elem. Anal. Des.*, vol. 43, no. 14, pp. 1039–1049, Oct. 2007.

[38] K. Suzuki and N. Kikuchi, "A homogenization method for shape and topology optimization," *Comput. Methods Appl. Mech. Eng.*, vol. 93, no. 3, pp. 291–318, Dec. 1991.

[39] P. Hajela and E. Lee, “Genetic algorithms in truss topological optimization,” *Int. J. Solids Struct.*, vol. 32, no. 22, pp. 3341–3357, Nov. 1995.

[40] M. Y. Wang, X. Wang, and D. Guo, “A level set method for structural topology optimization,” *Comput. Methods Appl. Mech. Eng.*, vol. 192, no. 1–2, pp. 227–246, Jan. 2003.

[41] A. Aremu, I. Ashcroft, R. Wildman, R. Hague, C. Tuck, and D. Brackett, “The effects of bidirectional evolutionary structural optimization parameters on an industrial designed component for additive manufacture,” *Proc. Inst. Mech. Eng. Part B J. Eng. Manuf.*, vol. 227, no. 6, pp. 794–807, Jun. 2013.

[42] M. Langelaar, “Topology optimization of 3D self-supporting structures for additive manufacturing,” *Addit. Manuf.*, vol. 12, pp. 60–70, Oct. 2016.

[43] G. Manogharan, R. Wysk, O. Harrysson, and R. Aman, “AIMS – A Metal Additive-hybrid Manufacturing System: System Architecture and Attributes,” *Procedia Manuf.*, vol. 1, pp. 273–286, 2015.

[44] K. Mumtaz and N. Hopkinson, “Top surface and side roughness of Inconel 625 parts processed using selective laser melting,” *Rapid Prototyp. J.*, vol. 15, no. 2, pp. 96–103, Mar. 2009.

[45] J. C. Fox, S. P. Moylan, and B. M. Lane, “Effect of Process Parameters on the Surface Roughness of Overhanging Structures in Laser Powder Bed Fusion Additive Manufacturing,” *Procedia CIRP*, vol. 45, pp. 131–134, 2016.

[46] M. Jamshidinia and R. Kovacevic, “The influence of heat accumulation on the surface roughness in powder-bed additive manufacturing,” *Surf. Topogr. Metrol. Prop.*, vol. 3, no. 1, p. 014003, Feb. 2015.

[47] H. Gong, K. Rafi, H. Gu, T. Starr, and B. Stucker, “Analysis of defect generation in Ti–6Al–4V parts made using powder bed fusion additive manufacturing processes,” *Addit. Manuf.*, vol. 1–4, pp. 87–98, Oct. 2014.

[48] T. M. Mower and M. J. Long, “Mechanical behavior of additive manufactured, powder-bed laser-fused materials,” *Mater. Sci. Eng. A*, vol. 651, pp. 198–213, Jan. 2016.

[49] H. Gong, K. Rafi, H. Gu, G. D. Janaki Ram, T. Starr, and B. Stucker, “Influence of defects on mechanical properties of Ti–6Al–4V components produced by selective laser melting and electron beam melting,” *Mater. Des.*, vol. 86, pp. 545–554, Dec. 2015.

[50] H. Gong, K. Rafi, T. Starr, and B. Stucker, “EFFECT OF DEFECTS ON FATIGUE TESTS OF AS-BUILT TI-6AL-4V PARTS FABRICATED BY SELECTIVE LASER MELTING,” p. 8.

[51] “Additive manufacturing of fatigue resistant materials: Challenges and opportunities.” [Online]. Available: https://reader.elsevier.com/reader/sd/pii/S0142112317300014?token=EDD3C14EA96D526CC668A399A00BAF8EFB76316E191EE4E25754A4342E4009B3A2CBDA8C65495CD2F34BFE9D198319C9. [Accessed: 11-Feb-2019].

[52] W. E. Frazier, “Metal Additive Manufacturing: A Review,” *J. Mater. Eng. Perform.*, vol. 23, no. 6, pp. 1917–1928, Jun. 2014.

[53] T. Niendorf, S. Leuders, A. Riemer, H. A. Richard, T. Tröster, and D. Schwarze, “Highly Anisotropic Steel Processed by Selective Laser Melting,” *Metall. Mater. Trans. B*, vol. 44, no. 4, pp. 794–796, Aug. 2013.

[54] R. Paul, S. Anand, and F. Gerner, “Effect of Thermal Deformation on Part Errors in Metal Powder Based Additive Manufacturing Processes,” *J. Manuf. Sci. Eng.*, vol. 136, no. 3, p. 031009, Mar. 2014.

[55] “Additive manufacturing of metallic components â€“ Process, structure and properties.” [Online]. Available: https://reader.elsevier.com/reader/sd/pii/S0079642517301172?token=6F110B92118F22CC6DE2AD5463AE5B91F42FCDE9F1ECBC8C665D02ED35EE86C31FA7563AB7EBD8417898EA4E06251943. [Accessed: 11-Feb-2019].

[56] W. Xu *et al.*, “Additive manufacturing of strong and ductile Ti–6Al–4V by selective laser melting via in situ martensite decomposition,” *Acta Mater.*, vol. 85, pp. 74–84, Feb. 2015.

[57] X. Zhao, X. Lin, J. Chen, L. Xue, and W. Huang, “The effect of hot isostatic pressing on crack healing, microstructure, mechanical properties of Rene88DT superalloy prepared by laser solid forming,” *Mater. Sci. Eng. A*, vol. 504, no. 1–2, pp. 129–134, Mar. 2009.

[58] S. Tammas-Williams, P. J. Withers, I. Todd, and P. B. Prangnell, “The Effectiveness of Hot Isostatic Pressing for Closing Porosity in Titanium Parts Manufactured by Selective Electron Beam Melting,” *Metall. Mater. Trans. A*, vol. 47, no. 5, pp. 1939–1946, May 2016.

[59] D. Wang, Y. Yang, Z. Yi, and X. Su, “Research on the fabricating quality optimization of the overhanging surface in SLM process,” *Int. J. Adv. Manuf. Technol.*, vol. 65, no. 9–12, pp. 1471–1484, Apr. 2013.

[60] R. plc, “Renishaw: Design for metal AM - a beginner’s guide,” *Renishaw*. [Online]. Available: http://www.renishaw.com/en/design-for-metal-am-a-beginners-guide--42652. [Accessed: 13-Feb-2019].

[61] R. plc, “Renishaw: RenAM 500Q,” *Renishaw*. [Online]. Available: http://www.renishaw.com/en/renam-500q--42781. [Accessed: 07-Feb-2019].

[62] “EOS 400-4: Ultra-fast quad-laser system for industrial 3D printing.” [Online]. Available: https://www.eos.info/systems_solutions/eos-m-400-4. [Accessed: 07-Feb-2019].

[63] M. U. Fahad and N. Hopkinson, “A new benchmarking part for evaluating the accuracy and repeatability of Additive Manufacturing (AM) processes.”

[64] W. Gao *et al.*, “The status, challenges, and future of additive manufacturing in engineering,” *Comput.-Aided Des.*, vol. 69, pp. 65–89, Dec. 2015.

[65] “Additive manufacturing applications in medical cases: A literature based review.” [Online]. Available: https://reader.elsevier.com/reader/sd/pii/S2090506817302282?token=75CACA3881F8EA5DA8F2BF7CEF0C57A1CB69F0EA0147A721045D3DB84BBCC1CD0890EC5EAD6AA175AC1BEA2F0830D053. [Accessed: 30-Jan-2019].

[66] G. Manivasagam, D. Dhinasekaran, and A. Rajamanickam, “Biomedical Implants: Corrosion and its Prevention - A Review~!2009-12-22~!2010-01-20~!2010-05-25~!,” *Recent Pat. Corros. Sci.*, vol. 2, no. 1, pp. 40–54, Jun. 2010.

[67] J. Tuomi *et al.*, "A Novel Classification and Online Platform for Planning and Documentation of Medical Applications of Additive Manufacturing," *Surg. Innov.*, vol. 21, no. 6, pp. 553–559, Dec. 2014.

[68] M. Salmi *et al.*, "Patient-specific reconstruction with 3D modeling and DMLS additive manufacturing," *Rapid Prototyp. J.*, vol. 18, no. 3, pp. 209–214, Apr. 2012.

[69] D. Wang, Y. Wang, J. Yu, Y. Yang, and C. Song, "Personalized femoral component design and its direct manufacturing by selective laser melting," *Rapid Prototyp. J.*, vol. 22, no. 2, pp. 330–337, Mar. 2016.

[70] X. Wang *et al.*, "Topological design and additive manufacturing of porous metals for bone scaffolds and orthopaedic implants: A review," *Biomaterials*, vol. 83, pp. 127–141, Mar. 2016.

[71] Z. Linxi, Y. Quanzhan, Z. Guirong, Z. Fangxin, S. Gang, and Y. Bo, "Additive manufacturing technologies of porous metal implants," p. 10, 2014.

[72] "3D Printed Surgical Tool Inspired By Origami," *All3DP*, 06-Apr-2016. [Online]. Available: https://all3dp.com/3d-printed-surgical-tool-inspired-origami/. [Accessed: 20-Mar-2019].

[73] "New 3D Printed Medical Tool a Breakthrough for ACL Reconstruction Surgery," *3D Printing Industry*, 08-Jan-2016. [Online]. Available: https://3dprintingindustry.com/news/new-3d-printed-surgical-tool-a-breakthrough-for-acl-reconstruction-surgery-64519/. [Accessed: 20-Mar-2019].

[74] “CIRP.” [Online]. Available: https://www.cirp.net/component/cirppubli/?task=searchpublic&year=2011. [Accessed: 08-Feb-2019].

[75] Z. Zhu, V. G. Dhokia, A. Nassehi, and S. T. Newman, “A review of hybrid manufacturing processes – state of the art and future perspectives,” *Int. J. Comput. Integr. Manuf.*, vol. 26, no. 7, pp. 596–615, Jul. 2013.

[76] “LASERTEC 65 3D hybrid - ADDITIVE MANUFACTURING Machines by DMG MORI.” [Online]. Available: https://en.dmgmori.com/products/machines/additive-manufacturing/powder-nozzle/lasertec-65-3d-hybrid. [Accessed: 11-Feb-2019].

[77] “New Mazak VC-500 AM Combines 5-Axis and Additive Technology to Revolutionize Product Design.” [Online]. Available: https://www.mazakusa.com/news-events/news-releases/new-mazak-vc-500-am-combines-5-axis-and-additive-technology/. [Accessed: 11-Feb-2019].

[78] Sodick, “OPM250L - Metal 3D Printer,” *Sodick*, 10-Feb-2019. [Online]. Available: //www.sodick.com/products/metal-3d-printing/opm250l. [Accessed: 11-Feb-2019].

[79] K. Boivie, R. Karlsen, and P. Ystgaard, “THE CONCEPT OF HYBRID MANUFACTURING FOR HIGH PERFORMANCE PARTS#,” *South Afr. J. Ind. Eng.*, vol. 23, no. 2, Nov. 2011.

[80] “Meeting the Machining Challenges of Additive Manufacturing.” [Online]. Available: https://www.mmsonline.com/articles/meeting-the-machining-challenges-of-additive-manufacturing. [Accessed: 03-Apr-2019].

[81] “Machining of Additively Manufactured Parts: Implications for Surface Integrity | Elsevier Enhanced Reader.” [Online]. Available: https://reader.elsevier.com/reader/sd/pii/S2212827116003486?token=C2D9B4804B5947E5A6AFC7A521ECB9457A675842F25FA61EA1AB2AD0136F91C20A78F71642A82C43988227CE0212EB81. [Accessed: 03-Apr-2019].

[82] “DirectAdditiveSubtractiveHybridManufacturing.pdf.” .

[83] “Predeformation | Amphyon (Additive Works).” [Online]. Available: http://www.amphyon.ru/article/predeformation. [Accessed: 12-Feb-2019].

[84] C. Li, C. H. Fu, Y. B. Guo, and F. Z. Fang, “A multiscale modeling approach for fast prediction of part distortion in selective laser melting,” *J. Mater. Process. Technol.*, vol. 229, pp. 703–712, Mar. 2016.

[85] N. Keller and V. Ploshikhin, “NEW METHOD FOR FAST PREDICTIONS OF RESIDUAL STRESS AND DISTORTION OF AM PARTS,” p. 9.

[86] C. Li, C. H. Fu, Y. B. Guo, and F. Z. Fang, “Fast Prediction and Validation of Part Distortion in Selective Laser Melting,” *Procedia Manuf.*, vol. 1, pp. 355–365, 2015.

[87] P. Alvarez, J. Ecenarro, I. Setien, M. S. Sebastian, A. Echeverria, and L. Eciolaza, “Computationally efficient distortion prediction in Powder Bed Fusion Additive Manufacturing,” *Int. J. Eng. Res.*, vol. 2, no. 10, p. 8.

[88] P. Prabhakar, W. J. Sames, R. Dehoff, and S. S. Babu, “Computational modeling of residual stress formation during the electron beam melting process for Inconel 718,” *Addit. Manuf.*, vol. 7, pp. 83–91, Jul. 2015.

[89] C. Seidel, M. F. Zaeh, M. Wunderer, J. Weirather, T. A. Krol, and M. Ott, “Simulation of the Laser Beam Melting Process – Approaches for an Efficient Modelling of the Beam-material Interaction,” *Procedia CIRP*, vol. 25, pp. 146–153, 2014.

[90] C. Li, J. F. Liu, and Y. B. Guo, “Efficient Multiscale Prediction of Cantilever Distortion by Selective Laser Melting,” p. 11.

[91] “2013-44-Zeng.pdf.” .

[92] N. Patil *et al.*, “A Generalized Feed Forward Dynamic Adaptive Mesh Refinement and Derefinement Finite Element Framework for Metal Laser Sintering—Part I: Formulation and Algorithm Development,” *J. Manuf. Sci. Eng.*, vol. 137, no. 4, p. 041001, Aug. 2015.

[93] D. Pal *et al.*, “A Generalized Feed-Forward Dynamic Adaptive Mesh Refinement and Derefinement Finite-Element Framework for Metal Laser Sintering—Part II: Nonlinear Thermal Simulations and Validations [2],” *J. Manuf. Sci. Eng.*, vol. 138, no. 6, p. 061003, Jan. 2016.

[94] “Distortion prediction and compensation in selective laser melting.” [Online]. Available: https://reader.elsevier.com/reader/sd/pii/S2214860416303104?token=DFCF4962E85E2E886A6F6C70FABBAD0CB695A7B40831424E61F34DF4FD816DF8783217119011456EB4066C340DD453FC. [Accessed: 12-Feb-2019].

[95] E. Budak, Y. Altintaş, and E. J. A. Armarego, “Prediction of Milling Force Coefficients From Orthogonal Cutting Data,” *J. Manuf. Sci. Eng.*, vol. 118, no. 2, p. 216, 1996.

[96] Y. Altintas, *Manufacturing automation: metal cutting mechanics, machine tool vibrations, and CNC design*, 2nd ed. Cambridge ; New York: Cambridge University Press, 2012.

[97] O. Gonzalo, J. Beristain, H. Jauregi, and C. Sanz, “A method for the identification of the specific force coefficients for mechanistic milling simulation,” *Int. J. Mach. Tools Manuf.*, vol. 50, no. 9, pp. 765–774, Sep. 2010.

[98] “Budak et al. - 1996 - Prediction of Milling Force Coefficients From Orth.pdf.” .

[99] M. A. Rubeo and T. L. Schmitz, “Mechanistic force model coefficients: A comparison of linear regression and nonlinear optimization,” *Precis. Eng.*, vol. 45, pp. 311–321, Jul. 2016.

[100] S. A. Tobias, “Vibration of machine tools,” *Prod. Eng.*, vol. 43, no. 12, pp. 599–608, Dec. 1964.

[101] T. Insperger and G. Stépán, *Semi-Discretization for Time-Delay Systems: Stability and Engineering Applications*. Springer Science & Business Media, 2011.

[102] J. Tlusty, W. Zaton, and F. Ismail, “Stability Lobes in Milling,” *CIRP Ann.*, vol. 32, no. 1, pp. 309–313, 1983.

[103] E. Budak and Y. Altintaş, “Analytical Prediction of Chatter Stability in Milling—Part I: General Formulation,” *J. Dyn. Syst. Meas. Control*, vol. 120, no. 1, p. 22, 1998.

[104] D. G. Ford, “Finite element analysis of the structural dynamics of a vertical milling machine,” vol. 44, p. 10, 2003.

[105] B. Li, B. Luo, X. Mao, H. Cai, F. Peng, and H. Liu, “A new approach to identifying the dynamic behavior of CNC machine tools with respect to different worktable feed speeds,” *Int. J. Mach. Tools Manuf.*, vol. 72, pp. 73–84, Sep. 2013.

[106] I. Zaghbani and V. Songmene, “Estimation of machine-tool dynamic parameters during machining operation through operational modal analysis,” *Int. J. Mach. Tools Manuf.*, vol. 49, no. 12–13, pp. 947–957, Oct. 2009.

[107] Z. Li, Q. Liu, X. Ming, X. Wang, and Y. Dong, “Cutting force prediction and analytical solution of regenerative chatter stability for helical milling operation,” *Int. J. Adv. Manuf. Technol.*, vol. 73, no. 1–4, pp. 433–442, Jul. 2014.

[108] “ASM Material Data Sheet.” [Online]. Available: http://asm.matweb.com/search/SpecificMaterial.asp?bassnum=mtp641. [Accessed: 20-Mar-2019].

[109] “Prediction of lack-of-fusion porosity for powder bed fusion | Elsevier Enhanced Reader.” [Online]. Available: https://reader.elsevier.com/reader/sd/pii/S2214860416300471?token=E7DE9F748F66630E27C0347557B26C9522DAED9C67AA8B0E8AA49993146FA9539E460A704D50E5787101AE6AAF38D3C5. [Accessed: 15-Apr-2019].

[110] “QuantAM Material Editor.pdf.” .

[111] A. Okyay, K. Erkorkmaz, and M. B. Khamesee, “Modal Analysis, Metrology, and Error Budgeting of a Precision Motion Stage,” *J. Manuf. Mater. Process.*, vol. 2, no. 1, p. 8, Mar. 2018.

[112] “Speed-varying cutting force coefficient identification in milling | Elsevier Enhanced Reader.” [Online]. Available: https://reader.elsevier.com/reader/sd/pii/S0141635915000823?token=87ED43EC9E691E66FE14

B35DE5C5F42F5AEC4E9EB686C94F2F711530243F8C6328416683A86AD4378CE39B3835A26361. [Accessed: 08-May-2019].

[113] A. Kumar and M. Law, “Experimental identification of cutting force coefficients for serrated end mills,” p. 4.

Appendix A

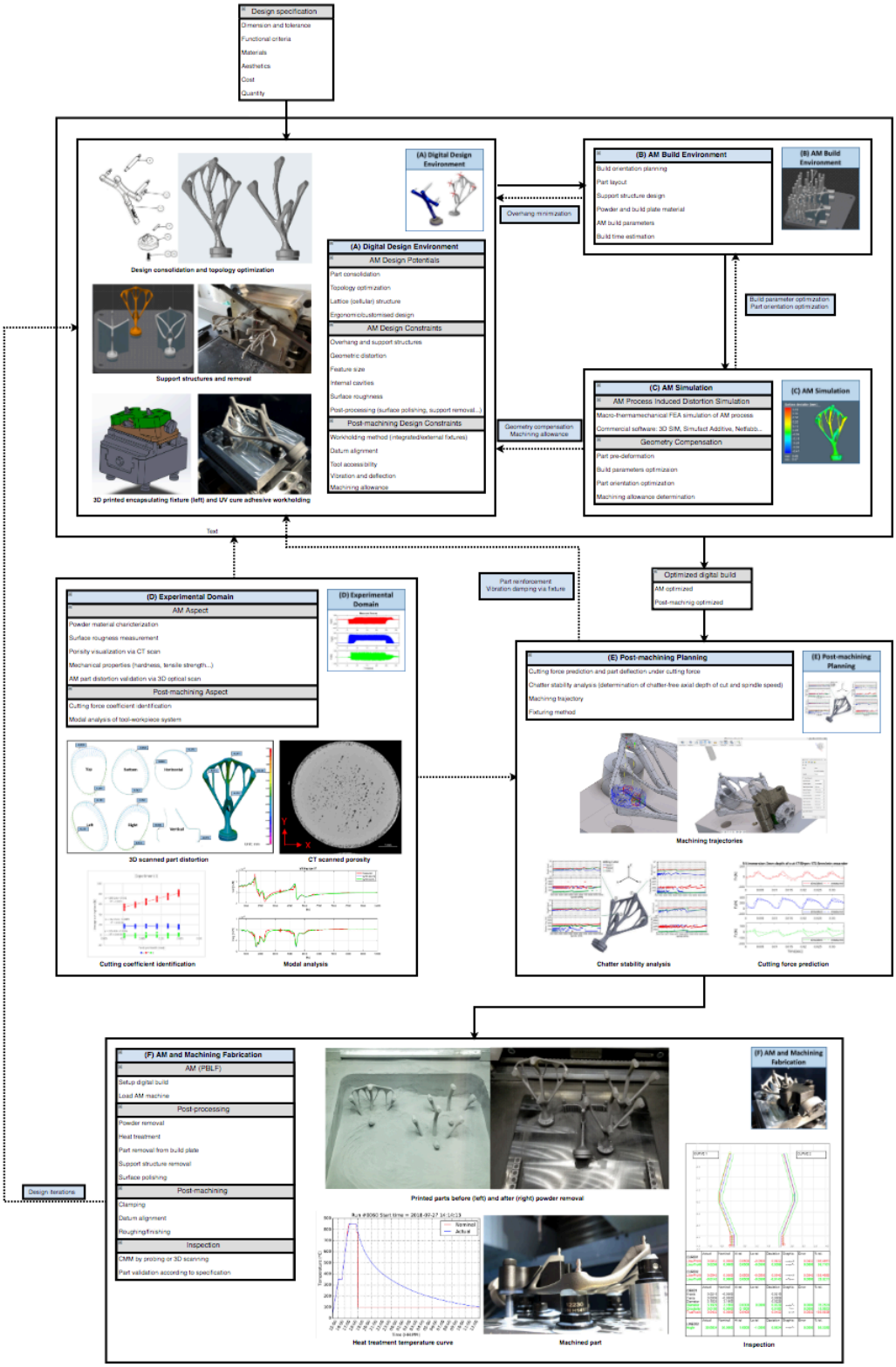
Design specification
Dimension and tolerance
Functional criteria
Materials
Aesthetics
Cost
Quantity
(A) Digital Design Environment
Design consolidation and topology optimization
Support structures and removal
3D printed encapsulating fixture (left) and UV cure adhesive workholding
(A) Digital Design Environment
AM Design Potentials
Part consolidation
Topology optimization
Lattice (cellular) structure
Ergonomic/customised design
AM Design Constraints
Overhang and support structures
Geometric distortion
Feature size
Internal cavities
Surface roughness
Post-processing (surface polishing, support removal...)
Post-machining Design Constraints
Workholding method (integrated/external fixtures)
Datum alignment
Tool accessibility
Vibration and deflection
Machining allowance
Overhang minimization
(B) AM Build Environment
Build orientation planning
Part layout
Support structure design
Powder and build plate material
AM build parameters
Build time estimation
(B) AM Build Environment
Build parameter optimization
Part orientation optimization
Geometry compensation
Machining allowance
(C) AM Simulation
AM Process Induced Distortion Simulation
Macro-thermamechanical FEA simulation of AM process
Commercial software: 3D SIM, Simufact Additive, Netfabb...
Geometry Compensation
Part pre-deformation
Build parameters optimization
Part orientation optimization
Machining allowance determination
(C) AM Simulation
Text
(D) Experimental Domain
AM Aspect
Powder material characterization
Surface roughness measurement
Porsity visualization via CT scan
Mechanical properties (hardness, tensile strength...)
AM part distortion validation via 3D optical scan
Post-machining Aspect
Cutting force coefficient identification
Modal analysis of tool-workpiece system
(D) Experimental Domain
3D scanned part distortion
CT scanned porosity
Cutting coefficient identification
Modal analysis
Part reinforcement
Vibration damping via fixture
Optimized digital build
AM optimized
Post-machining optimized
(E) Post-machining Planning
Cutting force prediction and part deflection under cutting force
Chatter stability analysis (determination of chatter-free axial depth of cut and spindle speed)
Machining trajectory
Fixturing method
(E) Post-machining Planning
Machining trajectories
Chatter stability analysis
Cutting force prediction
(F) AM and Machining Fabrication
AM (PBLF)
Setup digital build
Load AM machine
Post-processing
Powder removal
Heat treatment
Part removal from build plate
Support structure removal
Surface polishing
Post-machining
Clamping
Datum alignment
Roughing/finishing
Inspection
CMM by probing or 3D scanning
Part validation according to specification
Design iterations
Printed parts before (left) and after (right) powder removal
(F) AM and Machining Fabrication
Heat treatment temperature curve
Machined part
Inspection

Appendix B

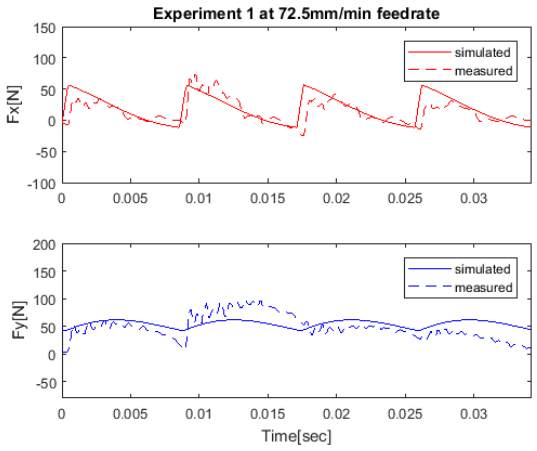
Experiment 1 at 72.5mm/min feedrate
Fx[N]
Fy[N]
simulated
measured
Time[sec]

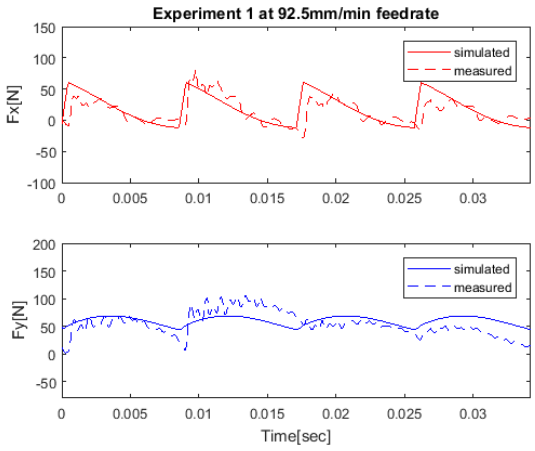
Experiment 1 at 92.5mm/min feedrate
Fx[N]
Fy[N]
simulated
measured
Time[sec]

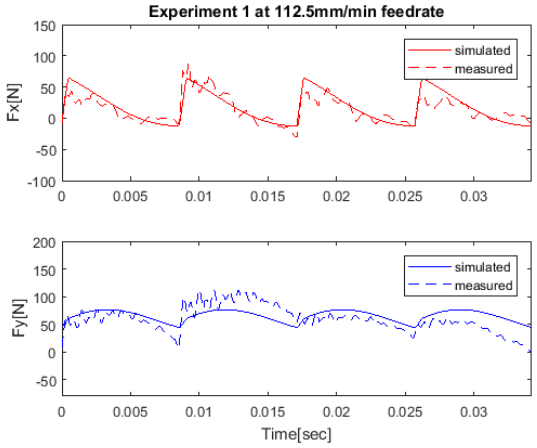
Experiment 1 at 112.5mm/min feedrate
Fx[N]
Fy[N]
simulated
measured
Time[sec]

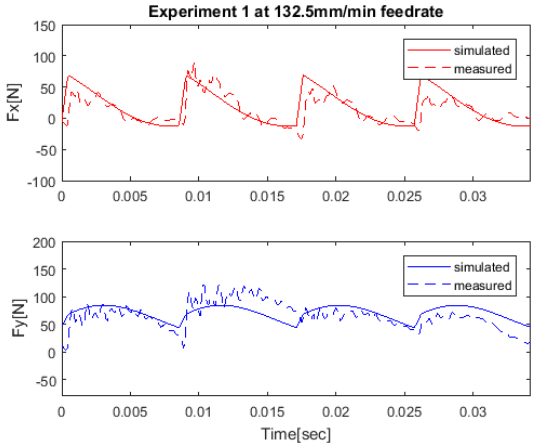
Experiment 1 at 132.5mm/min feedrate
Fx[N]
Fy[N]
simulated
measured
Time[sec]

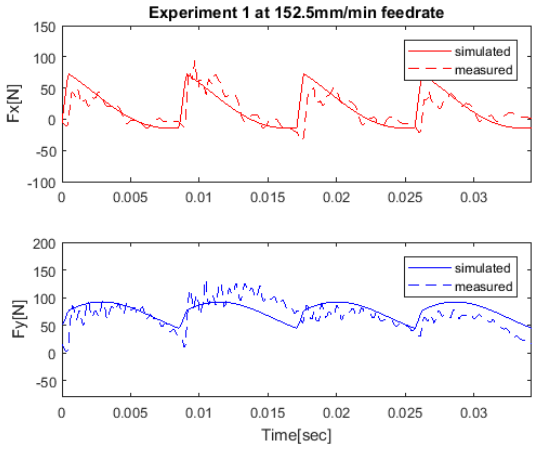
Experiment 1 at 152.5mm/min feedrate
Fx[N]
Fy[N]
simulated
measured
Time[sec]

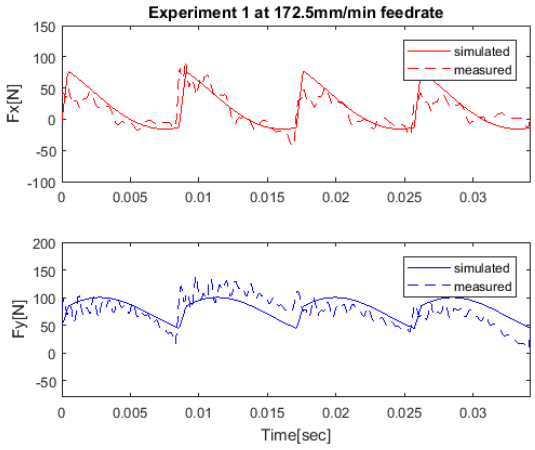
Experiment 1 at 172.5mm/min feedrate
Fx[N]
Fy[N]
simulated
measured
Time[sec]

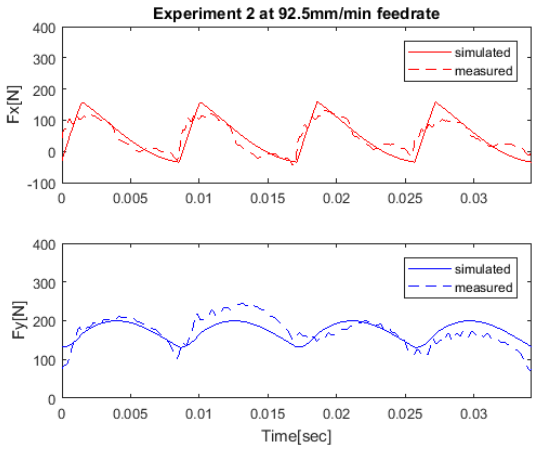
Experiment 2 at 92.5mm/min feedrate
Fx[N]
Fy[N]
simulated
measured
Time[sec]

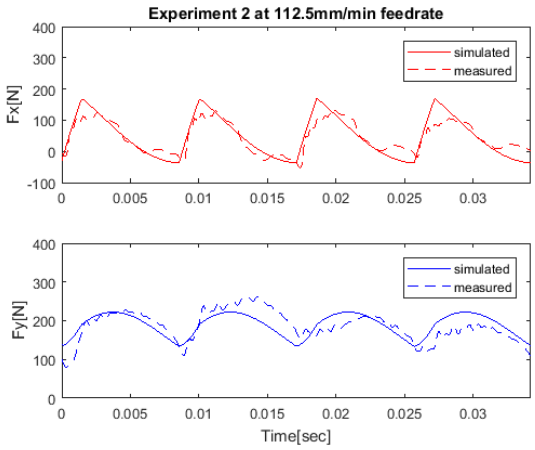
Experiment 2 at 112.5mm/min feedrate
Fx[N]
Fy[N]
simulated
measured
Time[sec]

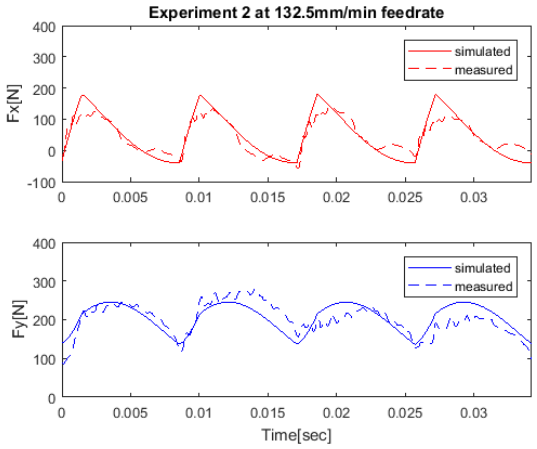
Experiment 2 at 132.5mm/min feedrate
Fx[N]
Fy[N]
simulated
measured
Time[sec]

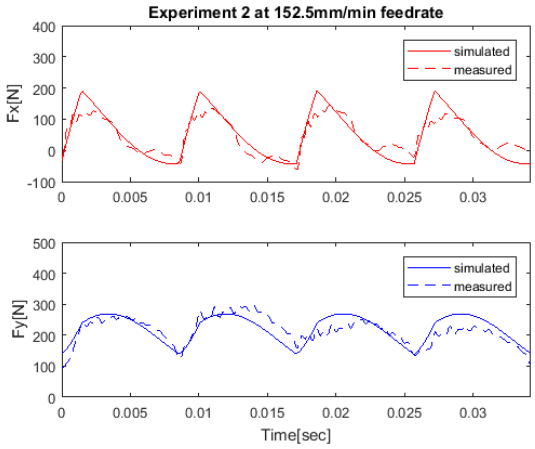
Experiment 2 at 152.5mm/min feedrate
Fx[N]
Fy[N]
simulated
measured
Time[sec]

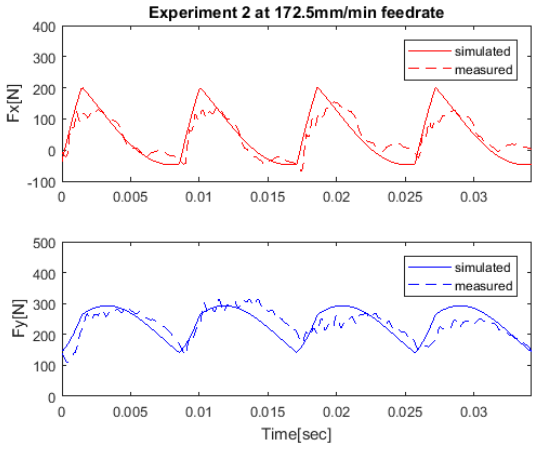
Experiment 2 at 172.5mm/min feedrate
Fx[N]
Fy[N]
simulated
measured
Time[sec]

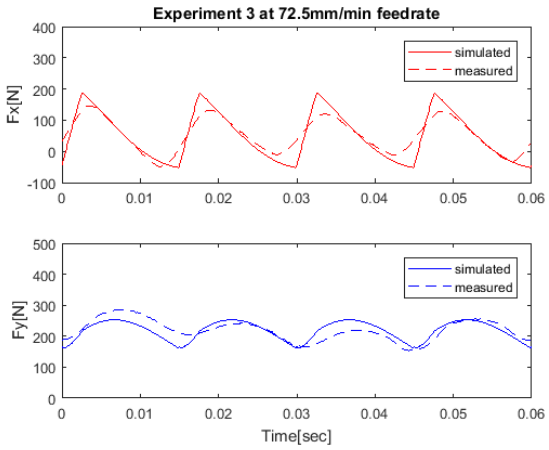
Experiment 3 at 72.5mm/min feedrate
Fx[N]
Fy[N]
simulated
measured
Time[sec]

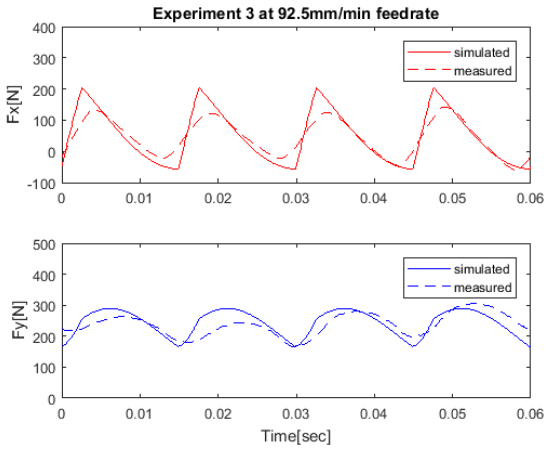
Experiment 3 at 92.5mm/min feedrate
Fx[N]
Fy[N]
simulated
measured
Time[sec]

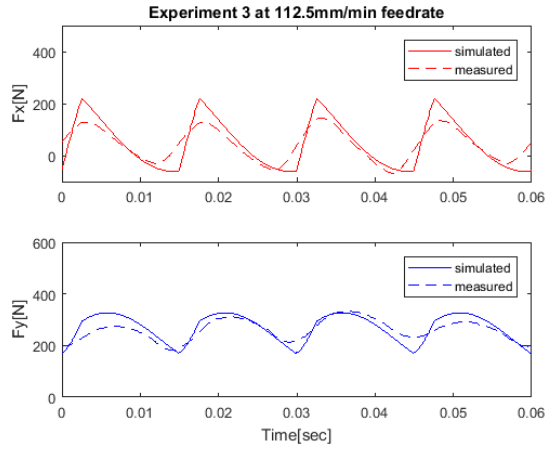
Experiment 3 at 112.5mm/min feedrate
Fx[N]
Fy[N]
simulated
measured
Time[sec]

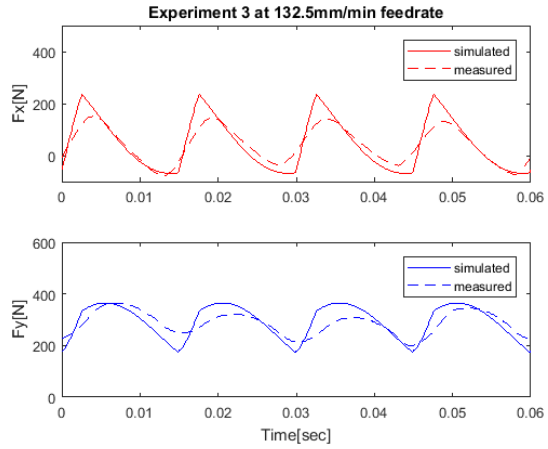
Experiment 3 at 132.5mm/min feedrate
Fx[N]
Fy[N]
simulated
measured
Time[sec]

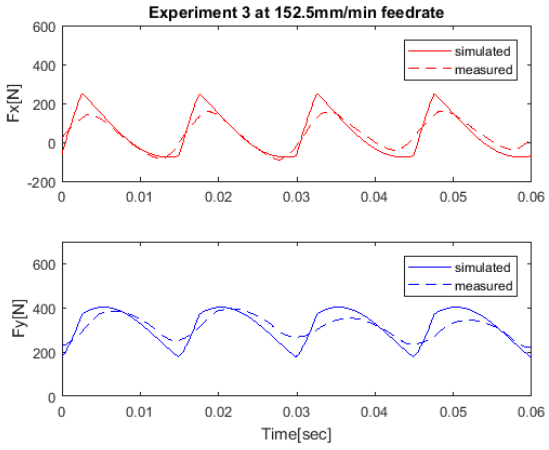
Experiment 3 at 152.5mm/min feedrate
Fx[N]
Fy[N]
simulated
measured
Time[sec]

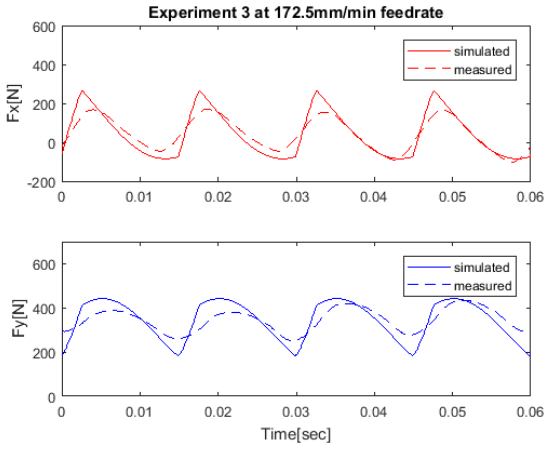
Experiment 3 at 172.5mm/min feedrate
Fx[N]
Fy[N]
simulated
measured
Time[sec]

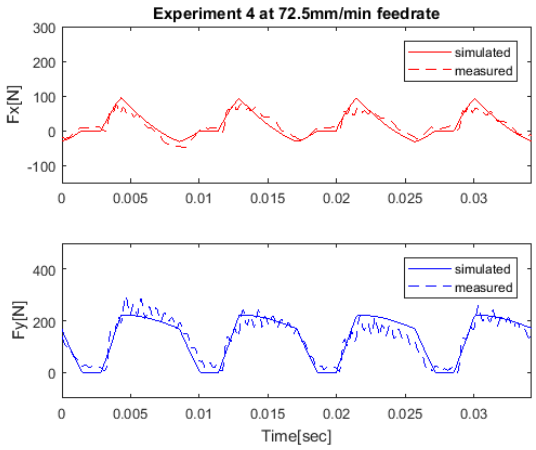
Experiment 4 at 72.5mm/min feedrate
Fx[N]
Fy[N]
simulated
measured
Time[sec]

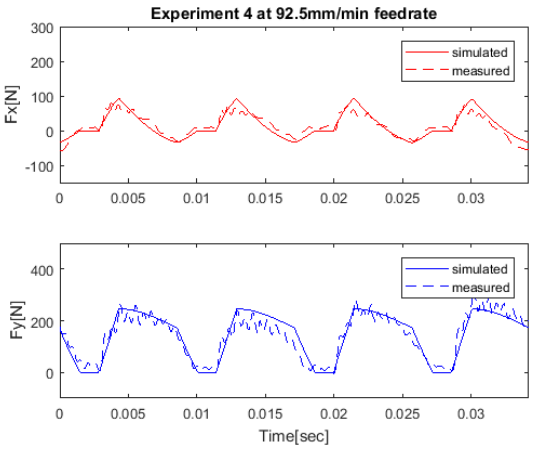
Experiment 4 at 92.5mm/min feedrate
Fx[N]
Fy[N]
simulated
measured
Time[sec]

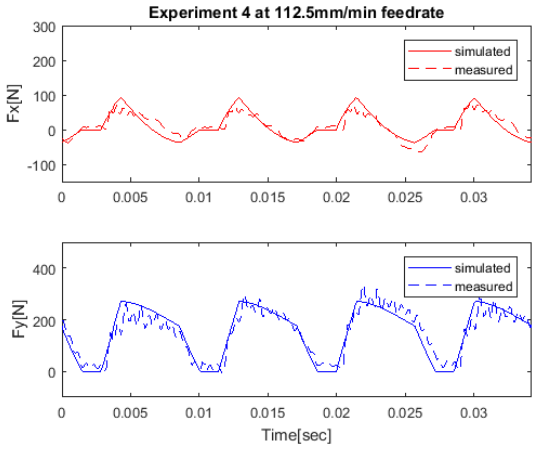
Experiment 4 at 112.5mm/min feedrate
Fx[N]
Fy[N]
simulated
measured
Time[sec]

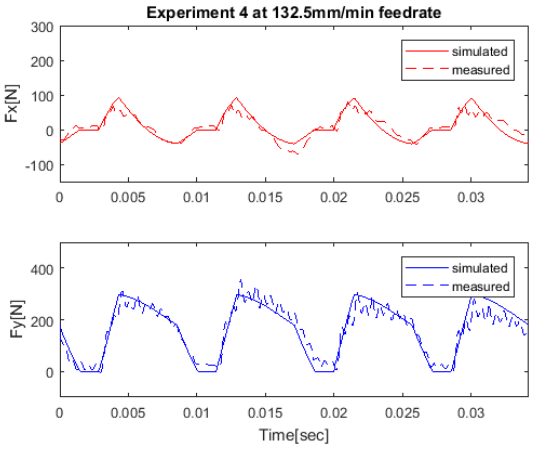
Experiment 4 at 132.5mm/min feedrate
Fx[N]
Fy[N]
simulated
measured
Time[sec]

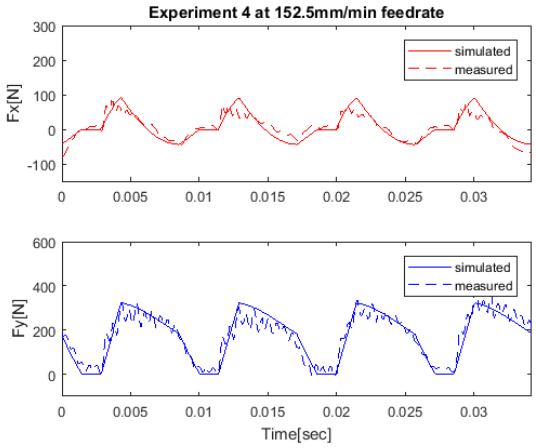
Experiment 4 at 152.5mm/min feedrate
Fx[N]
Fy[N]
simulated
measured
Time[sec]

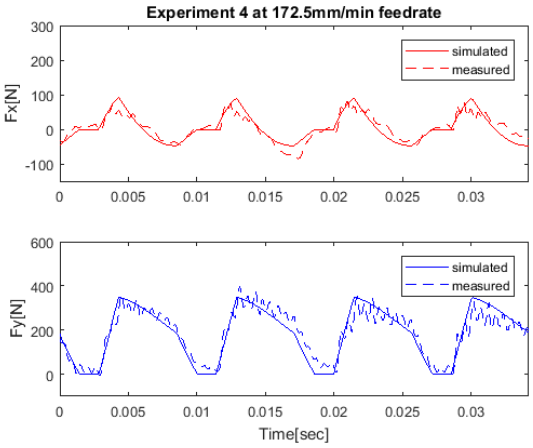
Experiment 4 at 172.5mm/min feedrate
Fx[N]
Fy[N]
simulated
measured
Time[sec]

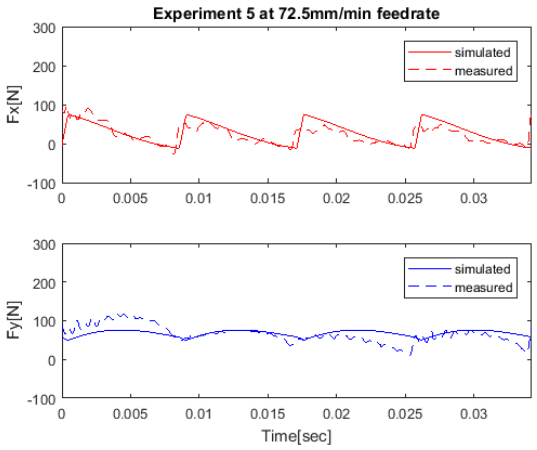
Experiment 5 at 72.5mm/min feedrate
Fx[N]
Fy[N]
simulated
measured
Time[sec]

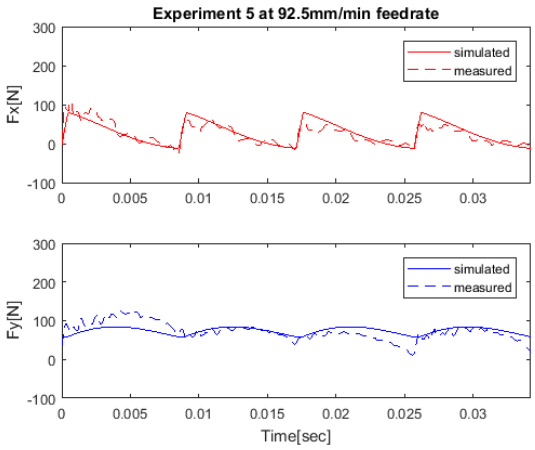
Experiment 5 at 92.5mm/min feedrate
Fx[N]
Fy[N]
simulated
measured
Time[sec]

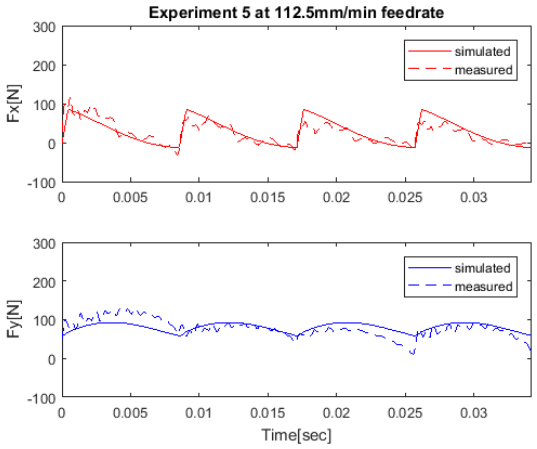
Experiment 5 at 112.5mm/min feedrate
Fx[N]
Fy[N]
simulated
measured
Time[sec]

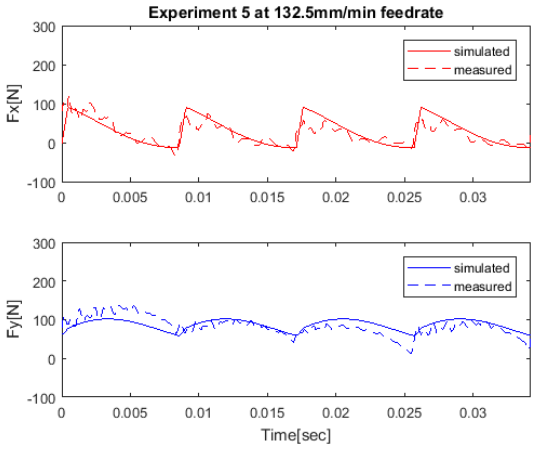
Experiment 5 at 132.5mm/min feedrate
Fx[N]
Fy[N]
simulated
measured
Time[sec]

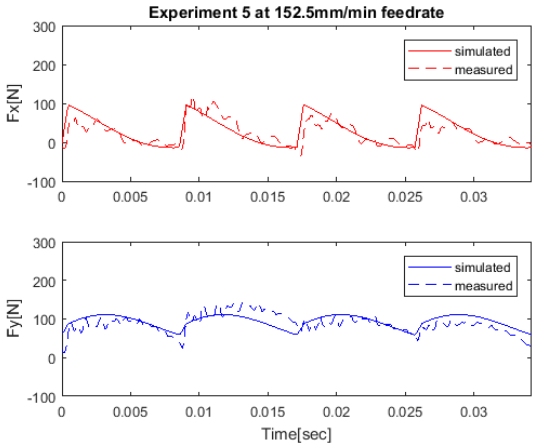
Experiment 5 at 152.5mm/min feedrate
Fx[N]
Fy[N]
simulated
measured
Time[sec]

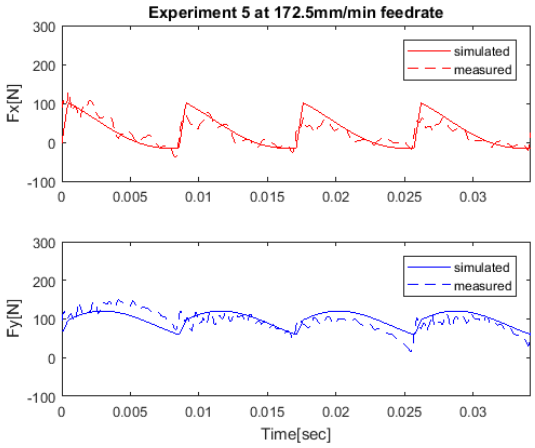
Experiment 5 at 172.5mm/min feedrate
Fx[N]
Fy[N]
simulated
measured
Time[sec]

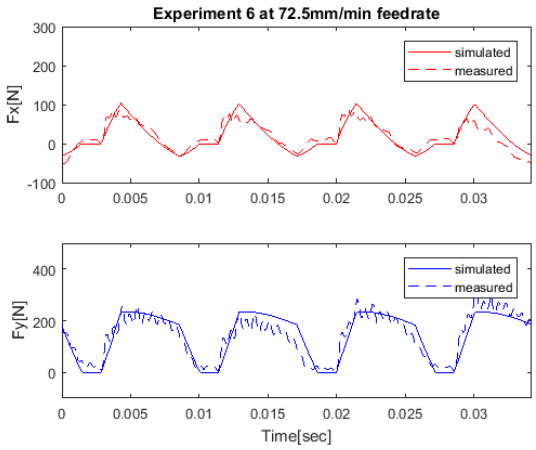
Experiment 6 at 72.5mm/min feedrate
Fx[N]
Fy[N]
simulated
measured
Time[sec]

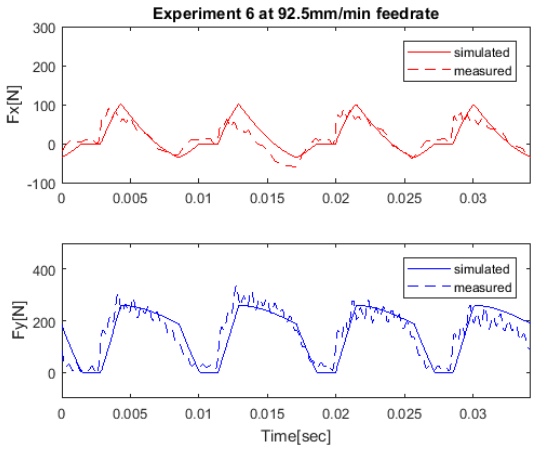
Experiment 6 at 92.5mm/min feedrate
Fx[N]
Fy[N]
simulated
measured
Time[sec]

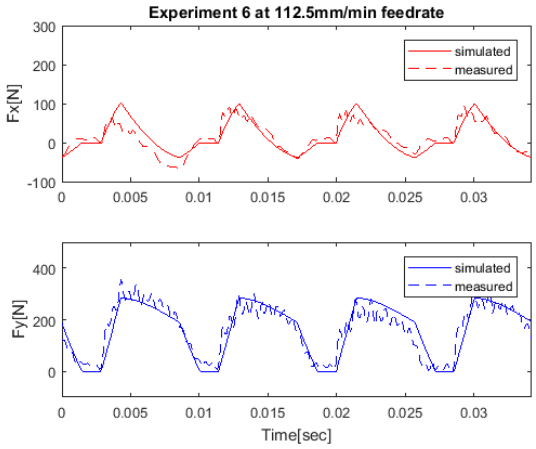
Experiment 6 at 112.5mm/min feedrate
Fx[N]
Fy[N]
simulated
measured
Time[sec]

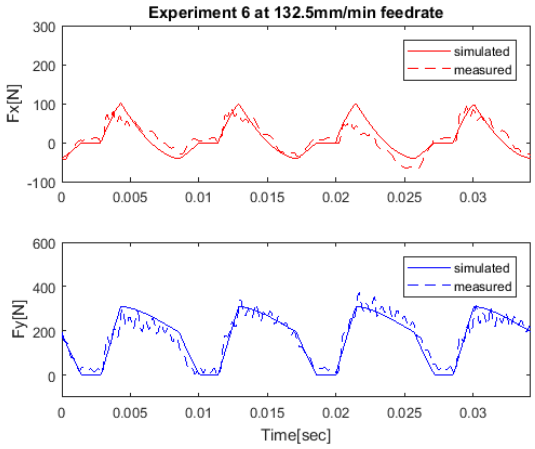
Experiment 6 at 132.5mm/min feedrate
Fx[N]
Fy[N]
simulated
measured
Time[sec]

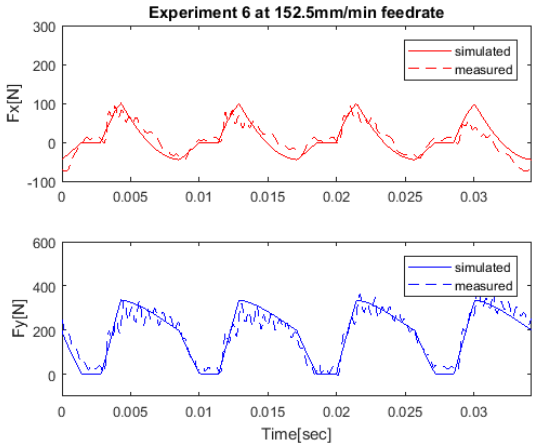
Experiment 6 at 152.5mm/min feedrate
Fx[N]
Fy[N]
simulated
measured
Time[sec]

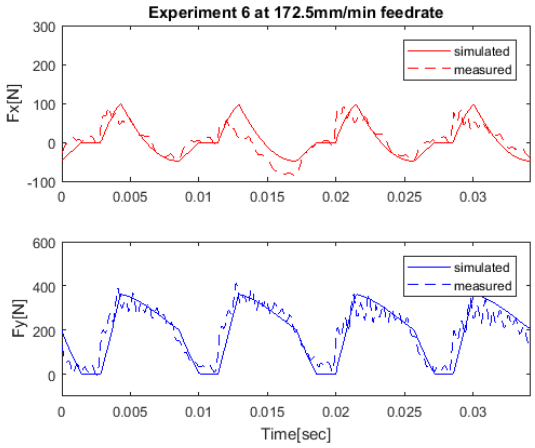
Experiment 6 at 172.5mm/min feedrate
Fx[N]
Fy[N]
simulated
measured
Time[sec]

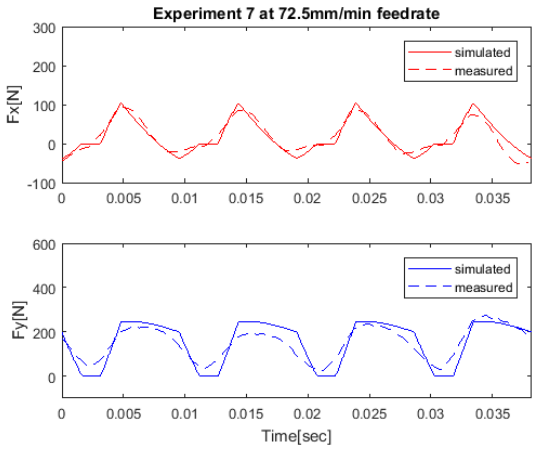
Experiment 7 at 72.5mm/min feedrate
Fx[N]
Fy[N]
simulated
measured
Time[sec]

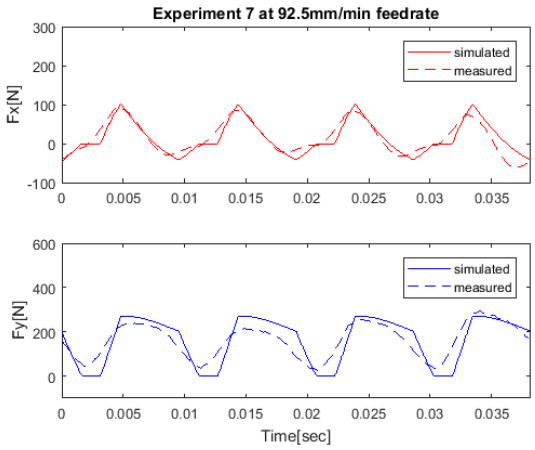
Experiment 7 at 92.5mm/min feedrate
Fx[N]
Fy[N]
simulated
measured
Time[sec]

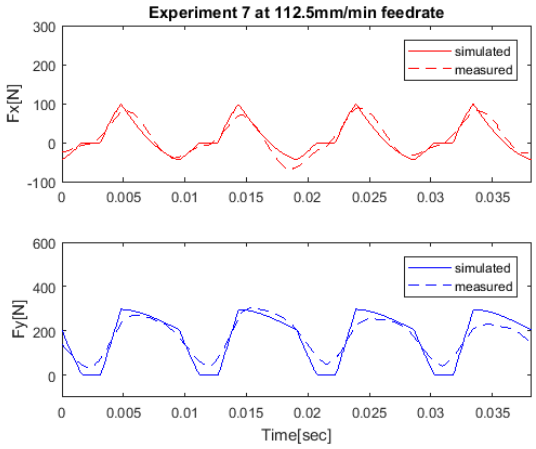
Experiment 7 at 112.5mm/min feedrate
Fx[N]
Fy[N]
simulated
measured
Time[sec]

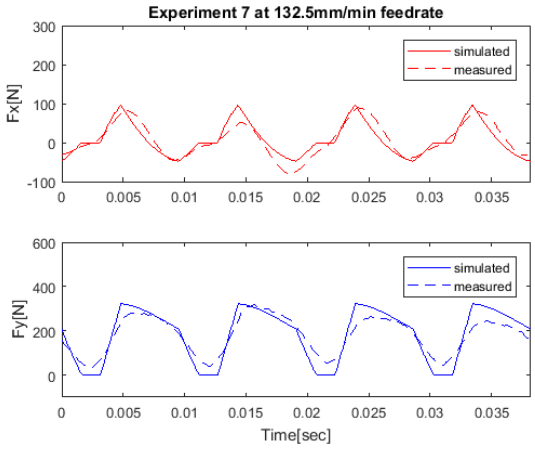
Experiment 7 at 132.5mm/min feedrate
Fx[N]
Fy[N]
simulated
measured
Time[sec]

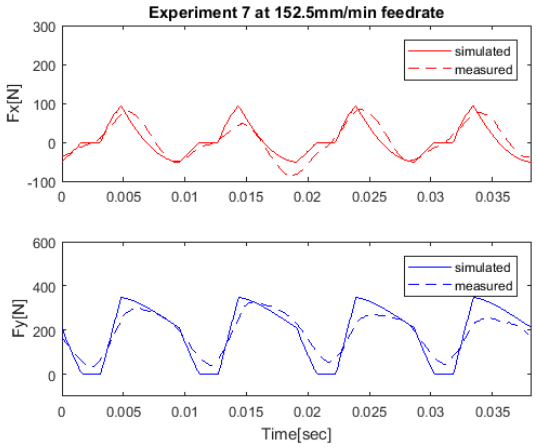
Experiment 7 at 152.5mm/min feedrate
Fx[N]
Fy[N]
simulated
measured
Time[sec]

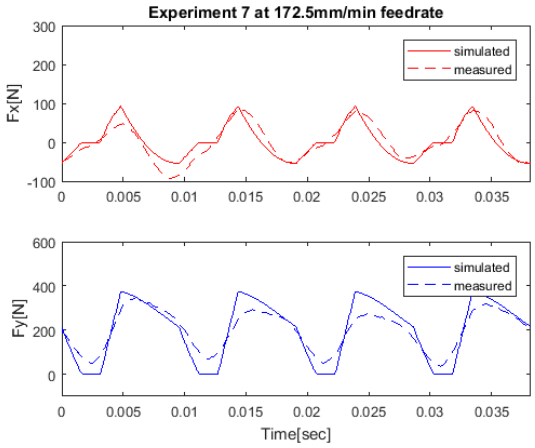
Experiment 7 at 172.5mm/min feedrate
Fx[N]
Fy[N]
simulated
measured
Time[sec]